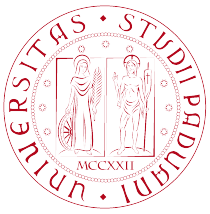

Università
degli Studi
di Padova

Sede Amministrativa: Università degli Studi di Padova
Dipartimento di Ingegneria Industriale

Scuola di Dottorato in: Ingegneria Industriale
Indirizzo: Ingegneria dell'Energia
Ciclo: XXVIII

Aero-Structural Optimization of Vertical Axis Wind Turbines

Direttore della Scuola: Ch.mo Prof. Paolo Colombo
Coordinatore d'indirizzo: Ch.ma Prof.ssa Luisa Rossetto
Supervisore: Ch.mo Prof. Ernesto Benini

Dottorando: Gabriele Bedon

Abstract

This Thesis focuses on the aero-structural simulation and optimization of Darrieus Vertical Axis Wind Turbines.

Aerodynamic simulation tools based on different techniques are developed, improved with respect to state-of-art tools, and validated against experimental data. The main considered approaches are based on the Blade Element Momentum, Vortex, two- and three-dimensional Unsteady Reynolds-Averaged Navier-Stokes (URANS) Computational Fluid Dynamics (CFD) models. The models are developed keeping in mind the final coupling with an optimization algorithm, therefore with particular emphasis on the computational effort and simulation robustness. A structural simulation tool based on the Euler-Bernoulli beam theory is also developed and validated against experimental data to perform an efficient aero-structural simulation.

The validated models are coupled with an optimization algorithm under certain constraints to create an iterative loop able to produce improved designs. Different applications are considered based on the most relevant research topics and real case scenarios. The particular case of a floating Troposkien Vertical Axis Wind Turbine is analysed by improving the baseline aerodynamic design for the 5 MW rotor developed in the FP7 DeepWind project and evaluating the aerodynamic performance under rotor tilted conditions for the 1 kW demonstrator. The airfoil shape for the blade of a 500 kW H-rotor is also subjected to an optimization analysis with the aim to increase the aerodynamic production, obtaining a new geometry different from literature design. Finally, the aerodynamic and structural simulation tools are coupled to perform a complete aero-structural optimization of blade shape and chord distribution for a 500 kW Troposkien rotor. Both aerodynamic production and rotor stress are targeted in the routine and new blade shapes are found and discussed.

The Thesis results, beside the increased performance with respect to the baseline case, prove that iterative loops, obtained by coupling a fast simulation tool and an optimization algorithm, can be adopted in the design and test phase of Darrieus Vertical Axis Wind Turbines, by providing the designer an advanced insight on the aerodynamic and structural phenomena experienced by these complex machines.

Sommario

Questa Tesi ha come oggetto la simulazione e l'ottimizzazione aero-strutturale di Turbine Eoliche ad Asse Verticale Darrieus.

Strumenti per la simulazione aerodinamica basati su differenti tecniche sono sviluppati, migliorati rispetto allo stato dell'arte, e validati rispetto a dati sperimentali. I principali approcci considerati sono basati sui modelli Blade-Element Momentum, Vortex e Unsteady Reynolds-Averaged Navier-Stokes (URANS) Computational Fluid Dynamics (CFD) bi- e tri-dimensionali. I modelli sono sviluppati tenendo a mente l'accoppiamento con un algoritmo di ottimizzazione, quindi con particolare enfasi sullo sforzo computazionale e sulla robustezza della simulazione. Uno strumento di simulazione strutturale basato sulla teoria della trave di Eulero-Bernoulli è, in aggiunta, sviluppato e validato rispetto a dati sperimentali per effettuare una efficiente simulazione aero-strutturale.

I modelli validati sono accoppiati con un algoritmo di ottimizzazione per la creazione di un ciclo per l'ottenimento di configurazioni migliorate. Differenti applicazioni sono considerate, basate sui temi di ricerca più rilevati e scenari reali. Il caso particolare di una Turbina Eolica ad Asse Verticale Troposkiana è stato considerato al fine di migliorare la configurazione aerodinamica di base di un rotore da 5 MW sviluppato nell'ambito del progetto FP7 DeepWind e di valutare le prestazioni aerodinamiche del dimostratore da 1 kW con rotore inclinato. La forma del profilo per la pala di un rotore ad H da 500 kW è oggetto anch'essa di un'attività di ottimizzazione finalizzata all'aumento della produzione aerodinamica, ottenendo una nuova geometria completamente differente da quelle disponibili in letterature. Infine, gli strumenti di simulazione aerodinamica e strutturale sono accoppiati per condurre una completa ottimizzazione aero-strutturale della forma della pala e della distribuzione di corda per un rotore Troposkiano da 500 kW. Sia la produzione aerodinamica che lo stato tensionale sono considerati come obiettivi e nuove forme palari sono individuate e discusse.

I risultati della Tesi, oltre all'incremento di prestazioni rispetto alle geometrie di base, provano che i cicli iterativi, ottenuti tramite l'accoppiamento di un veloce strumento di simulazione e un algoritmo di ottimizzazione, possono essere adottati nella progettazione e test di Turbine Eoliche ad Asse Verticale Darrieus, fornendo al progettista un avanzato strumento di analisi dei fenomeni aerodinamici e strutturali agenti in queste complesse macchine.

Preface

This dissertation is submitted in partial fulfillment of the requirements for the Ph.D. degree in Energy Engineering from the University of Padova. The dissertation includes the research work conducted during the period from January 2013 to December 2015 at the Department of Industrial Engineering and is based on the following scientific papers:

- Gabriele Bedon, Enrico Giuseppe Agostino Antonini, Stefano De Betta, Marco Raciti Castelli, and Ernesto Benini. "Evaluation of the Different Aerodynamic Databases for Vertical Axis Wind Turbine Simulations". *Renewable & Sustainable Energy Reviews* 40 (2014), pp. 386–399. DOI: doi:10.1016/j.rser.2014.07.126.
- Enrico Giuseppe Agostino Antonini, Gabriele Bedon, Stefano De Betta, Luca Michelini, Marco Raciti Castelli, and Ernesto Benini. "Innovative Discrete Vortex Model for Dynamic Stall Simulations". *American Institute of Aeronautics and Astronautics Journal* 53.2 (2014), pp. 479–485. DOI: 10.2514/1.J053430.
- Gabriele Bedon, Stefano De Betta, and Ernesto Benini. "A computational assessment of the aerodynamic performance of a tilted Darrieus wind turbine". *Journal of Wind Engineering and Industrial Aerodynamics* 145 (2015), pp. 263–269. ISSN: 01676105. DOI: 10.1016/j.jweia.2015.07.005.
- Gabriele Bedon, Uwe Schmidt Paulsen, Helge Aagaard Madsen, Federico Belloni, Marco Raciti Castelli, and Ernesto Benini. "Computational Assessment of the DeepWind Aerodynamic Performance with Different Blade and Airfoil Configurations". *accepted on Applied Energy* (2015). DOI: 10.1016/j.apenergy.2015.10.038.
- Gabriele Bedon, Stefano De Betta, and Ernesto Benini. "Performance-Optimized Airfoil for Darrieus Wind Turbines". *second revision submitted to Renewable Energy* (2015).
- Gabriele Bedon and Ernesto Benini. "Aero-structural Design Optimization of Vertical Axis Wind Turbines". *submitted to Wind Energy* (2015).

It is a pleasure to thank my supervisor Prof. Ernesto Benini for his guidance and support during the course of this work. I would also like to thank Stefano De Betta and all my colleagues and friends from the Department of Industrial Engineering for their support and creating a wonderful working atmosphere in which I could develop my research skills.

During my Ph.D. course, I had the opportunity to join the DTU Wind Energy department under the "Test and Measurements" section. I would like to thank Sr. Sc. Uwe Schmidt Paulsen for his guidance on the DeepWind activities and his patience. I would also to thank all my colleagues and friends from DTU to support and help me during this period.

I would also like to express my sincere thanks to my parents Liliana and Roberto for their constant encouragement and support. Finally, I would like to thank Sara for her love, support and understanding which enabled me to fully enjoy this wonderful period.

University of Padova
Padova, January 31st 2016
Gabriele Bedon

Contents

Abstract i

Sommario iii

Preface v

List of Tables x

List of Figures xiv

List of Symbols xv

1 Introduction 1
- 1.1 Offshore Vertical Axis Wind Turbines . . . 2
- 1.2 Aerodynamic Simulation . . . 3
  - 1.2.1 Blade Element Momentum Algorithm . . . 3
  - 1.2.2 Discrete Vortex Model . . . 5
  - 1.2.3 URANS CFD . . . 7
- 1.3 Structural Simulation . . . 8
- 1.4 Experimental Data . . . 9

2 Aerodynamic Simulation 11
- 2.1 Blade Element Momentum Theory . . . 11
  - 2.1.1 Aerodynamic Databases . . . 15
  - 2.1.2 Simulation Results . . . 21
  - 2.1.3 Conclusions . . . 32
- 2.2 Discrete Vortex Model . . . 33
  - 2.2.1 Experimental Data . . . 39
  - 2.2.2 CFD Analysis . . . 39
  - 2.2.3 Simulation Results . . . 42
  - 2.2.4 Conclusions . . . 43
- 2.3 2D URANS CFD . . . 44
  - 2.3.1 Experimental Data . . . 45
  - 2.3.2 Simulation Results . . . 46
  - 2.3.3 Conclusions . . . 48

2.4 3D URANS CFD . . . 48
2.4.1 Experimental Data . . . 50
2.4.2 Simulation Results . . . 52
2.4.3 Conclusions . . . 55

3 Structural Simulation **57**
3.1 Beam Model . . . 57
3.2 Section Properties . . . 61
3.2.1 Moments of Inertia . . . 62
3.2.2 Centroid . . . 62
3.2.3 Shear Center . . . 63
3.2.4 Torsional Constant . . . 65

4 Applications **67**
4.1 DeepWind . . . 67
4.1.1 Baseline Rotor . . . 68
4.1.2 Aerodynamic Optimization . . . 70
4.1.3 Conclusions . . . 79
4.2 Tilted Troposkien . . . 80
4.2.1 Results and Discussion . . . 80
4.2.2 Conclusions . . . 84
4.3 Airfoil Optimization . . . 85
4.3.1 Optimization Rationale . . . 86
4.3.2 Optimization Methodology . . . 87
4.3.3 Results and Discussion . . . 88
4.3.4 Airfoil Aerodynamics . . . 94
4.3.5 Conclusions . . . 99
4.4 Aero-structural Optimization . . . 100
4.4.1 Optimization Algorithm . . . 101
4.4.2 Code Coupling . . . 102
4.4.3 Results and Discussion . . . 103
4.4.4 Aerodynamic Analysis . . . 105
4.4.5 Structural Analysis . . . 107
4.4.6 Conclusions . . . 109

5 Conclusions **111**

Bibliography **113**

List of Tables

2.1 Main geometrical details for Sandia 2-meter rotor [37]. 21
2.2 Main geometrical details for Sandia 5-meter rotor [87]. 23
2.3 Main geometrical details for Sandia 17-meter rotor [88, 89]. 26
2.4 Main geometrical details for Sandia 42-meter rotor [100]. 29
2.5 Main geometrical details for Magdalen Island 37-meter rotor [91]. 31
2.6 Average error in the lift coefficient estimation for different turbulence models, pitching frequency of $k = 0.025$ 41
2.7 Main geometrical features of the baseline rotor configuration. 45
2.8 Geometrical parameters of the simulation mesh. 46
2.9 Percentage power variation with respect to the baseline mesh considering different mesh densities and boundary layers steps. 47
2.10 Number of elements and computational time required on a desktop computer equipped with a quad-core Intel i7-860 processor to converge in a single tip speed ratio for each mesh. 48
2.11 Main geometrical features of the baseline rotor configuration. 51
2.12 Geometrical parameters of the baseline mesh. 52
2.13 Simulation results for $\lambda = 4$ with two number of elements on the profile of the blade airfoil. 55

4.1 Baseline parameters for the DeepWind project rotor. 69
4.2 Thrust and side force mean coefficients, cycle amplitude and percentage variation from the baseline configuration for the different analysed configurations. 79
4.3 Maximum power production, power coefficient and percentage variation from the baseline configuration for the different analysed configurations. 79
4.4 Peak power coefficient values, relative tip speed ratios and variations with respect to the vertical configuration. 81
4.5 Drag coefficients at an angle of attack of 0° for the NACA 0018 and WUP 1615 airfoils. 94
4.6 Minimum drag coefficients and their angles of attack for the NACA 0018 and WUP 1615 airfoils estimated with RFOIL. 94
4.7 Chord lengths and percentage of the rotor height for the five blade segments of the selected individuals. 104

4.8 Peak power coefficient and relative tip speed ratio for the baseline and optimized configurations. 105
4.9 Mean, maximum and minimum stress and cycle amplitude for the baseline and the different optimized configurations operating at the maximum power coefficient conditions. 109

List of Figures

2.1 Different interpolation smoothness with respect to PCHIP and Spline methods [96]. 14
2.2 Aerodynamic lift coefficient for NACA 0012 at low Reynolds numbers, Sheldahl et al. [41]. 15
2.3 Aerodynamic lift coefficient for different NACA symmetric profiles at a Reynolds number of $3.6 \cdot 10^5$, Sheldahl et al. [41]. 16
2.4 Difference in lift coefficients between Paraschivoiu and interpolated Sheldahl database for NACA 0018 and Reynolds number of $1.6 \cdot 10^5$. 17
2.5 Difference in lift coefficients between Lazauskas and interpolated Sheldahl database for NACA 0012 and Reynolds number of $1.6 \cdot 10^5$. 18
2.6 Extended Jacobs database compared against Shedahl for NACA 0012. 19
2.7 Extended Jacobs database compared against Shedahl for NACA 0018. 19
2.8 Extended Bullivant database compared against Shedahl for NACA 0025. . . . 20
2.9 Extended Gregorek database for SNLA 0018-50, average Reynolds number of $1.41 \cdot 10^6$. 20
2.10 Extended Gregorek database for SNLA 0018-50, average Reynolds number of $2.52 \cdot 10^6$. 21
2.11 Reynolds numbers and angles of attack for the equatorial section of Sandia 2-meter rotor with respect to the azimuthal position during a blade revolution for an operative condition of $\lambda = 5$, corresponding to the experimental maximum power coefficient condition. 22
2.12 Power coefficient with respect to the tip speed ratio for the Sandia 2-meter turbine, experimental results compared against simulation results with different aerodynamic databases for two rotational speeds. 22
2.13 Reynolds numbers and angles of attack for the equatorial section of Sandia 5-meter rotor with respect to the azimuthal position during a blade revolution for an operative condition of $\lambda = 5$, corresponding to the experimental maximum power coefficient condition. 24
2.14 Power coefficient with respect to the tip speed ratio for the Sandia 5-meter turbine, experimental results compared against simulation results with different aerodynamic databases for five rotational speeds. 25

2.15 Reynolds numbers and angles of attack for the equatorial section of Sandia 17-meter rotor with respect to the azimuthal position during a blade revolution for an operative condition of $\lambda = 4.5$, corresponding to the experimental maximum power coefficient condition. 26
2.16 Power production with respect to the wind speed for the Sandia 17-meter turbine, experimental results compared against simulation results with different aerodynamic databases for five rotational speeds. 27
2.17 Reynolds number and angles of attack for the equatorial section of Sandia 42-meter rotor with respect to the azimuthal position during a blade revolution for an operative condition of $\lambda = 6.2$, corresponding to the experimental maximum power coefficient condition. 29
2.18 Power coefficient with respect to the tip speed ratio for the Sandia 42-meter turbine, experimental results compared against simulation results with different aerodynamic databases for three rotational speeds. 30
2.19 Reynolds numbers and angles of attack for the equatorial section of Magdalen Islands 37-meter rotor with respect to the azimuthal position during a blade revolution for an operative condition of $\lambda = 6$, corresponding to the experimental maximum power coefficient condition. 31
2.20 Power production with respect to the wind speed for the Magdalen Islands 37-meter turbine, experimental results compared against simulation results with different aerodynamic databases for three rotational speeds. 32
2.21 Schematic description of the adopted model [55]. 34
2.22 Non-oscillating steady state validation of the vortex model, NACA 0012 at $\mathrm{Re} = 1.35 \cdot 10^5$. 36
2.23 Boundary conditions of the computational domain. 40
2.24 Near blade mesh. 40
2.25 URANS validation, NACA 0012 at $\mathrm{Re} = 1.35 \cdot 10^5$, $k = 0.025$. 41
2.26 Comparison between experimental, URANS $k-\omega$ SST and vortex results for different pitching reduced frequencies, NACA 0012 at $\mathrm{Re} = 1.35 \cdot 10^5$. 42
2.27 Scheme of the computational domains with boundary conditions and sizes with respect to the rotor diameter D, not to scale. 44
2.28 500 kW Darrieus wind turbine installation (from: [117]). 45
2.29 Representation of the mesh near the blade walls and for the rotating domain. 46
2.30 Experimental data and simulation results for the 500 kW wind turbine operating at 13.62 rpm. 47
2.31 Scheme of the computational domains with boundary conditions and sizes. . . 50
2.32 Sandia 2-meter Darrieus wind turbine installation (from: [37]). 51
2.33 Original and kinematic viscosity corrected performance of the Sandia 2-meter rotor from the wind tunnel test. 52
2.34 Simulation results with two different configurations for the boundary layer extrusion. 53
2.35 Turbulent viscosity ratio near the airfoil at different azimuthal positions, $\lambda = 4.5$. 54
2.36 Airfoil mesh with 15 step boundary layer extrusion. 55

3.1 Finite element mesh adopted by Sandia to estimate the stress in the 42-meter rotor ([81]). . . . 58
3.2 Comparison between the experimental data, the numerical predictions provided by Sandia and Ansys 14.5 considering the gravitational load and the inertial load for two rotational speeds. . . . 59
3.3 Comparison between the experimental data and the numerical predictions without "mini-struts" provided by Ansys 14.5 and the Structural Model considering the gravitational load and the inertial load for two rotational speeds. 60
3.4 Example geometry for the estimation of section properties: NACA 0021 with 11 spars. . . . 62
3.5 Multicellular shell, with reference to geometrical details. . . . 63
3.6 Internal and external forces introduced in order to find the shear center. . . . 64

4.1 DeepWind optimized blade rotor shape. . . . 68
4.2 Performance for the DeepWind baseline configuration estimated with BEM algorithm. . . . 69
4.3 Single blade tangential and normal force coefficients computed by BEM algorithm. 71
4.4 Rotor thrust and side force coefficients with respect to the different number of blades. . . . 72
4.5 Single blade and whole rotor power coefficients with respect to the different number of blades. . . . 73
4.6 Power curves for the rotor equipped with different blade airfoils. . . . 74
4.7 Single blade tangential and normal force coefficients for different airfoil configurations. . . . 75
4.8 Rotor thrust force coefficients for different airfoil configurations. . . . 75
4.9 Optimization loop obtained by coupling the simulation and the optimization algorithm, from [31]. . . . 76
4.10 Chord distributions of the baseline, free optimization and the trade-off configurations. . . . 77
4.11 Performance for the baseline and optimized trade-off configurations. . . . 77
4.12 Rotor thrust and side force coefficients for baseline and optimized trade-off configurations. . . . 78
4.13 Scheme of the computational domains for the tilted configuration with boundary conditions and sizes, no to scale. . . . 80
4.14 Aerodynamic performance for the two tilted configurations obtained with the URANS CFD simulations. . . . 81
4.15 Performance of the two tilted configurations, estimated by URANS CFD simulations and interpolation of the curve with a reduced wind speed. . . . 83
4.16 Tangential force coefficient C_t with respect to the angle of attack for two operational Reynolds numbers. . . . 83
4.17 Scheme of the optimization loop showing the main iterative steps. . . . 87
4.18 Profile parametrization for the DU 06-W-200 profile. . . . 89
4.19 Pareto front evolution starting from the initial population, including the baseline rotor airfoil (NACA 0018). . . . 89
4.20 Profile parametrization for the WUP 1615 profile. . . . 90

4.21 Ratio between the numerical power coefficients and the numerical baseline maximum value for different tip speed ratios, rotors equipped with NACA 0018 and WUP 1615. 91
4.22 Torque values [Nm] for the single blade with respect to the azimuthal position [°] for different wind speeds. 92
4.23 Normal force values [N] for the single blade with respect to the azimuthal position [°] for different wind speeds. 93
4.24 Aerodynamic coefficients estimated by URANS $k - \omega$ SST and RFOIL simulations for the NACA 0018 and WUP 1615 airfoils. 95
4.25 Pressure coefficients for the NACA 0018 and WUP 1615 airfoils at different angles of attack, Re $3 \cdot 10^6$. 96
4.26 Pressure coefficients near the trailing edge for the NACA 0018 and WUP 1615 airfoils at different angles of attack, Re $3 \cdot 10^6$. 97
4.27 Static and dynamic lift coefficients, WUP 1615 airfoil at Reynolds number of about $3e6$ and tip speed ratio of $\lambda = 2.5$. 98
4.28 Variation ranges of the blade angle of attack with respect to different rotor operative conditions in terms of tip speed ratio. 99
4.29 Optimization loop. 102
4.30 Pareto front and its magnification near the baseline configuration (red cross) for two fitness values and considering a maximum percentage of 1% for the failed simulated sectors. 103
4.31 A selection of three individuals from the Pareto front which dominate the baseline solution: blade shape, segment position and chord lengths for the individual and baseline solution (dashed line and italic font). 104
4.32 Power coefficient vs. tip speed ratio for the baseline and optimized configurations. 105
4.33 Contour plots of the upwind induction factor for the baseline and optimized configurations operating at the maximum power coefficient conditions. 106
4.34 Contour plots of the flatwise stress along the blade length for the baseline and the different optimized configurations operating at the maximum power coefficient conditions. 108

List of Symbols

a $[-]$	Axial induction factor
$a_{i,j}$ $[1/m]$	Influence coefficient
a_u $[-]$	Upwind axial induction factor
a_1 $[-]$	Squire's parameter
ΔA $[m^2]$	Streamtube cross-sectional area
A $[m^2]$	Rotor swept area
A_C $[m^2]$	Airfoil shell area
c $[m]$	Airfoil chord
c_f $[-]$	Circulation reduction factor
C_D $[-]$	Airfoil drag coefficient
C_L $[-]$	Airfoil lift coefficient
$C_{L,\alpha}$ $[-]$	Linear lift coefficient slope
C_n $[-]$	Blade side force coefficient
C_N $[-]$	Rotor side force coefficients
C_P $[-]$	Rotor power coefficient
C_p $[-]$	Pressure coefficient
C_t $[-]$	Single blade tangential force coefficients
C_T $[-]$	Rotor thrust force coefficients
D $[m]$	Rotor diameter
dl $[m]$	Integration length
$\mathbf{e}$ $[-]$	Unit vector
f $[Hz]$	Pitching frequency
ΔF_n $[N]$	Normal force exerted by the blade element as it passes through the streamtube
ΔF_t $[N]$	Tangential force exerted by the blade element as it passes through the streamtube
ΔF_x $[N]$	Instantaneous streamwise force exerted by the blade element as it passes through the streamtube

$\Delta F_{x,u}$ $[N]$	Instantaneous streamwise force exerted by the blade element as it passes through the upwind streamtube
$\Delta \bar{F}_{x,u}$ $[N]$	Average streamwise force exerted by the blade element as it passes through the upwind streamtube
G $[-]$	Auxiliary function for induction factor iterative algorithm
G_S $[Pa]$	Shear modulus
h $[m]$	Rotor height
h_s $[m]$	Spar height
H $[m]$	Rotor total height
I $[m^4]$	Moment of Inertia
I_S $[m^4]$	Total moment of Inertia
J $[m^4]$	Torsional constant
k $[-]$	Reduced pitching frequency
l $[m]$	Airfoil perimeter between two shears
ΔL $[m]$	Actuator line width
n $[-]$	Integer determining the flow velocity shape
n_{bad} $[-]$	Total number of sectors for which the Aerodynamic Model does not converge
$\mathbf{n_i}$ $[-]$	Panel normal unit vector
n_P $[-]$	Number of points for airfoil discretization
N $[-]$	Number of airfoil panels
N_B $[-]$	Number of blades
N_v $[-]$	Number of vertical mesh subdivisions
N_θ $[-]$	Number of horizontal mesh subdivisions
p_u^+ $[Pa]$	Pressures on the upstream face of the upwind actuator disk
p_u^- $[Pa]$	Pressures on the downstream face of the upwind actuator disk
P $[W]$	Power produced by the turbine
P_u $[N]$	Unitary load
q $[N/m]$	Load generated by the torque on the airfoil walls
r $[m]$	Rotor radius relative to a blade element
r_c $[m]$	Vortex core radius
r_{c_0} $[m]$	Initial vortex core radius
$\mathbf{r_i}, r_i$ $[m]$	Distance from the i^{th} vortex center to the point where the induced velocity is computed
R $[m]$	Wind turbine maximum radius
Re $[-]$	Reynolds number
Re_c $[-]$	Chord Reynolds number
Re_v $[-]$	Vortex Reynolds number
RHS $[m/s]$	Right hand side for the influence velocity equation system
s $[N/m]$	Non-dimensional shear load on the spar

S $[N]$	Shear load
t $[m]$	Airfoil thickness
t_s $[m]$	Spar thickness
t_w $[m]$	Airfoil wall thickness
T $[Nm]$	Rotor torque
T_{tot} $[Nm]$	Rotor total torque
T_u $[Nm]$	Unitary torque
T_{up} $[Nm]$	Rotor upwind torque
$\mathbf{v}$, v $[m/s]$	Reference wind speed vector and norm
$\mathbf{v}\infty$, v_∞ $[m/s]$	Free-stream wind velocity vector and norm
v_e $[m/s]$	Downstream equilibrium wind speed
v_i $[m/s]$	Flow velocity at a blade section, i can be up or down
v_u $[m/s]$	Flow velocity at the upwind blade section
$\mathbf{V}$, V $[m/s]$	Velocity vector and norm
$\mathbf{V_b}$, V_b $[m/s]$	Velocity vector and norm induced by a airfoil lumped vortex
$\mathbf{V_i}$, V_i $[m/s]$	Velocity vector and norm induced by a generic lumped vortex
$\mathbf{V_l}$, V_l $[m/s]$	Downstream velocity vector and norm with respect to the shear layer
$\mathbf{V_r}$, V_r $[m/s]$	Velocity vector and norm due to the motion of the panel
$\mathbf{V_s}$, V_s $[m/s]$	Velocity vector and norm induced by a wake lumped vortex shed from the separation point
$\mathbf{V_{tot,i}}$, $V_{tot,i}$ $[m/s]$	Total velocity vector and norm induced on the i^{th} panel element
$\mathbf{V_{tot,j}}$, $V_{tot,j}$ $[m/s]$	Total velocity vector and norm induced on the j^{th} wake element
$\mathbf{V_u}$, V_u $[m/s]$	Upstream velocity vector and norm with respect to the shear layer
$\mathbf{V_w}$, V_w $[m/s]$	Velocity vector and norm induced by a wake lumped vortex shed from the trailing edge
w_i $[m/s]$	Relative velocity at a blade element cross-sectional plane, i can be up or down
w_u $[m/s]$	Relative velocity at the upwind blade element cross-sectional plane
Δx, Δy $[m]$	Vortex element displacements
x $[m]$	Airfoil abscissa coordinate
x_c $[m]$	Centroid abscissa coordinate
x_{dy} $[-]$	Dynamic separation point
x_s $[m]$	Spar position
x_{sh} $[m]$	Shear center abscissa coordinate
x_{st} $[-]$	Non-oscillating steady state separation point
y $[m]$	Airfoil ordinate coordinate
y_c $[m]$	Centroid ordinate coordinate

y^+ $[-]$	Non-dimensional distance, based on local cell fluid velocity, from the wall to the first mesh node
Δz $[m]$	Streamtube height
α $[rad]$	Airfoil angle of attack
α_L $[-]$	Oseen parameter
β $[^\circ]$	Rotor tilt angle
$\mathbf{\Gamma_b}$, Γ_b $[m^2/s]$	Total airfoil lumped vortex intensity vector and norm
$\mathbf{\Gamma_{b,i}}$, $\Gamma_{b,i}$ $[m^2/s]$	Airfoil panel lumped vortex intensity vector and norm
$\mathbf{\Gamma_i}$, Γ_i $[m^2/s]$	Generic lumped vortex intensity vector and norm
$\mathbf{\Gamma_s}$, Γ_s $[m^2/s]$	Separated wake lumped vortex intensity vector and norm
$\mathbf{\Gamma_w}$, Γ_w $[m^2/s]$	Trailing edge wake lumped vortex intensity vector and norm
δ $[rad]$	Blade element inclination with respect to the vertical plane
λ $[-]$	Tip speed ratio
ζ $[s]$	Time
$\Delta\zeta$ $[s]$	Time step
θ $[rad]$	Blade azimuthal coordinate
θ_i $[rad]$	Airfoil shell rotation angle
θ_S $[rad]$	Total airfoil rotation angle
$\Delta\theta$ $[rad]$	Azimuthal mesh size
μ $[kg\ m/s]$	Dynamic viscosity
ν $[m^2/s]$	Kinematic viscosity
ρ $[kg/m^3]$	Air density
σ $[-]$	Rotor solidity
σ_z $[MPa]$	Flatwise stress
τ $[s]$	Time constant
ω $[rad/s]$	Rotor angular velocity

Chapter 1

Introduction

During the last decade, wind energy has experienced a cubic growth [1] due to the increasing awareness for the need of a renewable energy source that could provide humanity with a solution to overcome the actual fossil fuel dependency. In this regard, the ongoing research on wind turbine technology development has resulted in new concepts that improve the production and reduce the cost of energy.

Vertical Axis Wind Turbines (VAWTs) are recently gaining a considerable interest [2–4] due to their inherent qualities that make their use in favour with respect to the horizontal axis systems [5, 6]. The design simplicity linked to the bottom position of the generator and combined with the easiest control policy, which does not require any pitch or yaw mechanism, allows their use both in urban and extremely isolated areas, where the maintenance work needs to be minimized. Among the different VAWTs types, Darrieus wind turbines are the most interesting due to the higher efficiency and reduced loads compared to other configurations [7]. On the other hand, these machines are characterized by complex aerodynamics due to the unsteady working conditions.

The aim of this Thesis is to develop, validate and test aerodynamic and structural simulation models coupled with an optimization algorithm to provide efficient design and verification tools. The models are developed with particular emphasis on the computational effort and simulation robustness. The design tools are afterwards applied to different applications based on the most relevant research topics and real case scenarios.

1.1 Offshore Vertical Axis Wind Turbines

Similar to horizontal axis wind turbines, which are now being constructed in offshore locations in order to exploit the observed higher power density [8, 9] and increase its size without incurring Not In My Back Yard (NIMBY) issues [10], VAWTs are also recently object of research activities in order to prove the feasibility of offshore configurations with sensibly increased size.

Based on the experience from onshore installations, a variety of research projects aim to deploy Darrieus wind turbines in offshore environments. Different from horizontal axis wind turbines, whose installations generally include foundation technologies that constraint the turbine movement (e.g., monopile, gravity base, tripod base, and jacket structures) [11–13], a floating concept is being analysed for VAWTs, which would allow its installation in deeper waters [14].

Nowadays two main projects are being conducted by the main institutions of the offshore VAWT research. The *Inflow* project [15] aims at demonstrating the cost competitiveness and provide an industrial prototype of a helical Darrieus turbine that might be installed on a semi-submersible floater support structure. A 26 MW wind farm is designed as target to complete the first phase of its industrialization process, with 13 turbines to be built and installed, based on the background experience developed during onshore and offshore tests. The *DeepWind* project [16–18] proposed an equivalent floating offshore wind turbine concept, which consists of a long axis that rotates in the water, with a vertical axis Troposkien rotor placed on the top, a generator located at the bottom of the rotor and a sea-bed support structure system [19]. In this system, the vertical axis rotor is targeted to reach a power production of 5 MW. The rotor swept area needed to obtain such power production leads the project researchers to adopt a modified Troposkien shape rotor [20] with a height of about 130 m.

The aerodynamic performance for this type of rotors was estimated by considering the wind turbine as perfectly vertical (i.e., orthogonal) to the free-stream wind speed, despite the rotor, due to the floating support structure, will mostly operate in a tilted configuration. This approximation is usually made in most conventional semi-empirical models used to simulate the aerodynamic performance of VAWTs e.g., the Blade Element Momentum theory [21–23] or Vortex models [24]. Tilted conditions are generally treated by reducing the performance of a tilted rotor by considering only the projection of the free-stream wind speed on the rotor plane [25, 26].

1.2 Aerodynamic Simulation

Different numerical models for the simulation of the complex aerodynamics of these machines have been developed. Three main approaches have been followed, subsequentially developed with the advent of more powerful computational resources. The first model is the Blade Element Momentum (BEM) Multiple Streamtube developed by Strickland [21], successively improved by Paraschivoiu [22, 23] considering the Double Disk approach. This model has the advantage of being extremely simple and fast to provide an estimation of the whole power curve and off-design production, but on the other hand the result reliability is strongly dependent on the quality and the extension of the aerodynamic database adopted [27]. An improved description for the Darrieus wake was possible by the Vortex Wake model developed by Strickland [24], which is able to provide an additional insight of the aerodynamic behaviour. On the other hand, the computational time required for the simulation is sensibly increased with respect to the previously mentioned method. Finally, Computational Fluid Dynamics (CFD) codes provide a more accurate description for turbine aerodynamics [28, 29] but, on the other hand, require more computational time, limiting their use for final testing simulations more than design activities.

1.2.1 Blade Element Momentum Algorithm

The BEM algorithm is considered for several applications to be the most suitable code for design purposes. The choice is linked to the simplicity of the algorithm formulation along with the small computational time required. These peculiarities allow its adoption even coupled with optimization algorithms for the automatic design improvement [30–32], which may require a considerable number of rotor performance evaluations. Algorithms based on BEM theory have been developed and adopted by several authors in order to predict the performance of rotor designs [21–23, 33–35].

The rationale behind the basic formulation of the BEM analysis is to consider the rotor as one actuator disk placed inside a streamtube and subjected to forces. These forces are computed as a first approximation considering the air velocity as uniform. The BEM theory imposes to equate the aerodynamic forces on the airfoil blades to the change in fluid momentum: the air speed at the rotor can be therefore calculated from the free-stream wind speed [34]. This model is denoted as "Single Streamtube Model" and provides good estimations for lightly loaded blades [21]. However, it presents reliability limitations due to the uniform velocity assumption.

Strickland [21] improved this method by considering a mesh of the rotor swept area. This model, named "Multiple Streamtube Model", aims to calculate the interference factor due to

the interaction between air and blade in every section of the mesh. From the air deceleration and considering the energy balance, the forces on the blades can be estimated. The interaction is considered symmetric in the upwind and downwind zones,.

Paraschivoiu [22, 23] introduced the "Double Disk" approach. The interaction between air and blade is not symmetric in the upwind and downwind zones: the equilibrium velocity at the rotor middle section estimated from the decelerated velocity in the upwind zone is adopted as input speed in the downwind zone for the calculation of a second interference factor. The so obtained model is named "Double Disk Multiple Streamtube Model" and provides results more reliable than the previous models. Limiting his research to a small Darrieus wind turbine (2-meter height), Paraschivoiu [36] reported the agreement of the Darrieus Turbine program (DART) with both experimental field data and wind tunnel measurements conducted by Sheldahl [37].

The "Double Disk Multiple Streamtube Model" requires geometry and environmental data:

- Environmental and operative conditions: wind speed, rotational speed, wind shear, etc.;
- Rotor geometry: height, radius, chord distribution, etc.;
- Aerodynamic coefficients of the blade airfoils: lift and drag coefficients at different angles of attack and Reynolds numbers.

As stated before, the reliability of this method is strongly dependent on the accuracy of the aerodynamic database adopted. The simulation of vertical axis rotors requires aerodynamic coefficients extended from angles of attack between $-180°$ and $+180°$ covering a large span of Reynolds number. Unfortunately, the literature review provides mainly experimental databases developed for aeronautic applications, which are very limited in angles of attack and Reynolds numbers.

The coefficients reported in the aerodynamic databases available in literature show numerical differences despite the same Reynolds number. The reasons beside these discrepancies are mainly to be linked to methodology differences which can affect the final result. In particular, the effect of turbulence levels [38] and airfoil roughness [39] are often not considered and details are omitted. Moreover, recent studies show an additional three-dimensional complexity linked to the stall of a finite aspect ratio wing. According to Manolesos et al. [40], stall cells develop on the airfoil surface. These are strongly unstable and their presence can affect the force measurement.

Given all the uncertainties afflicting the databases available in literature, a more practical approach is instead preferred in this Thesis. The main databases, obtained from airfoil

measurements in wind tunnels and available in literature, are considered and the results compared, in order to find the most reliable and provide the VAWT researchers with a practical indication on the methodology to apply for their studies. The databases considered are the one from Sheldahl et al. [41] and their derivatives from Paraschivoiu [36] and Lazauskas et al. [42]. In addition to these, databases from Jacobs et al. [43, 44], Bullivant [45] and Gregorek et al. [46], obtained for aeronautic applications, have been extended beyond stall and included in the comparison. A complete description of these databases is reported in the technical report from Bedon et al. [47].

1.2.2 Discrete Vortex Model

The simulation with numerical models of the aerodynamic behavior of an oscillating airfoil, which is typical for VAWTs, is largely debated in the literature. A general analytical theory for the prediction of the dynamic effects of separated flows over airfoils is still not developed [48, 49] and, in order to obtain reliable data, experimental results and Computational Fluid Dynamics (CFD) simulations are still mandatory.

Common approaches for the numerical simulation of two-dimensional airfoil aerodynamics rely on the panel method which, in the basic formulation, provides good estimations limited to attached flow conditions. Alternatively, thin symmetrical profiles can be represented by a number of concentrated vortices placed along a limited straight line, where the no-penetration condition is imposed on discrete points. This method is widely used for airplane wing aerodynamics simulations and an extensive discussion can be found in Katz & Plotkin [50]. The prediction of the post stall behavior is, however, not covered by the basic formulation.

Several attempts have been conducted to extend the previously described methods to a wider range of angles of attack. Jones [51] studied the case of the unsteady separated flow of an inviscid fluid around a moving flat plate with the introduction of a leading edge vortex and developed a fast numerical algorithm to compare his results with experimental data. The work highlighted an increased aerodynamic normal force and torque in the unsteady conditions with respect to the steady case. This model was further extended by other authors [52, 53] who considered different experimental data and different vortex models. A more general approach considers a second separated vortex shed from the airfoil suction side at a determined separation point provided from experimental tests or estimated by means of viscous boundary layer computations. This methodology was implemented in the panel method by Oler et al. [54]. The authors, however, highlighted a computational inaccuracy for the non-oscillating steady state conditions, linked to the incomplete and inaccurate modelling of the viscous/inviscid interactions in the immediate vicinity of the separation point [54]. A good agreement with experimental lift and drag coefficients was obtained by Katz including

an additional separated wake in a non-viscous vortex code [55, 56]: the intensity of the wake vorticity was computed as a result from the resultant flow field velocity and the shedding point was included as an input obtained from experimental tests. Ramesh et al. [57] recently presented a new criterion for intermittent vortex shedding from a rounded leading edge to be adopted in discrete-vortex methods. The use of a single empirical parameter, linked to the maximum allowable leading-edge suction, allowed to determine the onset, growth, and termination of leading edge vortices. Good agreement is found with experimental and numerical results with respect to forces and complex flows.

Stationary and unsteady separations have been also studied considering the Navier-Stokes equations, in particular focusing on the leading edge and on the generated eddy structures due to Rayleigh instabilities. Osswald et al. [58] implemented a fully implicit direct numerical simulation (DNS) methodology for an unsteady analysis considering a velocity-vorticity formulation, to simplify the theoretical and numerical analysis of manoeuvring flight. The rapid pitch-up of a NACA 0015 airfoil is examined at Re = 1000 and Re = 10000, identifying a possible sequence of events depicting the basic mechanism responsible for the evolution and subsequent shedding of the dynamic stall vortex. Bhaskaran and Rothmayer [59] studied the two-dimensional, unsteady, leading-edge flow over stationary, pitching and oscillating airfoils using the Navier-Stokes equations for flow past a parabola. They showed that the eddy creation prior to reversal in the base flow generally agrees with the theory of Rayleigh instabilities, with a wavelength in reasonable agreement with the theoretical value. Morris and Rusak [60] investigated the inception of leading-edge stall on stationary, two-dimensional, smooth, thin airfoils at low to moderately high Reynolds number flow by a reduced-order, multiscale model problem via numerical simulations. The study reveals the fundamental nature of leading-edge stall on a stationary aerofoil. It is found that there exists a limit approximately equal to 300 on the modified Reynolds number. When the value is below this limit, the flow is dominated by the increasing effect of the adverse pressure gradient which eventually overcomes the viscous stresses ability to keep the boundary layer attached to the airofoil. However, when the value increases above the limit value, the unsteady convective structures relax the effect of the adverse pressure gradient on the viscous boundary layer to delay the onset of stall in the mean flow with respect to Marginal Separation Theory (MST) results [61, 62].

In this Thesis, a discrete vortex model including a separated wake is considered and improved with additional numerical models in order to take into account the airfoil dynamic stall behavior. The model is designed to be adopted for the simulation of the blade profile of a Darrieus VAWT and to enable the optimization of its shape. The particular operative conditions are comparable to a pitching airfoil with a specific range of reduced frequencies, for which the validation will be focused. To simulate the airfoil dynamic behavior due to the change in the angle of attack which leads to different aerodynamic loads on the blade, additional models need to be considered. Several vortex models which describe the temporal

development of the vortices have been developed in the past [63]. The model proposed by Vatistas et al. [64] is adopted in the present work, because of its simple formulation and reasonable accuracy when dealing with concentrated vortices. This model allows the introduction of a core radius, whose growth behavior can be expressed as suggested by Bhagwat & Leishman [65]. In addition to the vortex models, the influence of the airfoil dynamic behavior must be considered for the estimation of the separation point. Experimental data of non-oscillating steady state separation points for different Reynolds numbers are not widely available in literature, whereas different methods for their estimation are quite common [66]: most of them refer to iterative procedures. In the present formulation, a simple model based on the lift on a flat plate in a potential Kirchhoff flow, described by Thwaites [67], is considered and the results are corrected to provide a better agreement with the experimental data. In order to account for the delay in the shift of the dynamic separation point, an empirical formulation is adopted, which is inspired by the time-dependent correlations introduced in the Beddoes-Leishmann dynamic stall model for the angle of attack [68].

The proposed vortex model is particularly suitable for moderately thin profiles and, therefore, the NACA 0012 was selected as a case study. The obtained results are compared with both CFD simulations and experimental data. The CFD analyses, based on a validated simulation of a pitching airfoil, were conducted using the commercial software Ansys Fluent 14.5 [69]. Several experimental data are available in literature for the NACA 0012 profile; the first results for dynamic stall were presented by McCroskey et al. [70, 71] and McAlister et al. [72]. However, Gerontakos [73] provided aerodynamic coefficients both for the steady and for the unsteady cases with the same testing conditions, enabling the model validation in both cases.

1.2.3 URANS CFD

The most flexible solution in terms of operative conditions and rotor geometry, which however requires a higher computational effort, involves the analysis of the two- or three-dimensional aerodynamics using Unsteady Reynolds Averaged Navier Stokes (URANS) CFD techniques. A validation on the mesh and solver settings is always required in order to verify the model predictions compared to experimental data.

Two-dimensional URANS CFD simulations were widely used for airfoil optimization and dynamic stall simulations: the most important contributions are here reported.

Bourguet et al. [74] proposed a blade design strategy based on the simultaneous maximization of the nominal power production, widening of the efficiency range and reduction of the blade weight. Symmetric profiles are considered and parameterized by a 7-control-point Bézier curve. The simulation algorithm adopted is a $k-\epsilon$ URANS CFD model using a "C" type mesh grid.

The optimization results provided an airfoil similar to NACA 0025 with an expected increase of 28% in nominal power production and of 46% in the efficiency range.

Ferreira et al. [75] validated a two-dimensional URANS CFD model against Particle Image Velocimetry (PIV) experimental data. Different mesh grid densities and turbulence models are tested and compared, showing a high sensitivity of these parameters to the final reliability of numerical data with respect to the experimental dynamic stall at low tip speed ratios.

Carrigan et al. [76] adopted an evolutionary algorithm, but the simulation process relied on an URANS CFD computation. The airfoil family investigated is the NACA 4-series, with the aim of maximizing the average rotor efficiency. The optimized airfoil is characterized by a sensible increase in thickness (58% with respect to the baseline) and a decrease in rotor solidity (40% with respect to the baseline).

The use of three-dimensional URANS CFD simulations, due to the required computational effort, are instead limited to particular applications where three dimensional effects or asymmetry need to take into consideration.

Raciti Castelli et al. [29] presented a 3D CFD model for the evaluation of the performance of a straight-bladed Darrieus wind turbine. A considerable overestimation in the numerical results is found with respect to wind tunnel experimental data, which is referred to be linked to blockage effects.

Rossetti and Pavesi [77] investigated the self-starting behavior of a Darrieus wind turbine considering both two-dimensional and three-dimensional simulations. The difference among the numerical results shows the importance of three-dimensional effects such as secondary flows and tip effects. These effects have a positive effect on start-up, increasing the torque characteristic for tip speed ratio of 1.

In this Thesis, two- and three-dimensional URANS CFD simulation models are developed and validated against experimental results.

1.3 Structural Simulation

The structural analysis of VAWTs is generally conducted by adopting a Finite Element Analysis (FEA) and provides reliable results, considering both steady and unsteady approaches. This peculiar flexibility is driven by the fact that, differently from the horizontal design [28], in VAWTs centrifugal and gravitational forces are providing the main contributions to the rotor load system [78, 79].

Berg [80] and Ashwill [81] provided the description of the experimental tests conducted on the Sandia 34m Darrieus wind turbine. The obtained experimental results for both gravitational and inertial loads at different rotational speeds were correctly reproduced with a steady beam element analysis. The comparison is conducted with respect to the flatwise stress, natural frequencies and modal shapes.

Larsen and Madsen [82] describe the implementation of the 2D actuator cylinder flow model for Vertical Axis Wind Turbines in the HAWC2 [83] aerolastic code in order to provide a reliable structural dynamics simulations.

Fereidoni at al. [84] coupled a vortex filament based aerodynamic model with a three dimensional model adopting curved beams. The aeroelastic behaviour of the Sandia 17-meter VAWT is studied with a great agreement except in the region where dynamic stall plays a crucial role in predicting the aerodynamic forces.

Finally, Roscher [85] analysed multiple blade cross-section of a 5 MW Troposkein VAWT with respect to their mass to area ratio. A new design is proposed, that is argued to be easily scalable above 10 MW. The response to stress and fatigue analysis is provided, showing the damage evolution in the rotor operative life.

In this Thesis, a steady model based on the Euler-Bernoulli beam theory [86] is created and validated.

1.4 Experimental Data

In the past years, a considerable amount of papers has been developed on experimental activities for Darrieus rotor of different sizes and characteristics. Sandia National Laboratories provided experimental data both from wind tunnel and open field tests for rotors with an height of 2 m [37], 5 m [87] and 17 m [88, 89]. Turbines with even greater size have been tested in open field environment: the most important examples are the 37 m height Darrieus installed on Magdalen Islands [90, 91], for a maximum power production of 230 kW, and the largest Darrieus ever realized, the Éole project with an height of 96 m and a power production of 4 MW [92]. These turbines operate at different Reynolds numbers, due to their different sizes, and are characterized by different solidities and aerodynamic profiles, mainly NACA 0012, NACA 0015 and NACA 0018. All these experimental data provide a good background for the validation of numerical models, which are needed in order to conduct a successful design activity.

Chapter 2

Aerodynamic Simulation

This chapter present the aerodynamic models which are developed and validated in this Thesis. As presented in the Introduction, three main approaches have been followed, respectively based on the Blade Element Momentum theory (Section 2.1), Vortex theory (Section 2.2) and URANS CFD simulations, considering both two-dimensional (Section 2.3) and three-dimensional (Section 2.4) domains.

2.1 Blade Element Momentum Theory

The simulation model hereby adopted is based on the Double Multiple Streamtube approach developed by Strickland [21] and Paraschivoiu [22, 23]. Two actuator disks describe the upwind and downwind rotor sections, where the interference factors are calculated. The interference factor represents the decrease of air velocity from the freestream due to the interaction with the blade and is defined as:

$$a = 1 - \frac{v_i}{v} \tag{2.1}$$

where v_i is the velocity at the blade (upwind or downwind section) and v is the freestream air speed. The interference factor is estimated by equating the streamwise forces on the airfoil blades to the change in fluid momentum. The first forces can be estimated considering that the actuator disk extracts energy from the fluid and therefore generates a pressure jump which,

for the upwind section (indexed with u), can be calculated as:

$$\Delta \bar{F}_{x,u} \;=\; \left(p_u^+ - p_u^-\right) \Delta A \tag{2.2}$$

where p_u^+ and p_u^- are respectively the pressures on the upstream and downstream faces of the upwind actuator disk and ΔA is the streamtube cross-sectional area.

By considering Bernoulli's equation first between the upstream equilibrium station and the actuator disk and between the actuator disk and the downstream equilibrium equation, Equation 2.2 becomes:

$$\Delta \bar{F}_{x,u} \;=\; \frac{1}{2}\rho \left(v^2 - v_e^2\right) \Delta A \tag{2.3}$$

where ρ is the air density and v_e is the downstream equilibrium wind speed.

The streamwise force must be also equal to the change in fluid momentum over the streamtube area, in formula:

$$\Delta \bar{F}_{x,u} \;=\; \left(\rho v_u \Delta A\right) \left(v - v_e\right) \tag{2.4}$$

where v_u is the local wind speed.

By comparing Equations 2.3 and 2.4, the following relation is obtained:

$$v_e \;=\; 2v_u - v \tag{2.5}$$

Considering the streamtube area as:

$$\Delta A \;=\; r \Delta\theta \Delta z \cos\theta \tag{2.6}$$

where r is the blade element radius, $\Delta\theta$ is the azimuthal mesh size, Δz is the height mesh size and θ is the azimuthal position, Equation 2.4 combined with 2.5 becomes:

$$\Delta \bar{F}_{x,u} \;=\; 2\rho r \Delta\theta \Delta z \cos\theta v_u (v - v_u) \tag{2.7}$$

The blade can be also seen as the responsible for the loads. The instantaneous streamwise force on the element can be therefore expressed as:

$$\Delta F_x \;=\; \Delta F_n \cos\delta \cos\theta + \Delta F_t \sin\theta \tag{2.8}$$

where ΔF_n and ΔF_t are respectively the normal and tangential forces and δ is the blade local slope.

By introducing the normal and the tangential force coefficients, C_n and C_t, Equation 2.8 becomes:

$$\Delta F_{x,u} = \frac{1}{2}\rho w_u^2 \left(\frac{c\Delta z}{\cos\delta}\right)[C_n \cos\delta\cos\theta + C_t \sin\theta] \tag{2.9}$$

where w_u is the relative local wind speed at the upwind blade position and c is the blade chord.

The average streamwise force for the upwind section can be found by averaging the consecutive instantaneous force values at the different azimuthal positions and multiplying by the number of blades:

$$\Delta \bar{F}_{x,u} = \rho w_u^2 \left(\frac{N_B \Delta\theta}{4\pi}\right)\left(\frac{c\Delta z}{\cos\delta}\right)[C_n \cos\delta\cos\theta + C_t \sin\theta] \tag{2.10}$$

where N_B is the number of blades. The normal and tangential force coefficients are commonly derived from the airfoil aerodynamic coefficients, in formulas:

$$C_n = C_L \cos\alpha + C_D \sin\alpha \tag{2.11}$$

$$C_t = C_L \sin\alpha - C_D \cos\alpha \tag{2.12}$$

where C_L and C_D are respectively the lift and drag lift coefficients and α is the geometrical angle of attack.

An interference factor is initially assumed and the algorithm is iterated. A convenient formulation in order to obtain a reliable convergence is suggested by Homicz [93], who provides a function to compute the interference factor for the new iteration:

$$a_u = \frac{1}{1 + G_u(a_u)} \tag{2.13}$$

being the function G_u expressed as:

$$G_u(a_u) = \frac{N_B c}{8\pi r \cos\theta}\left[C_n \cos\theta + C_t \frac{\sin\theta}{\cos\delta}\right]\left(\frac{w_u}{v_u}\right)^2 \tag{2.14}$$

A similar formulation can be derived for the downwind section, giving a second interference factor. As can be clearly seen, the aerodynamic coefficients are deeply involved in the iterative solution for the performance estimation and a particular attention should be given to their choice. In particular, the Reynolds number varies during one revolution and for different

operational conditions at different relative wind speeds. In order to obtain the most reliable estimation from the aerodynamic database, an interpolation on the angle of attack and on the selected Reynolds number is adopted. The selected interpolation algorithm is the Piecewise Cubic Hermite Interpolating Polynomial (PCHIP) [94], which allows a smoother interpolation than other interpolation algorithms e.g. spline interpolation, as can be seen in Figure 2.1, and is suggested for these types of applications [95].

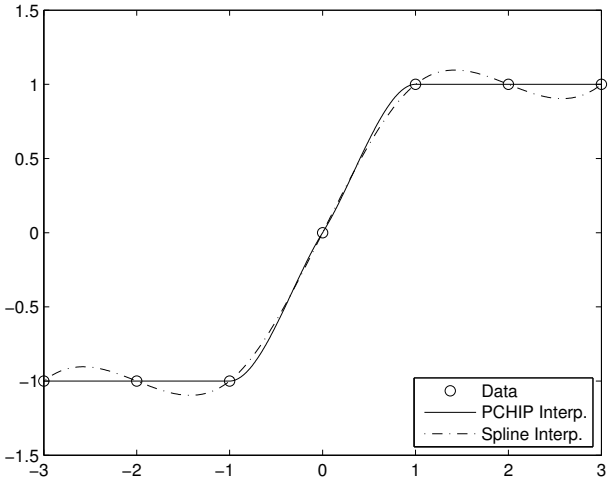

Figure 2.1: Different interpolation smoothness with respect to PCHIP and Spline methods [96].

Different authors provide also models derived from aeronautical use for the dynamic stall evaluation. The blade, experiencing a cyclic change in angle of attack, shows aerodynamic coefficients different from the static values particularly beyond stall [36, 68, 97]. The effect is important for operative conditions characterized by low tip speed ratios but, in this work, in order to obtain the clearest comparison possible, additional models were not included.

From the tangential coefficient C_t the aerodynamic rotor torque can be estimated by means of:

$$T = \frac{N_B}{N_\theta} \sum_{1}^{N_\theta} \sum_{1}^{N_V} \left(0.5 \rho r C_t \frac{c \Delta z}{\cos \delta} \right) w_i^2 \tag{2.15}$$

where N_θ and N_V are respectively the number of azimuthal and vertical mesh elements and w_i is the relative wind speed (upwind or downwind section).

Finally, the power production and the power coefficient are defined as:

$$P = T\omega \tag{2.16}$$

$$C_P = \frac{P}{0.5\rho v^3 A} \tag{2.17}$$

being ω the rotational speed and A the rotor swept area.

2.1.1 Aerodynamic Databases

The aerodynamic databases provided by Sheldahl et al. [41], their derivatives from Paraschivoiu [36] and Lazauskas et al. [42], and the extended databases [47] from Jacobs et al. [43, 44], Bullivant [45] and Gregorek at al. [46] are considered. The databases cover the main rotor configurations whose experimental tests have been published and therefore enable their validation for BEM simulations.

2.1.1.1 Sheldahl

A widely uncritically consulted database for BEM simulations of VAWT is the one provided by Sheldahl et al. [41]. The database is experimentally obtained for three profiles, NACA 0009, 0012 and 0015 at three Reynolds numbers, $3.5 \cdot 10^5$, $5.0 \cdot 10^5$ and $7.0 \cdot 10^5$. The database is successively expanded by means of the computer code PROFILE [98] for NACA 0018, 0021 and 0025 and a wider range of Reynolds numbers. This range includes also very low Reynolds numbers which often characterize the flow in a VAWT. The lift coefficient for NACA 0012 at low Reynolds numbers is represented in Figure 2.2.

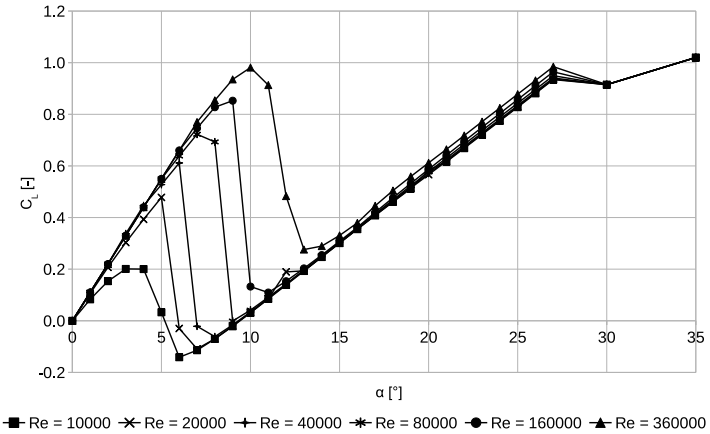

Figure 2.2: Aerodynamic lift coefficient for NACA 0012 at low Reynolds numbers, Sheldahl et al. [41].

The graph highlights peculiarities for this database which must be kept in consideration for the following simulation results. The airfoil at stall conditions presents a very steep decrease

in the lift coefficient, which reaches the lower value by increasing the angle of attack of 1° or 2° from the maximum lift coefficient. This is linked to the nature of the thin airfoil, which results in an abrupt stall, but this extreme predicted behaviour could be also linked to the nature of the numerical algorithm adopted to obtain these coefficients. Moreover the lift coefficient for the Reynolds numbers lower than $1.6 \cdot 10^5$ presents a negative value at certain positive angles of attack, which sounds unphysical considering the similarities with a flat plate. For this reason, in the following computations, only the data for Reynolds number higher than $1.6 \cdot 10^5$ are considered.

Furthermore it is possible to observe that for angle of attack greater than 30° the lift coefficients for all the Reynolds numbers and all the profiles are the same but for the NACA 0012, which however presents only small changes. This is shown in Figure 2.3.

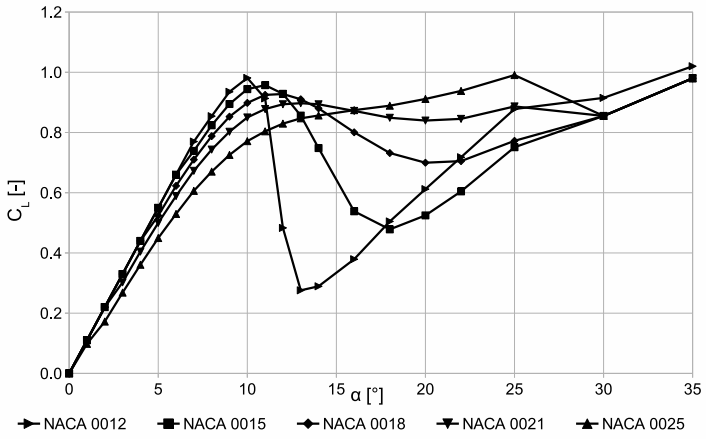

Figure 2.3: Aerodynamic lift coefficient for different NACA symmetric profiles at a Reynolds number of $3.6 \cdot 10^5$, Sheldahl et al. [41].

The decrease in the lift coefficient after the stall is less steep for the thicker profiles and the whole behaviour is smoother. On the other hand, it is possible to observe that after 30° a jump in almost all the lift coefficients is present: the numerical algorithm provided the same values for all the profiles and therefore the switch between the databases is not smooth.

2.1.1.2 Paraschivoiu

The second database considered is the one provided by Paraschivoiu [36]. The database is obtained for NACA 0012, 0015 and 0018 and Reynolds numbers between 10^4 and 10^7. The database is very similar to the previous one but it is provided with aerodynamic coefficients for a larger number of angles of attack, probably obtained through a different interpolation than the one adopted in this work. The difference between the interpolated database from Sheldahl and the one proposed by Paraschivoiu is depicted in Figure 2.4 for the lift coefficient

of NACA 0018 at a Reynolds number of $1.6 \cdot 10^5$.

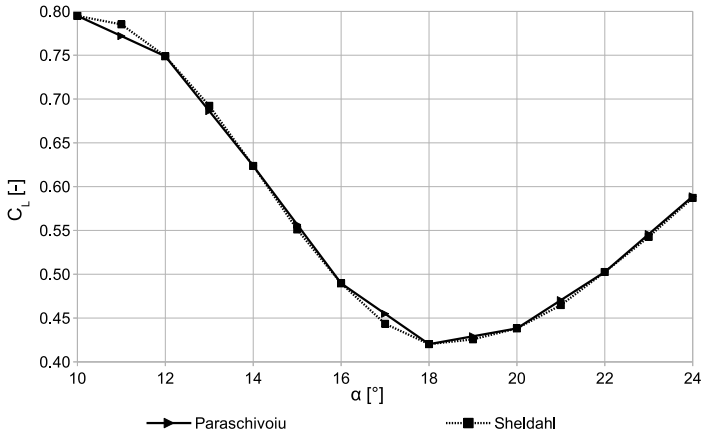

Figure 2.4: Difference in lift coefficients between Paraschivoiu and interpolated Sheldahl database for NACA 0018 and Reynolds number of $1.6 \cdot 10^5$.

The difference in lift coefficient varies considering different airfoil thicknesses: it's lower than 1% for NACA 0012 and NACA 0015 but it reaches values up to 7.9% for NACA 0018 at Reynolds number of $7 \cdot 10^5$. Moreover the maximum differences in drag coefficient for NACA 0015 and NACA 0018 are respectively 1.2% and 2.2% at Reynolds numbers of $1.6 \cdot 10^5$ and $3.6 \cdot 10^5$. This difference could be argued to be limited but, on the other hand, the VAWTs operate in this range of angles of attack and therefore a slight difference could not be preventively omitted. In order to enhance the difference in databases, for this computations all the Reynolds numbers are considered, even those for which a unphysical negative lift coefficient at positive angles of attack is present.

2.1.1.3 Lazauskas

The third considered database is again based on the Sheldahl database but it has been modified by Lazauskas et al. in order to correct the glaring anomalies [42]. As previously observed, indeed, the switch between the experimental data and the numerical prediction in the Sheldahl database created a "jump" in the lift coefficient data. Lazauskas et al. corrected these values in order to provide a smoother trend, as shown in Figure 2.5 for the NACA 0012 profile at a Reynolds number of $1.6 \cdot 10^5$.

Sheldahl, Paraschivoiu and Lazauskas databases represent the most famous database available in the literature whose angles of attack are extended between $-180°$ and $+180°$, allowing their direct use for VAWT applications. However, a few amount of other authors provided the results for airfoil experimental test even at low Reynolds number on the same profiles, but with a limited range of angles of attack. The airfoils in VAWTs operate with angles of attack

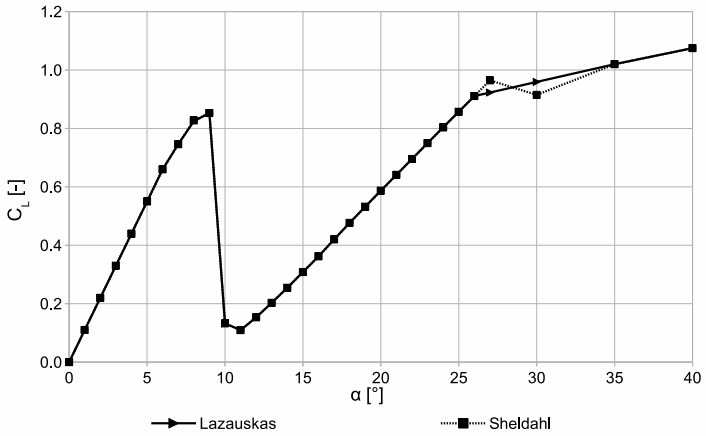

Figure 2.5: Difference in lift coefficients between Lazauskas and interpolated Sheldahl database for NACA 0012 and Reynolds number of $1.6 \cdot 10^5$.

lower than 30° in most of the azimuthal and vertical positions, so it is reasonable to assume that numerically extending the limited databases to higher angles of attack would lead to prediction not largely affected by errors.

2.1.1.4 Jacobs

Jacobs et al. [43, 44] provided experimental databases for NACA 0009, 0012, 0015, 0018 and 0021 and Reynolds numbers ranging between approximately $1.6 \cdot 10^5$ and $3 \cdot 10^6$. The aerodynamic coefficients are provided for a maximum angle of attack of 28°. In order to overcome this limitation, the Sheldahl database is considered: the aerodynamic coefficients for higher angles of attack are included in order to create a complete database. However, in order to provide a smooth transition between the database and the extension, in a region comprised between ±2° from the switch point, the database coefficients are replaced with interpolated values. The extended databases for NACA 0012 and NACA 0018 at Reynolds number around $3.6 \cdot 10^5$ and $1 \cdot 10^6$ are shown in Figures 2.6 and 2.7, compared against the nearest database from Sheldahl.

A considerable difference is highlighted between the lift coefficient trends. The lift coefficient proposed by Jacobs highlights an initial linearity similar to Shedahl's. On the other hand, Sheldahl lift coefficients are characterized by a steeper and earlier stall conditions, where the values are sensibly decreased from the maximum lift. Moreover, Jacobs maximum lift values are higher than Sheldahl's for high Reynolds number and thick profiles. Jacobs drag coefficients are instead generally similar to the Sheldahl values.

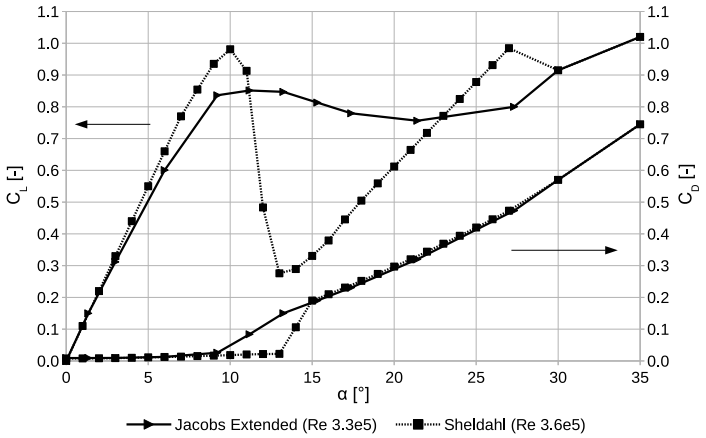

Figure 2.6: Extended Jacobs database compared against Shedahl for NACA 0012.

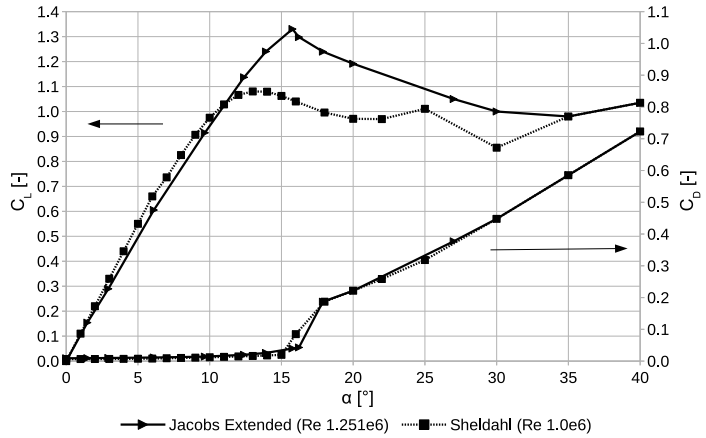

Figure 2.7: Extended Jacobs database compared against Shedahl for NACA 0018.

2.1.1.5 Bullivant

Jacobs et al. [43, 44] do not include any data for NACA 0025 profiles. One of the few database available in literature is provided by Bullivant [45] for the only Reynolds number of $3.2 \cdot 10^6$. Again, the database is provided only for angles of attack lower than 25° and it is therefore extended including the data from Sheldahl database and substituting the coefficients next to the switch point with the interpolated values in order to provide a smooth transition as for the previous database. The comparison between the Bullivant and the Shedahl database is reported in Figure 2.8.

Both the lift and drag coefficients from Bullivant database appear smoother than the Sheldahl values, which present a considerable jump linked to the change in methodology (experimental/numerical). Bullivant maximum lift coefficient is also lower and, consequently, characterized by a higher drag coefficient.

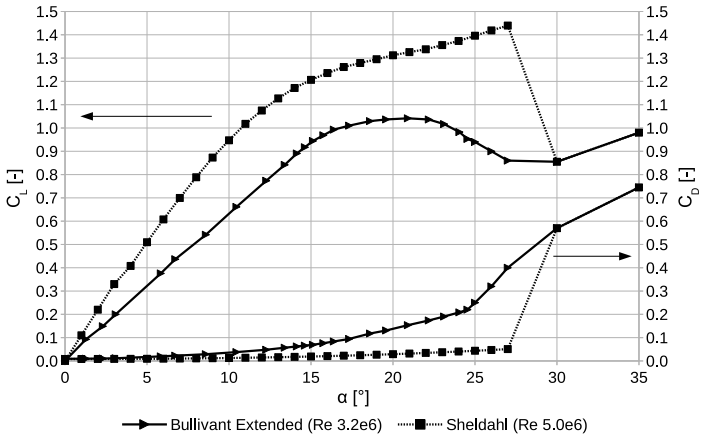

Figure 2.8: Extended Bullivant database compared against Shedahl for NACA 0025.

2.1.1.6 Gregorek

The symmetric profile SNLA 0018/50 is a variation on the traditional NACA 0018 created by Sandia National Laboratories specifically for VAWT applications [99] and was adopted for different rotor configurations. The data considered here are provided by Gregorek et al. [46] and are limited to high Reynolds numbers (above 10^6) and angles of attack lower than 30°. As before, the coefficients from Sheldahl are used to extend the database: in this case, the NACA 0018 coefficients are considered. The aerodynamic coefficients for average Reynolds numbers of $1.41 \cdot 10^6$ and $2.52 \cdot 10^6$ are presented in Figures 2.9 and 2.10.

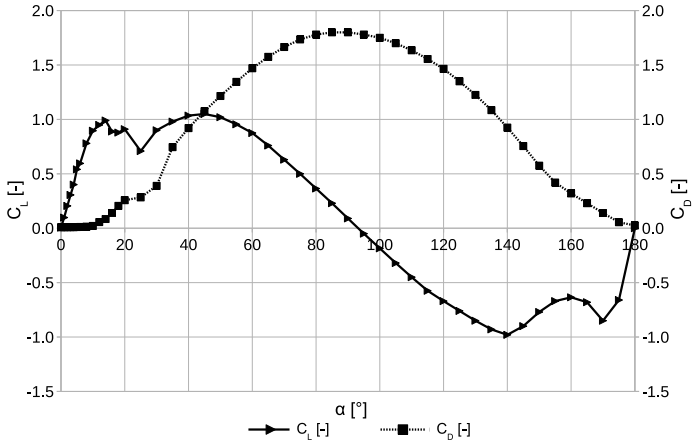

Figure 2.9: Extended Gregorek database for SNLA 0018-50, average Reynolds number of $1.41 \cdot 10^6$.

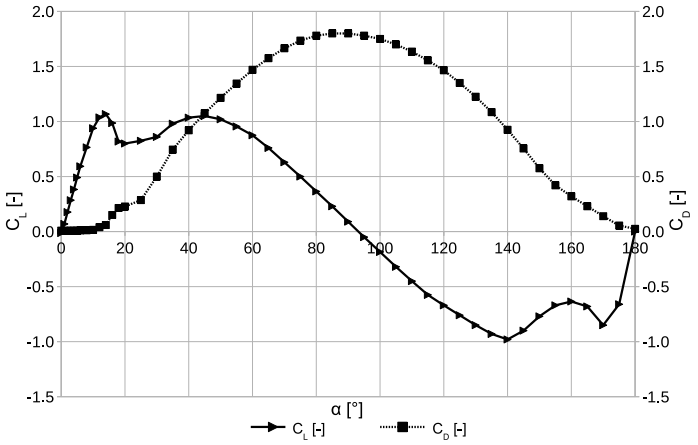

Figure 2.10: Extended Gregorek database for SNLA 0018-50, average Reynolds number of $2.52 \cdot 10^6$.

2.1.2 Simulation Results

The different databases are adopted in the Double Disk Multiple Streamtube Blade Element Momentum model in order to compare the simulation results with experimental data. Different rotor configurations characterized by different sizes, working conditions and aerodynamic profiles are considered, in order to establish the database reliability.

2.1.2.1 Sandia 2-meter

Sandia National Laboratories tested a 2-meter Darrieus VAWT in both wind tunnel and open-field [37]. A good agreement is found between the two experimental results and, in the present work, the open field measurements are considered. The main rotor data are reported in Table 2.1.

H [m]	R [m]	Profile	c [mm]	N_B [-]	σ [-]
2.00	0.98	NACA 0012	58.77	3	0.18

Table 2.1: Main geometrical details for Sandia 2-meter rotor [37].

The turbine is characterized by a NACA 0012 profile and therefore the databases from Sheldahl, Paraschivoiu, Lazauskas and Jacobs are considered. Two fixed rotational speeds are considered in the tests: 400 rpm and 460 rpm. Given the small turbine size, low Reynolds numbers are experienced by the blade during the revolution, as shown in Figure 2.11(a). The blade angles of attack is shown in Figure 2.11(b).

The results for the turbine simulation with the different databases are shown in Figure 2.12.

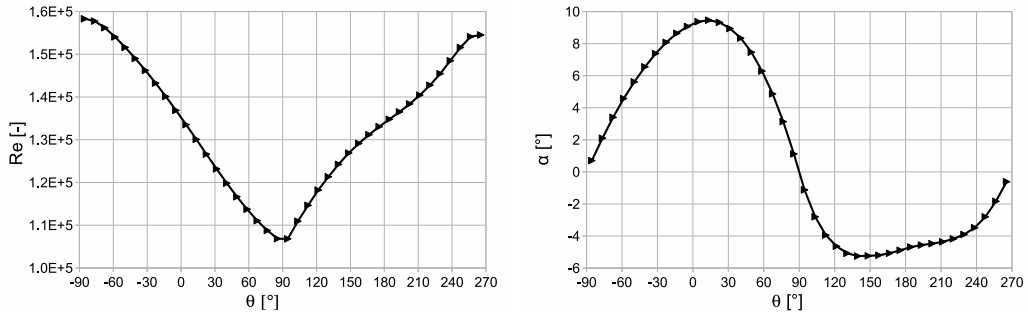

(a) Reynolds numbers (b) Angles of attack

Figure 2.11: Reynolds numbers and angles of attack for the equatorial section of Sandia 2-meter rotor with respect to the azimuthal position during a blade revolution for an operative condition of $\lambda = 5$, corresponding to the experimental maximum power coefficient condition.

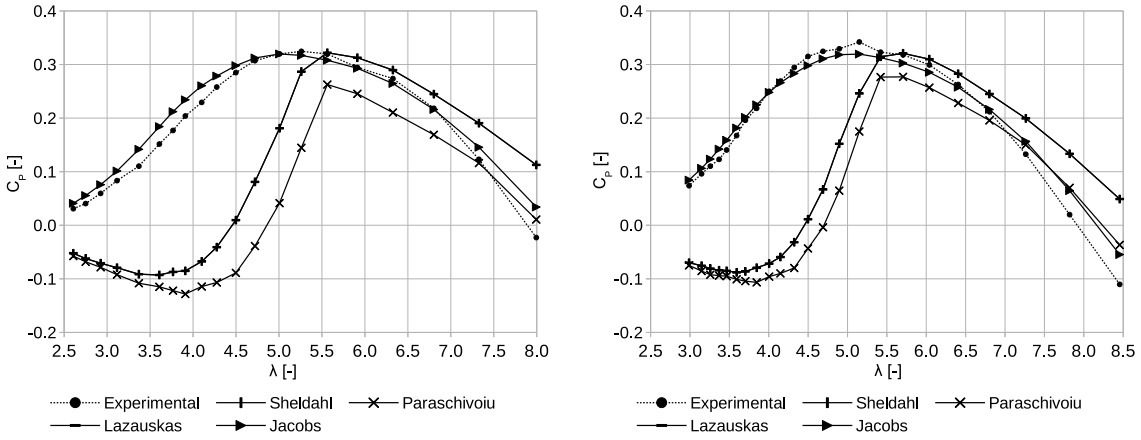

(a) 400 rpm (b) 460 rpm

Figure 2.12: Power coefficient with respect to the tip speed ratio for the Sandia 2-meter turbine, experimental results compared against simulation results with different aerodynamic databases for two rotational speeds.

The database which best reproduces the experimental results is the Jacobs extended database. The experimental curve is indeed reproduced accurately for both pre and post stall operative conditions and both rotational speeds.

Sheldahl and Lazauskas database provide the same results because the differences in coefficients are only related to angles of attack higher than 15° which, in this configurations, are not very relevant. The results are quite accurate for high tip speed ratios, when the angle of attack is limited. For lower tip speed ratios, when the wind speed is increased, the angle of attack is also increased and, as can be seen from Figure 2.11(b), exceeds 10° even in the equatorial plane, the most productive section. The steep decrease of the lift coefficient for

these operative conditions leads to an underprediction with respect to the real blade lift and therefore a penalized estimation in rotor torque.

The database from Paraschivoiu provides the worse estimation. The presence of negative lift coefficients for some angles of attack additionally penalizes the global rotor performances with respect to the Sheldahl simulation, giving an additional shift downwards for the power coefficient curve.

The results highlight that, for small wind turbines experiencing low Reynolds numbers, the Jacobs database should be preferred for BEM simulations.

2.1.2.2 Sandia 5-meter

Another small wind turbine has been tested by Sandia National Laboratories in their test field [87]. The tests were conducted on two prototypes, both with a diameter of 5-meter but equipped with 2 and later 3 blades, all with the same geometry. The main rotor characteristics are reported in Table 2.2.

H [m]	R [m]	Profile	c [mm]	N_B [-]	σ [-]
5.1	2.5	NACA 0015	152.4	2/3	0.12/0.18

Table 2.2: Main geometrical details for Sandia 5-meter rotor [87].

The blade is characterized by a NACA 0015 profiles and therefore the same databases as the case before are adopted: Sheldahl, Paraschivoiu, Lazauskas and Jacobs. Results from five rotational speeds are reported in the paper: from 125 rpm to 175 rpm. The Reynolds numbers are higher than in the previous case but still lower than those commonly considered in aeronautic applications, as shown in Figure 2.13(a). The blade angles of attack is shown in Figure 2.13(b).

The results for the turbine simulation with the different databases are shown in Figure 2.14.

The reliability for the rotor simulations appears to be different with respect to the different rotational speeds.

Considering 125 rpm, it is possible to observe that all the databases over-estimate the turbine production for high tip speed ratios. Increasing the wind speed, the Jacobs database still provides the best result being superimposed to the experimental curve, whereas both Sheldahl, Paraschivoiu and Lazauskas database provide an under-estimate prediction linked to the steep decrease in the lift coefficient after the stall occurs. The three databases show mainly the same results since the Reynolds numbers involved are higher than in the previous case and therefore

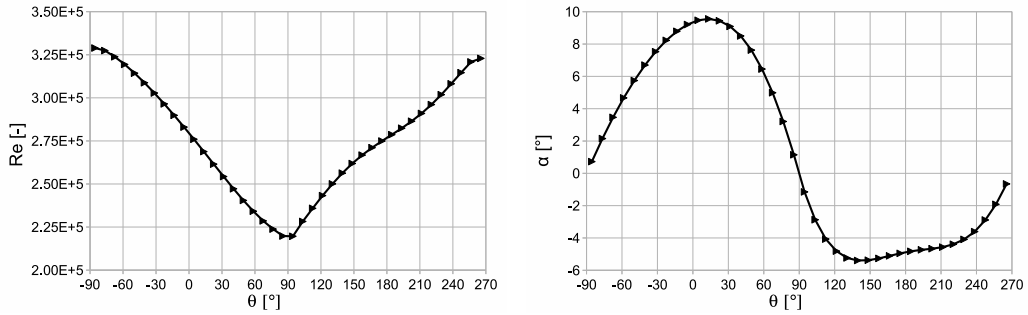

(a) Reynolds numbers

(b) Angles of attack

Figure 2.13: Reynolds numbers and angles of attack for the equatorial section of Sandia 5-meter rotor with respect to the azimuthal position during a blade revolution for an operative condition of $\lambda = 5$, corresponding to the experimental maximum power coefficient condition.

the low Reynolds numbers included in the Paraschivoiu database are not anymore considered.

The experimental data for a rotational speed of 137.5 rpm highlight a strange behaviour for tip speed ratios between 3.0 and 5.5, since the curve experiences a steep change in trend which is not followed by the numerical simulations. All the databases provide reliable results for high tip speed ratios whereas for low tip speed ratio the best results are still achieved with Jacobs database.

Sheldahl, Paraschivoiu and Lazauskas databases show a good approximation for the power coefficient peak for a rotational speed of 150 rpm, whereas Jacobs database provides a slightly underestimated prediction. Again the post stall behaviour is correctly predicted by this last database whereas the first ones under-predict it because of the under-estimation of the lift coefficient.

Finally for the higher rotational speeds and the lower solidity configurations (in this case, only two blades were installed), Jacobs database provides the most reliable result over all the power coefficient curve, exactly predicting both the peak coefficient and the pre- and post-stall behaviour. The same errors for the other databases as in the previous cases are registered.

Concluding, for a rotor configuration characterized by these Reynolds numbers and size, the Jacobs database is suggested to be adopted in order to obtain the most reliable computation.

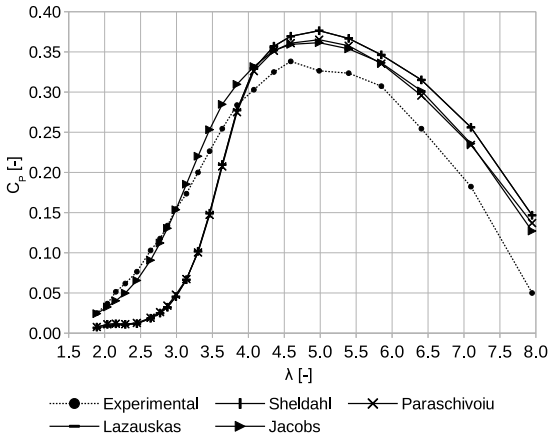

(a) 125 rpm

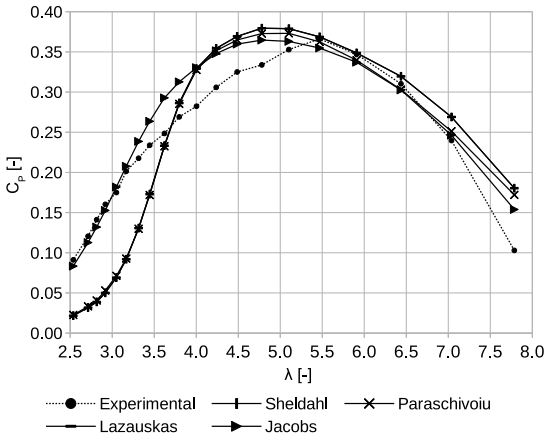

(b) 137.5 rpm

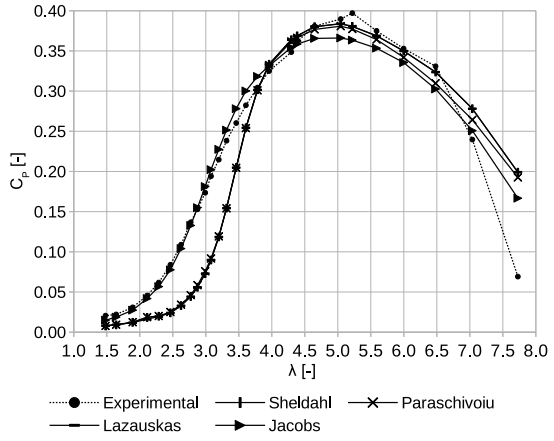

(c) 150 rpm

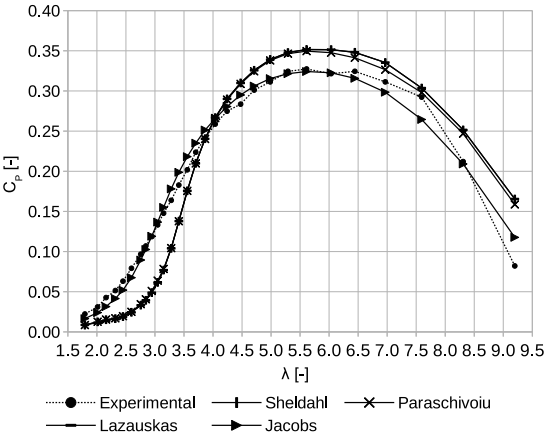

(d) 162.5 rpm

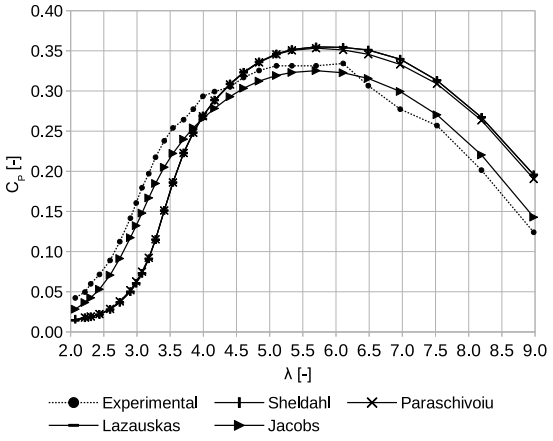

(e) 175 rpm

Figure 2.14: Power coefficient with respect to the tip speed ratio for the Sandia 5-meter turbine, experimental results compared against simulation results with different aerodynamic databases for five rotational speeds.

2.1.2.3 Sandia 17-meter

The 17-meter rotor tested by Sandia National Laboratories is the most documented reference case due to the large availability of measurements for various rotational speeds. The turbine has been tested with both 2-blade and 3-blade configurations [88, 89]. In the present study, the results from the three-blade rotor are considered. The main rotor characteristics are reported in Table 2.3.

H [m]	R [m]	Profile	c [mm]	N_B [-]	σ [-]
17.01	8.36	NACA 0012	533.4	3	0.19

Table 2.3: Main geometrical details for Sandia 17-meter rotor [88, 89].

The rotor is characterized by a NACA 0012 profile as for the 2-meter rotor, and the solidities are almost the same. The same databases as before are therefore adopted: Sheldahl, Paraschivoiu, Lazauskas and Jacobs. On the other hand, the Reynolds numbers are considerably increased, as shown in Figure 2.15(a) and therefore a new comparison is worth. Higher Reynolds number databases are in fact less sensitive to small variations in the Reynolds numbers than lower Reynolds number databases and the experimental tests for their estimation less complex. Moreover, Sandia experimentally tested NACA 0012 profile for higher Reynolds numbers and therefore the aerodynamic coefficients are not only numerically derived as for the lower Reynolds number values. The variation in the angles of attack along the azimuthal position for the rotor equatorial plane is reported in Figure 2.15(b).

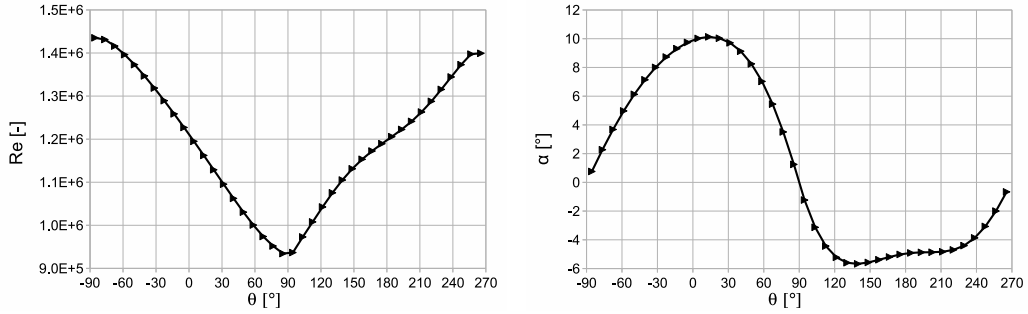

(a) Reynolds numbers

(b) Angles of attack

Figure 2.15: Reynolds numbers and angles of attack for the equatorial section of Sandia 17-meter rotor with respect to the azimuthal position during a blade revolution for an operative condition of $\lambda = 4.5$, corresponding to the experimental maximum power coefficient condition.

The results for the turbine simulation with the different databases are shown in Figure 2.16. The power curves are presented in this case because these are found them more convenient to compare the discrepancies between the simulation results and the experimental data.

The simulation results for this rotor architecture are in general less accurate than for the

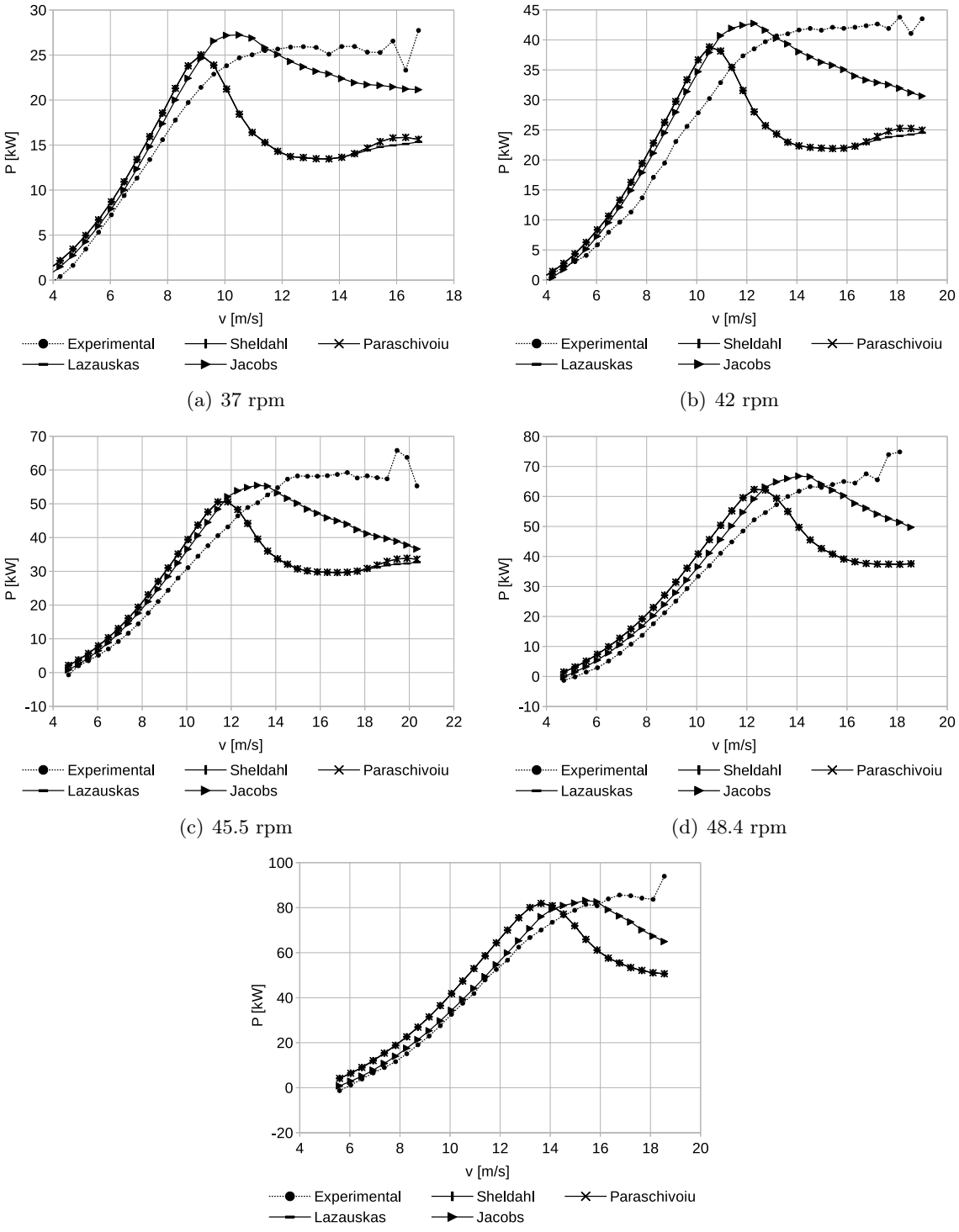

(a) 37 rpm

(b) 42 rpm

(c) 45.5 rpm

(d) 48.4 rpm

(e) 52.5 rpm

Figure 2.16: Power production with respect to the wind speed for the Sandia 17-meter turbine, experimental results compared against simulation results with different aerodynamic databases for five rotational speeds.

previous cases. This could be related to the main difference between this configuration and the previous ones: the presence of two tilted supporting spokes for each blade. Their presence deeply influence the aerodynamic behaviour of the rotor and, since they are profiled as NACA 0012 and tilted, they actively introduce a tangential coefficient C_t which provides additional contributions both to rotor torque and drag, for different operative conditions. Since the basic formulation adopted in the present work does not include any model for the spokes, in order to keep the model simple and not to introduce additional uncertainty factors that would influence the comparison between the databases, their presence is not accounted.

On the other hand the general trend for the power curve is still correctly predicted. The error in the power production is very reduced up to the rotor nominal wind speed for all the rotational speeds. It is possible to observe that Sheldahl, Paraschvioiu and Lazauskas databases provide mainly the same result for wind speed lower than 14 m/s. A small difference is observed for higher wind speeds among Sheldahl/Paraschivoiu and Lazauskas databases because of the glare effect at high angles of attack that is supposed to be corrected only in the second database. The steep decrease after profile stall in all three databases deeply affects the stall characteristics of the turbine, leading to a considerable decrease in the power production. The power decrease is also present adopting the Jacobs database, but with a less steep characteristic. The experimental data highlight a different behaviour for the stalled conditions which can be related to the presence of the spokes and additionally to the dynamic stall, another factor which is not considered in this code and might contribute to a more reliable estimation in these conditions [36].

Overall, the Jacobs database still provides a better result than the other databases in the first part of the power curve and to predict the peak (nominal) power production. The stall production is not correctly predicted because of the limitations in the simulation code more than database reliability.

2.1.2.4 Sandia 42-meter

Sandia National Laboratories published the results for a last turbine with a greater size, 42-meter in height and 34-meter in diameter [100]. This turbine is characterized by a blade which is designed both considering aerodynamics and structural constraints, being tapered with three different profiles. The chord and the thickness indeed decrease from the shaft connection to the rotor equatorial plane in order to lower the centrifugal forces and increase the aerodynamic tangential coefficient. Moreover, the blade shape is not a traditional SCS (Straight-Curve-Straight, a convenient approximation for the Troposkien shape [20]), but with a smaller diameter. The main geometrical details are reported in Table 2.4.

H [m]	R [m]	Profile	c [m]	N_B [-]
41.9	17.1	SNLA 0018-50/NACA 0021	1.22/1.07/0.91	2

Table 2.4: Main geometrical details for Sandia 42-meter rotor [100].

Due to the presence of different airfoils, in this case different databases need to be used. The central part of the rotor is profiled as SNLA 0018-50, a profile which is realized by Sandia National Laboratories derived from NACA 0018 especially for VAWT applications [99]. The database adopted here is only the one provided by Gregorek [46] extended to high angles of attack, since unfortunately no other database are available for these profiles. The Gregorek database is provided for Reynolds numbers between 10^6 and $4.0 \cdot 10^6$ and it is therefore suitable for the simulated operative conditions as shown in Figure 2.17(a). The NACA 0021 coefficients are instead included in the Sheldahl, Lazauskas and Jacobs database and are therefore separately adopted and compared. This profile is only adopted in the blade tips and therefore at a small radius from the shaft: the difference in performance estimation due to the databases is therefore expected to be limited. The variation in the angles of attack along the azimuthal position for the rotor equatorial plane is reported in Figure 2.17(b).

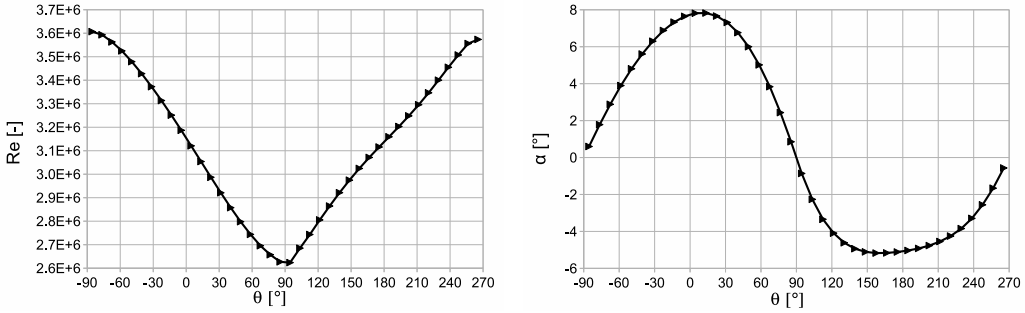

(a) Reynolds number

(b) Angles of attack

Figure 2.17: Reynolds number and angles of attack for the equatorial section of Sandia 42-meter rotor with respect to the azimuthal position during a blade revolution for an operative condition of $\lambda = 6.2$, corresponding to the experimental maximum power coefficient condition.

The results obtained using different databases for NACA 0021 airfoil and the Gregorek database for the SNLA 0018-50 airfoil are reported in Figure 2.18.

The simulation algorithm produces a good estimation for the rotor performance for the rotational speeds of 28 rpm and 34 rpm, whereas for 38 rpm at tip speed ratios lower than 5, the experimental curve experiences a steep decrease which is not followed by the simulated curves. The global agreement of the simulation results confirms that the Gregorek database can be successfully adopted to simulate the SNLA 0018-50 profile in the VAWTs. As expected, the differences in the adopted databases for NACA 0021 do not substantially influence the power coefficient curve since this profile is adopted only in a limited region and for structural

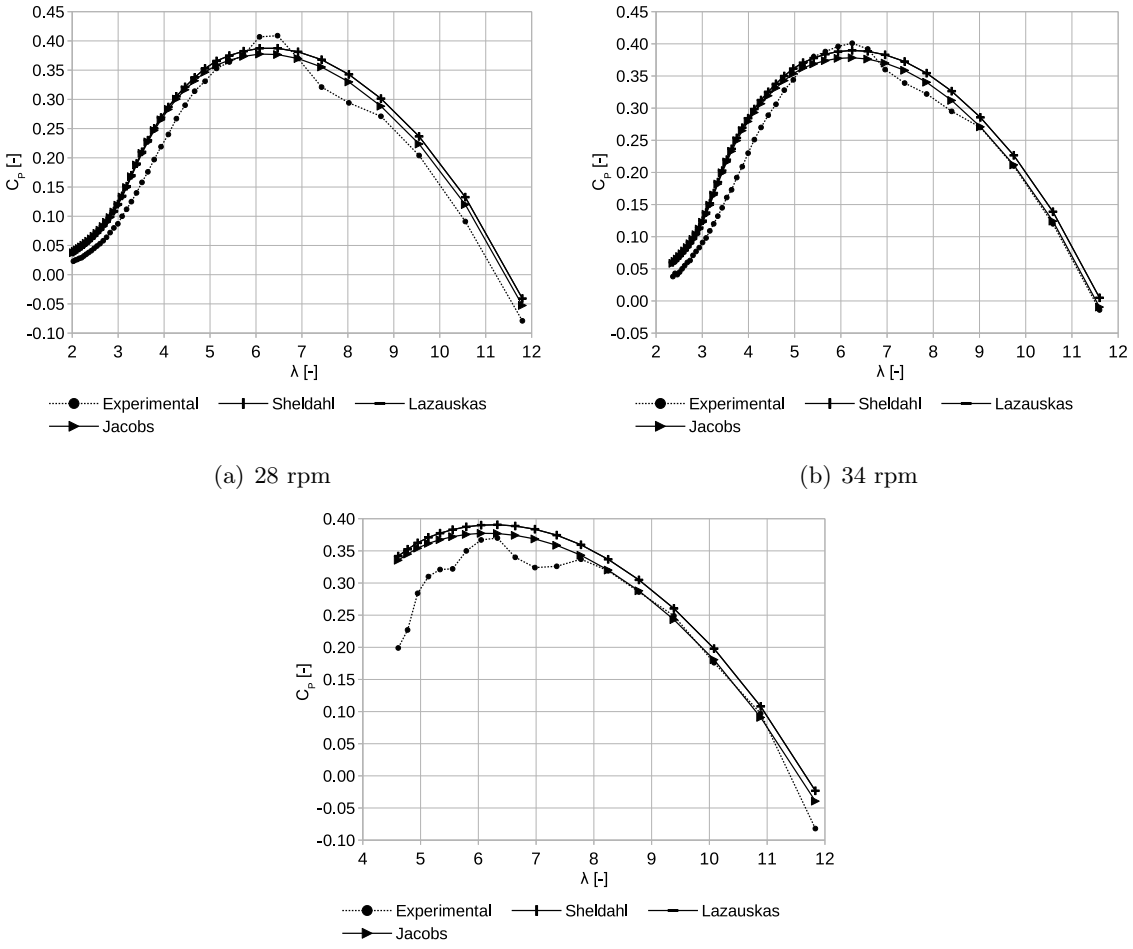

(a) 28 rpm

(b) 34 rpm

(c) 38 rpm

Figure 2.18: Power coefficient with respect to the tip speed ratio for the Sandia 42-meter turbine, experimental results compared against simulation results with different aerodynamic databases for three rotational speeds.

reasons. Anyway, Jacobs database still provides an estimation closer to the experimental values and therefore should be preferred against Sheldahl and Lazauskas databases. A slight overestimation is present for low tip speed ratios, where the rotor experiences stall conditions: this slight overestimation can be probably corrected by introducing a dynamic stall model.

2.1.2.5 Magdalen Island 37-meter

In 1977 a 230 kW VAWT designed and built by DAF Indal Ltd. was installed in Magdalen Islands, Canada [90, 91]. The turbine was characterized by an height of 37-meter and a diameter of 24-meter. The turbine suffered for an overspeed accident and was eventually equipped with an aerodynamic brake. The turbine blade is profiled as a NACA 0018, a profile

which was not adopted in the turbines developed by Sandia. The validation is conducted in order to establish the reliability of the databases for this profile. The main geometrical details are reported in Table 2.5.

H [m]	R [m]	Profile	c [m]	N_B [-]	σ [-]
37	12	SNLA NACA 0018	0.61	2	0.10

Table 2.5: Main geometrical details for Magdalen Island 37-meter rotor [91].

Given the rotor size, the Reynolds numbers expected for this configuration are rather higher with respect to the smaller configurations, as shown in Figure 2.19(a). The databases adopted here are again Sheldahl, Paraschivoiu, Lazauskas and Jacobs, even if for the first three databases the expected difference in the results is small because of the high Reynolds numbers involved. The Jacobs database presents also small differences compared to the other ones, mainly located in the post stall angles of attack, which should not influence extensively the computation since the angles of attack for most of the sectors are lower than 10°, as can be seen in Figure 2.19(b) for the rotor equatorial plane.

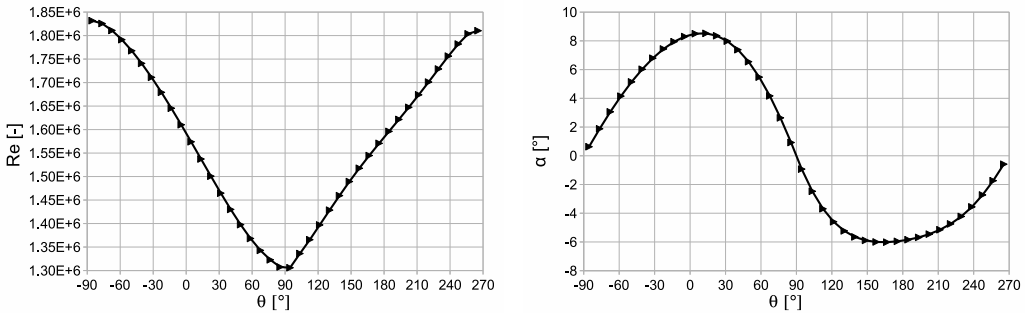

(a) Reynolds number

(b) Angles of attack

Figure 2.19: Reynolds numbers and angles of attack for the equatorial section of Magdalen Islands 37-meter rotor with respect to the azimuthal position during a blade revolution for an operative condition of $\lambda = 6$, corresponding to the experimental maximum power coefficient condition.

The results obtained using different databases for NACA 0018 airfoil are reported in Figure 2.20. Even in this case the comparison is conducted on the power curve since the experimental data for one rotational speed appears to be scattered, probably obtained with a few number of measurements for each rotational speed, leading to a power coefficient curve which is not suitable for comparisons.

The simulations provide results which are very close for wind speed up to the maximum production levels. The prediction in this phase is quite accurate for the higher rotational speed whereas for the lower a discrepancy is registered: the experimental production is lower than the simulated one. On the contrary, for higher wind speeds at 29.4 rpm the experimental production is higher than the predicted: these discrepancies can be related to the dynamic

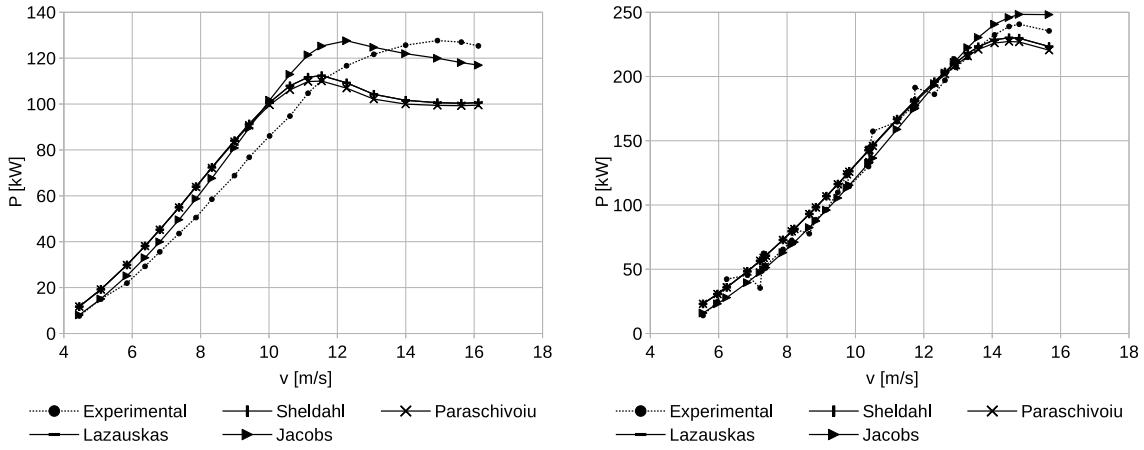

(a) 29.4 rpm (b) 36.6 rpm

Figure 2.20: Power production with respect to the wind speed for the Magdalen Islands 37-meter turbine, experimental results compared against simulation results with different aerodynamic databases for three rotational speeds.

stall phenomena. Instead, the peak prediction is quite accurate with the Jacobs database whereas the other databases provide an underestimated production. This is mainly related to the difference in the lift coefficient among the databases, as can be observed in Figure 2.7. Jacobs estimation is higher and the result turns to be more reliable. For higher rotational speeds, the curve is limited to pre-stall conditions because on the test site only in few occasion the wind speed was higher than 15 m/s. The predictions are reliable generally with all the databases, even though it is still possible to observe an underestimation using the Sheldahl/Paraschivoiu/Lazauskas coefficients.

All the databases generally provide a good estimation for the turbine performances but Jacobs database should still be the preferred choice to simulate turbines operating at high Reynolds numbers and adopting NACA 0018 airfoils because of the correct peak prediction.

2.1.3 Conclusions

This work presents a review on the different aerodynamic databases available in the literature which can be used for VAWT simulations combined with Blade Element Momentum algorithms. The databases should include airfoil coefficients at low Reynolds numbers and for angles of attack from $-180°$ to $+180°$. Some databases included in the comparison were already provided with these characteristics, others are extended conducting some assumptions, in order to extend the comparison pool.

The Double Disc Multiple Streamtube BEM simulation without any correction model provided

already a good result with most of the databases, although limitations linked to the dynamic stall operative conditions and spoke presence are highlighted. Recommendation on the database choice can be however drawn in order to select the most reliable one with respect to the applicative case. Especially for rotors operating at low Reynolds numbers, the widely diffuse Sheldahl database and the derived databases from Paraschivoiu and Lazauskas largely affect the computation result leading to under-predicted performances due to the under-estimation of the lift coefficient in post-stall conditions. This result is clearly depicted in the Sandia 2-meter and 5-meter simulations, where the computation is completely unreliable for low tip speed ratios since the performance drop to unrealistic values. On the other hand, for higher Reynolds numbers this effect is still present but with a more limited influence.

Overall, the adoption of the extended Jacobs database is recommended for all the VAWT computations, since the estimation reliability was always higher or equal with respect to the other databases. Although the database was extended using the aerodynamic coefficient from Sheldahl for high angles of attack, its inaccuracy is limited to a small amount of sectors of the blade and does not affect the overall computational results.

2.2 Discrete Vortex Model

The objective of this section is to derive and prove the validity of an enhanced two-dimensional discrete vortex model to predict the dynamic behavior of a symmetrical airfoil. The proposed model is based on a discrete vortex scheme, where the airfoil is approximated into a series of flat plate elements, each of them represented by a single lumped vortex located at the center of pressure of the element itself (i.e. at the quarter-chord, according to the flat plate theory). In the present model, a number of flat elements equal to 8 is considered: the assumption will be confirmed to be reasonable, as shown in the non-oscillating steady state condition validation. The boundary condition of zero normal flow for each flat plate element is imposed, which means that the airfoil is considered as a streamline, in formula:

$$\mathbf{V_{tot,i}} \cdot \mathbf{n_i} \;=\; 0 \tag{2.18}$$

where $\mathbf{V_{tot,i}}$ and $\mathbf{n_i}$ are respectively the air velocity vector for the i^{th} panel and the unit normal vector. The normal velocity is computed at the three-quarter-chord of each element to fulfil the Kutta condition at the airfoil trailing edge [50].

The influence of the lumped vortex in any point of the flow field is computed by:

$$\mathbf{V_i} = \frac{\Gamma_i}{2\pi r_i}\mathbf{e} \tag{2.19}$$

where Γ_i is the vortex strength, r_i is the distance from the vortex center to the point where the induced velocity is computed and $\mathbf{e}$ is the unit vector in the direction of $\mathbf{r_i} \times \mathbf{\Gamma_i}$.

In order to simulate an unsteady flow, a shedding wake is added to this scheme: the airfoil's circulation changes in time and the discrete vortex wake elements are shed from the trailing edge at every time step. The wake and the airfoil circulation must fulfil the Kelvin's law, which imposes the total circulation generated in the flow to be zero, in formula:

$$\frac{D\Gamma}{D\zeta} = 0 \tag{2.20}$$

The model can be extended to separated flows around airfoils at high angles of attack introducing a shear layer which is emitted from a separation point in the suction side of the airfoil, as proposed by Katz [55] and shown in Figure 2.21(a), at a fixed distance normal to the airfoil chord. The adopted distance is obtained through the validation with non-oscillating steady state condition data, as explained below. The chord-wise coordinate of the separation point (which is a function of Reynolds number, airfoil type and angle of attack) and the strength of the separated wake vortex are evaluated considering the following semi-empirical model.

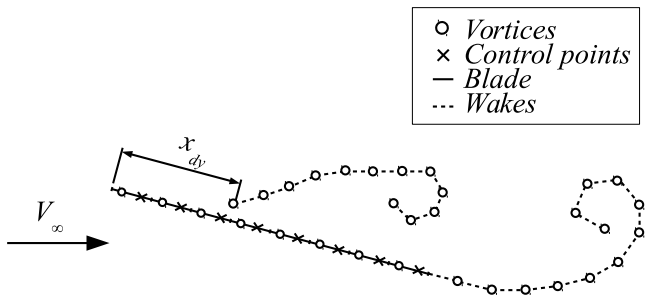

(a) Airfoil and wakes representation

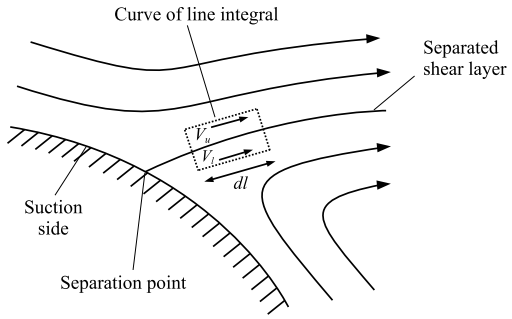

(b) Integration path on the separation line

Figure 2.21: Schematic description of the adopted model [55].

The intensity of the vortex shed at the separation point can be estimated considering a line integral enclosing part of the shear wake just behind the separation point itself [55], as can

be seen in Figure 2.21(b), which yields to:

$$\frac{d\Gamma_s}{d\zeta} = \frac{d}{d\zeta} \oint \mathbf{V} \cdot d\mathbf{l} = \frac{1}{2} \left(V_u^2 - V_l^2 \right) \tag{2.21}$$

where Γ_s is the circulation strength generated at the separation point, $\mathbf{V}$ is the velocity vector, $d\mathbf{l}$ is the integration length, V_u is the upstream wind speed with respect to the shear layer and V_l is the downstream wind speed. A circulation reduction factor c_f is introduced (since not all the vorticity generated in the boundary layer is injected in the flow field at the separation point), whose value is set to 0.6, as proposed by Katz [55]. The strength of the latest separated wake element is therefore:

$$\Gamma_s = \frac{c_f}{2} \left(V_u^2 - V_l^2 \right) \Delta\zeta \tag{2.22}$$

On the basis of a weighted average of the the experimental results obtained from Fage & Johansen [101], for the present model a constant upper velocity of $V_u = 1.4v$ and a constant lower one of $V_l = 0$ is suggested, leading to a constant value for the strength of the latest vortex shed at the separation point and therefore neglecting minor fluctuations.

The position of the separation point is first estimated as if the lift on the airfoil was generated by a flat plate in a potential Kirchhoff flow [67], in formula:

$$x_{st} = \left(2\sqrt{\frac{C_L}{C_{L,\alpha} \cdot \alpha}} - 1 \right)^2 \tag{2.23}$$

where C_L is the non-oscillating steady state lift coefficient and $C_{L,\alpha}$ is the linear lift slope. The non-oscillating steady state lift coefficients provided by experimental data for a fixed Reynolds number of $1.35 \cdot 10^5$ and for the NACA 0012 airfoil are considered in the present work. The separation point coordinates are afterwards slightly adjusted to fit the computed non-oscillating steady state lift coefficients with the database values. The normal distance of the latest shed vortex from the airfoil chord is then investigated: the position of this vortex is of crucial importance since it can lead to numerical problems in the computation of the induced velocities, if placed on the chord line or very close to it, or to incorrect physical description of the problem, if placed at large distances. Within this range, different normal distances are investigated, namely $0.03c$, $0.05c$, $0.07c$ and $0.09c$. For distances of $0.03c$, $0.07c$ and $0.09c$ the lift coefficient estimation was observed not to be reliable for the considered range of angles of attack (between 0° and 25°). On the other hand, a normal distance equal to $0.05c$ ensures the algorithm convergence and provides values similar to the flat plate case: such distance is therefore assumed for the proposed computations. The evolution of the lift coefficient as a function of the angle of attack and the comparison between the estimated (flat plate) separation points and the corrected ones are shown in Figure 2.22.

The generation of the circulation due to the separated flow has to be taken into account in order to fulfil the Kelvin's law:

$$\frac{D\Gamma}{D\zeta} = \Gamma_b(\zeta) - \Gamma_b(\zeta - \Delta\zeta) + \Gamma_w + \Gamma_s = 0 \tag{2.24}$$

where Γ_b is the total bound circulation of the airfoil, Γ_w is the strength of the latest vortex shed at the trailing edge and Γ_s is the strength of the latest vortex shed at the separation point.

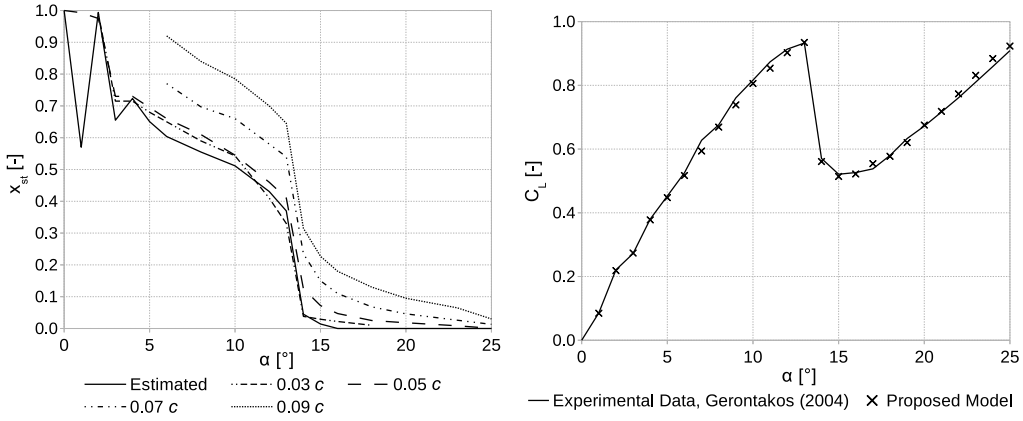

(a) Estimated vs corrected separation points as a function of the normal distance of the separation point from the chord line

(b) Non-oscillating steady state results

Figure 2.22: Non-oscillating steady state validation of the vortex model, NACA 0012 at $\mathrm{Re} = 1.35 \cdot 10^5$.

In order to correctly reproduce the effect of the dynamic stall, a delay in the movement of the boundary layer separation point needs to be considered, as reported by Hansen et al. [68]. An estimation of the dynamic separation point can be obtained from the non-oscillating steady state separation one, in formula:

$$x_{dy}(\zeta + \Delta\zeta) = x_{st} + (x_{dy}(\zeta) - x_{st})\, e^{\left(\frac{\Delta\zeta}{\tau}\right)} \tag{2.25}$$

where x_{st} and x_{dy} are respectively the separation point for steady and unsteady conditions and τ is the time constant, which in this model is set to $4c/v$ as suggested by Hansen et al. [68].

A viscous vortex model, which allows to avoid singularity conditions in the induced velocity calculation and to reproduce the vortex decay in time, is additionally included. This is particularly necessary in a VAWT rotor simulation, where the blades and the wakes collide and interfere at different times due to the rotor circular motion. The hereby adopted model was first proposed by Vatistas et al. [64], obtaining good agreement with experimental results.

The swirl-velocity profile generated by an infinite straight vortex becomes:

$$\mathbf{V_i} = \frac{\Gamma_i}{2\pi}\left(\frac{r_i}{\left(r_c^{2n} + r_i^{2n}\right)^{(1/n)}}\right)\mathbf{e} \tag{2.26}$$

where r_c is the vortex core radius and n is an integer determining the flow velocity shape. In this work n was assumed equal to 2, leading to a close approximation of the Lamb-Oseen Model, which provides a good approximation of the experimental results [102, 103]. The vortex core radius is modelled as a time dependent solution, being the vortex viscosity included to take into account the effects of vortex growth and initial finite vortex core [104]:

$$r_c\left(\zeta\right) = \sqrt{r_{c_0} + 4\alpha_L \nu \left(1 + a_1 \mathrm{Re}_v\right)\zeta} \tag{2.27}$$

where r_{c_0} is the initial vortex core radius, set to $0.10c$ as proposed by Bhagwat & Leishman [65], α_L is the Oseen parameter [105] equal to 1.25643, ν is the kinematic viscosity, a_1 is the Squire's parameter set to $2 \cdot 10^4$ according to the experimental measurements performed by Bhagwat & Leishman [103], which describes adequately the vortex core growth, and Re_v is the vortex Reynolds number ($\mathrm{Re}_v = \Gamma_v/\nu$).

Some remarks have to be made on the Kutta condition for unsteady flows. Very high oscillating frequencies, large amplitudes and high angles of attack may cause trailing edge separation, thus violating the Kutta condition. This situation was investigated with experimental studies by Archibald [106] and Poling & Telionis [107] concluding that, even though the Kutta condition is no more valid, the variations in both lift and pressure distribution can be neglected.

The model is solved for successive time steps considering one equation for the Kelvin's law (eq. 2.24) and N equations for the no-penetration boundary condition, in formula:

$$\mathbf{V_{tot,i}} \cdot \mathbf{n_i} = \left(\mathbf{v}_\infty + \mathbf{V_b} + \mathbf{V_w} + \mathbf{V_s} - \mathbf{V_r}\right)_i \cdot \mathbf{n_i} \;=\; 0 \tag{2.28}$$

where $\mathbf{V_b}$, $\mathbf{V_w}$ and $\mathbf{V_s}$ are respectively the foil, wake and separated wake induced velocities and $\mathbf{V_r}$ is the velocity due to the motion of the i^{th} panel. The N+1 unknowns are the circulation strengths of the N panels and of the most recent element in the trailing edge wake, whereas the remaining vortex intensities in the trailing edge wake and in the separated one are known.

Every induced velocity can be expressed as a linear combination of the vortex strength

multiplied by an influence factor $a_{i,j}$. The system of equations takes the form:

$$\begin{pmatrix} a_{1,1} & a_{1,2} & \cdots & a_{1,N} & a_{1,W} \\ a_{2,1} & a_{2,2} & \cdots & a_{2,N} & a_{2,W} \\ \vdots & \vdots & \ddots & \vdots & \vdots \\ a_{N,1} & a_{N,2} & \cdots & a_{N,N} & a_{N,W} \\ 1 & 1 & \cdots & 1 & 1 \end{pmatrix} \begin{pmatrix} \Gamma_1 \\ \Gamma_2 \\ \vdots \\ \Gamma_N \\ \Gamma_w \end{pmatrix} = \begin{pmatrix} RHS_1 \\ RHS_2 \\ \vdots \\ RHS_N \\ \Gamma_b\left(\zeta - \Delta\zeta\right) \end{pmatrix} \tag{2.29}$$

where RHS_i is the right hand side, which includes the constant values induced by the wakes apart from the latest trailing edge wake vortex. The airfoil circulation is then computed as the sum of the panels' circulation strength, in formula:

$$\Gamma_b\left(\zeta\right) = \sum_{i=1}^{N} \Gamma_{b,i} \tag{2.30}$$

and the lift coefficient follows using the Kutta-Joukowski Theorem:

$$C_L = \frac{2\Gamma_b}{v_\infty c} \tag{2.31}$$

The drag coefficient is not considered since the viscous analysis of the airfoil boundary layer is still not modeled: the drag force estimation would be therefore not reliable in the whole operative range.

Each vortex moves downstream with the local absolute velocity, since vortex wakes are force-free. In each time step, the vortex element displacements are calculated by:

$$\left(\Delta x, \Delta y\right)_j = \mathbf{V_{tot,j}} \cdot \Delta\zeta \tag{2.32}$$

The latest vortex element of both trailing and separated wakes is placed at half of the distance travelled by the airfoil during one time step, in order to obtain an efficient wake discretization [56].

The choice of the time step, as suggested by Katz [55], must fulfil the following boundaries in order to produce good results:

$$0.05 < \frac{\Delta\zeta \ v_\infty}{c} < 0.2 \tag{2.33}$$

A value of 0.1 is chosen in the present model.

2.2.1 Experimental Data

The experimental data provided by Gerontakos [73] are used in the present work as reference values: the experiment was conducted in a subsonic wind tunnel with a cross section area of 120×90 cm^2 and a length of 270 cm. A sinusoidally oscillating airfoil (equipped with two tip plates of 30 cm diameter to avoid three-dimensional flows due to the tip effects) was considered and its aerodynamics was investigated at $\mathrm{Re} = 1.35 \cdot 10^5$ by means of closely-spaced multiple hot-film sensor arrays supplemented by surface pressure measurements, hot-wire wake velocity surveys and smoke-flow visualizations. The gaps between the oscillatory airfoil and the stationary tip plates were kept within 1 mm to minimize the leakage of the blade-tip flow [108]. These aspects allow therefore to assume the flow to be two-dimensional and suitable for this study. Pitching reduced frequencies between 0.025 and 0.100 were investigated, in formula:

$$k = \frac{\pi f c}{v_\infty} \tag{2.34}$$

being f the pitching frequency, c the airfoil chord and v the unperturbed freestream wind speed. The angle of attack varies with the following law:

$$\alpha[^\circ] = 10 + 10 sin(2\pi f \zeta) \tag{2.35}$$

being ζ the time.

The sinusoidal motion of the airfoil at the considered reduced frequencies are closely related to the operating conditions in the blade airfoil of a Darrieus turbine [108] and therefore the validation on these experimental data is considered reliable.

2.2.2 CFD Analysis

In order to accurately reproduce the flow over the pitching NACA 0012 airfoil, a full campaign of two-dimensional Computational Fluid Dynamics (CFD) analyses based on the Unsteady Reynolds-Averaged Navier-Stokes (URANS) equations is performed. As shown in Figure 2.23, the fluid domain is subdivided into 2 regions: a circular rotating inner zone enclosing the airfoil and embedded within a stationary outer zone (covering the whole external computational domain and characterized by a circular opening, centred on the airfoil aerodynamic centre). The inlet is located at $30c$ upwind from the airfoil center of pressure and a *velocity inlet* boundary condition is imposed, with a velocity of 14 m/s and a gauge pression of 0 Pa. The turbulence conditions were specified through the turbulence intensity and the viscosity ratio parameters, which are set respectively to 0.08% and 10 [108]. The outlet is located at

$60c$ downwind from the airfoil center of pressure and a *pressure outlet* boundary condition is imposed, with a gauge pression of 0 Pa. These boundary conditions are placed far enough to obtain an uniform free-stream velocity before the airfoil [108] and to allow the full development of the wake. The side boundaries of the domain are set to *symmetry* and located at $30c$ from the airfoil center of pressure, to avoid blockage effects. No roughness was considered along the airfoil surface.

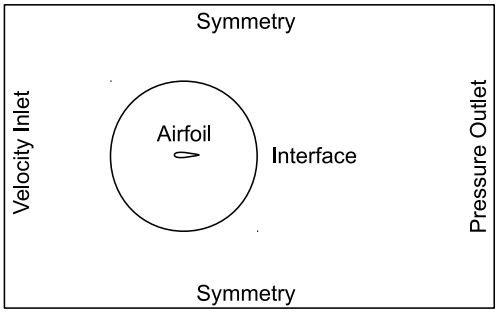

Figure 2.23: Boundary conditions of the computational domain.

Figure 2.24 shows some details of the adopted hybrid structured/unstructured mesh: 225 nodes are placed on both the pressure and the suction sides of the airfoil, at a distance of $3.31 \cdot 10^{-4}c$ from the walls, to obtain an y^+ close to 1. The structured grid is composed of 40 rows clustered around the airfoil surface with a growth rate of 1.05.

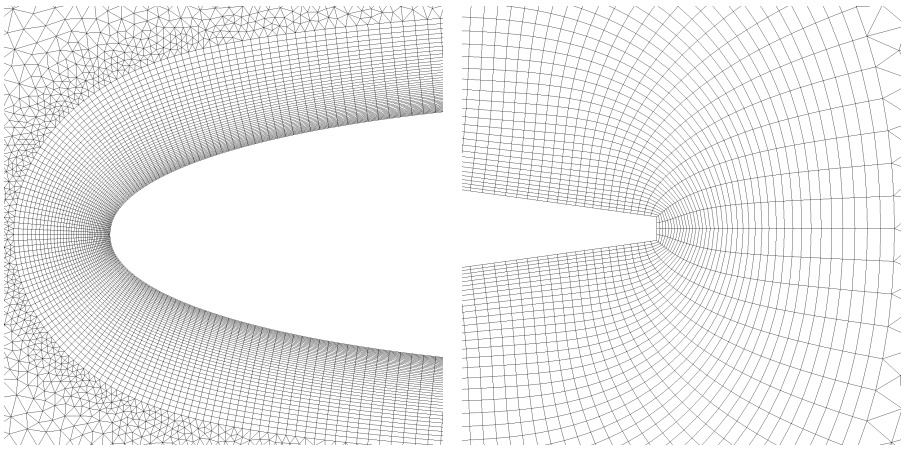

(a) Leading edge (b) Trailing edge

Figure 2.24: Near blade mesh.

The non-linear governing equations for the conservation of mass, momentum and turbulence are solved by the commercial software Ansys Fluent 14, which is based on a finite volume method. A coupled scheme with a second order spatial discretization is adopted, with the absolute residuals set to 10^{-5}, since lower orders would not lead to significant solution variations. The pitching motion of the airfoil (and of the circular rotating inner grid) is imposed by means of an User-Defined Function (UDF). The time step is computed to obtain

a value of the Courant number below 0.15 [109] at the interface between the rotational and the stationary domains. The independence of the solution from the mesh size was obtained with successive refinements, until almost identical results near the airfoil and in the wake region were registered.

To correctly predict the flow around the pitching airfoil, several turbulence models are considered: $k-\epsilon$ standard, $k-\epsilon$ realizable, $k-\omega$ standard, $k-\omega$ SST, Spalart-Allmaras [69]. The enhanced wall treatment is considered for the $k-\epsilon$ models. The average error in the lift coefficient estimation for the different models is reported in Table 2.6. The $k-\omega$ SST model is chosen due to its lowest average error compared to the experimental data for a reduced pitching frequency of $k = 0.025$. In fact, as can be clearly seen in Figure 2.25, the other models fail to predict both the deep stall zone of the curve and the downstroke phase of the hysteresis cycle because of the inability to simulate flows with large separation regions and severe adverse pressure gradients [108].

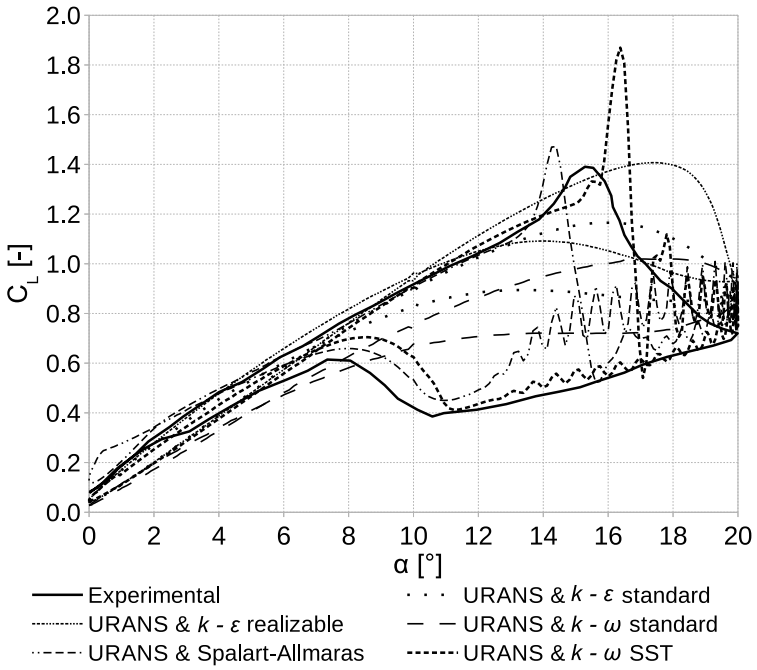

Figure 2.25: URANS validation, NACA 0012 at Re $= 1.35 \cdot 10^5$, $k = 0.025$.

Table 2.6: Average error in the lift coefficient estimation for different turbulence models, pitching frequency of $k = 0.025$

Model	Average Error [%]
$k-\epsilon$ standard	5.40%
$k-\epsilon$ realizable	7.54%
$k-\omega$ standard	5.02%
$k-\omega$ SST	2.29%
Spalart-Allmaras	3.63%

2.2.3 Simulation Results

The lift coefficient estimations from the proposed vortex model for the pitching NACA 0012 airfoil are shown in Figure 2.26, as well as the experimental data from Gerontakos [73] and the results of the CFD simulations for different pitching reduced frequencies.

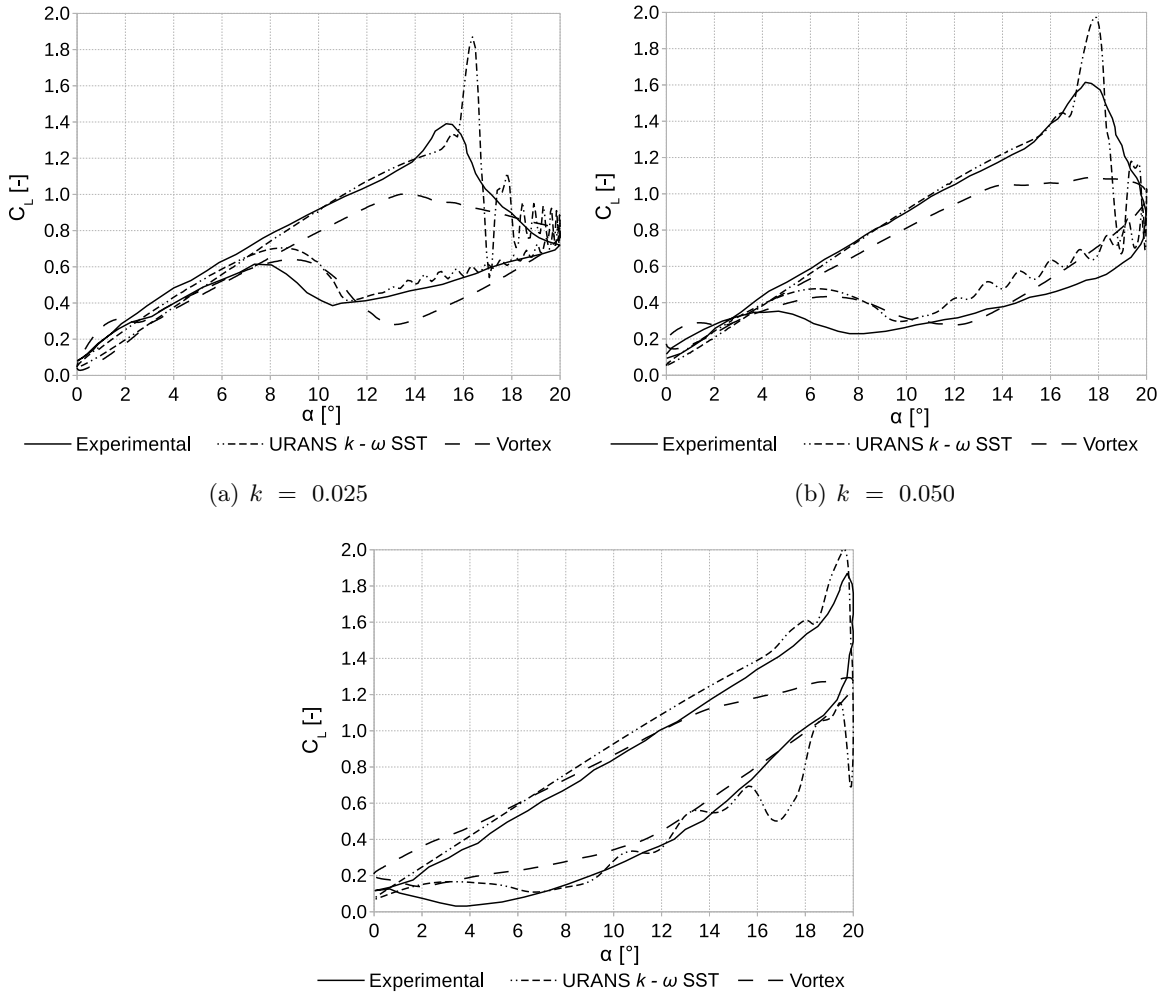

(a) $k = 0.025$

(b) $k = 0.050$

(c) $k = 0.100$

Figure 2.26: Comparison between experimental, URANS $k - \omega$ SST and vortex results for different pitching reduced frequencies, NACA 0012 at Re $= 1.35 \cdot 10^5$.

For increasing angles of attack (from 0° to approximately 14°), the lift coefficient and the curve slope provided by the Vortex code are reliable, but slightly underestimated with respect to both the CFD and the experimental data for pitching reduced frequencies of $k = 0.025$ and $k = 0.050$. The results obtained for the highest pitching frequency ($k = 0.100$) are instead superimposed to the experimental one.

For angles of attack between 15° and 20° (i.e. where the experimental lift coefficient reaches

the maximum value), the CFD code clearly over-predict the lift coefficient whereas the vortex model is more conservative. The CFD over-prediction is linked to the sharp lift coefficient drop-off after the stall, which brings to a bad prediction of the flow reattachment in the down-stroke phase, as observed also by Wang et al. [110] for the transition SST model. The CFD result is also characterized by high oscillations linked to the two-dimensional simulation, as observed by Wang et al. [108] and Martinat et al. [111]. The vortex model provides a lift coefficient curve very close to the average values from CFD. The model however provides an underestimation of the peak lift coefficient, linked to an overestimation of the vortex intensity in the separated wake.

A great reduction in the overall computational time is achieved using the proposed model (1 hour against more than 24 hours required by the CFD calculations on a desktop computer equipped with an Intel i7-870 CPU and 16 GB RAM).

2.2.4 Conclusions

A Vortex model is presented, which includes a separated wake to simulate the deep stall behavior and dynamic models for both the separation point and the vortex intensity evolution. Good results are obtained in the non-oscillating steady state case and the model capabilities in predicting the dynamic stall are investigated.

The predicted hysteresis in the lift coefficient is compared to both experimental data and CFD simulations. The most reliable results are obtained for the highest pitching frequency ($k = 0.100$), while a lower accuracy is registered for the lower pitching frequencies ($k = 0.025$ and $k = 0.050$), where further investigation is required. CFD URANS $k - \omega$ SST simulations are also conducted for comparison with Vortex. The results are reliable compared to experimental data except for the overestimation of the peak lift coefficient. A better agreement is again obtained for the highest pitching frequency.

A reliable estimation of the dynamic lift coefficient is achieved by the proposed model, especially for high airfoil pitching frequencies. The reduced computational requirements prompt for its adoption to provide aerodynamic data for unsteady computations and optimization.

2.3 2D URANS CFD

The commercial software Ansys Fluent 14.5 [112] is adopted to perform the URANS CFD simulations of a two-blade rotor. An unsteady solver is selected, considering the required time for the rotor to perform an azimuthal rotation of 1° as a fixed time-step [113]. The $k-\omega$ SST turbulence model is adopted due to the highest reliability of the results and its flexibility in the wall boundary treatment [114]. The spatial and temporal discretizations are performed considering second order schemes. Every time step is considered as converged when the maximum residual value fell below 10^{-4}. The rotor torque varies in every time step due to the Darrieus unsteady aerodynamics: the mean torque value is calculated in every rotational period and the simulation is considered as finalized when the difference between two consecutive periods was below 1%.

The computational domain is divided in two sub-domains, *gallery* and *cylinder* in order to impose the rotor motion in the cylinder domain and different mesh densities. The two-dimensional domains, as well as the sizes and the boundary conditions, are shown in Figure 2.27. A velocity inlet boundary is imposed at the inlet, considering an uniform wind speed, varied in the simulation to reproduce the whole experimental curve. The outlet is considered as a pressure outlet, with a relative pressure of 0 Pa. The remaining *gallery* boundaries are set as symmetry, since these are placed far enough not to be influenced by the rotor activity. A mesh motion is imposed for the *cylinder* domain, with a rotational speed equal to the experimental value. The quantities are exchanged between the fixed and rotating grid domains adopting a sliding mesh approach [112]. The forces computed on the blade walls are used to estimate the rotor torque. The two domains are connected by means of an interface boundary condition. The central tower is neglected in the model due to the lack of information about its geometry, its presence only in the bottom half of the rotor and the limited effect of its wake, which only affects the downwind production [29, 113, 115, 116].

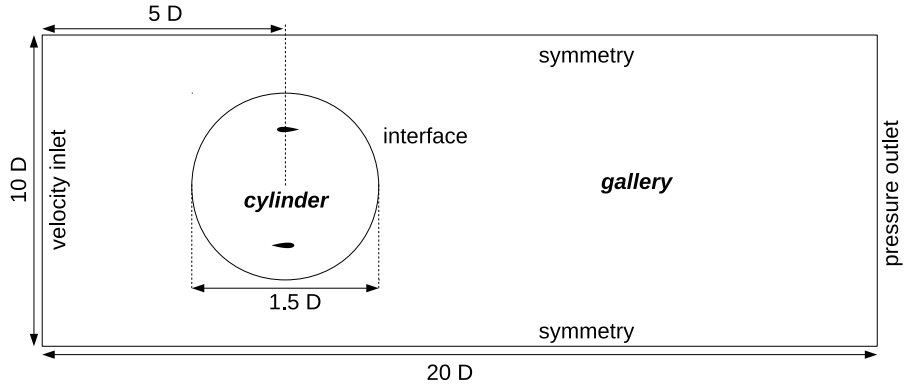

Figure 2.27: Scheme of the computational domains with boundary conditions and sizes with respect to the rotor diameter D, not to scale.

2.3.1 Experimental Data

The experimental data from the open-field test conducted by Mays et al. [117] on a two-blade 500 kW Darrieus vertical axis wind turbine are considered for the validation of the URANS CFD simulations. This configuration was chosen as the presence of two blades only limits the number of elements in the mesh and therefore reduces the computational time. The rotor geometrical specifications are reported in Table 2.7, while a picture of the installation is shown in Figure 2.28. The simulations are performed considering the experimental operative conditions, i.e. fixed rotational speed of 13.62 rpm.

Blade length [m]	24.3
Rotor diameter [m]	35 m
Blade profile [-]	NACA 0018
Mean chord [m]	1.75
Blade taper [%]	25%
Rotor solidity [-]	0.10

Table 2.7: Main geometrical features of the baseline rotor configuration.

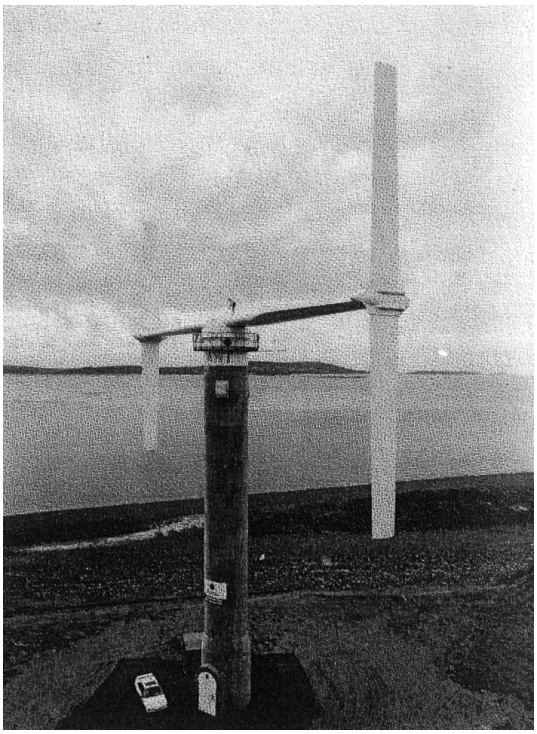

Figure 2.28: 500 kW Darrieus wind turbine installation (from: [117]).

2.3.2 Simulation Results

The mesh grid is generated considering a hybrid approach. The boundary layer near blade walls is discretized with a structured O-Grid mesh. The first element height is defined by the y^+ condition, imposed to be lower than 1 to maximize the turbulence model reliability. The number of mesh extrusion steps was set to 60, enough to capture the boundary layer effect on the blade airfoil. The external mesh is discretized with an unstructured mesh, whose triangular cells have an average size increasing from the blades to the domain interfaces and external walls. The main parameters for the baseline mesh generation are reported in Table 2.8 whereas the mesh for the blade walls and for the rotating domain is shown in Figure 2.29.

Number of elements on the blade airfoil [-]	1204
Leading edge spacing [mm]	0.001
Trailing edge spacing [mm]	0.001
First layer height [mm]	0.008
Growth rate [-]	1.1
Boundary Layer Extrusion Steps	60
Cylinder wall mean element size [m]	1
Gallery wall mean element size [m]	5
Volume mesh growth rate [-]	1.15
Element count [-]	248000

Table 2.8: Geometrical parameters of the simulation mesh.

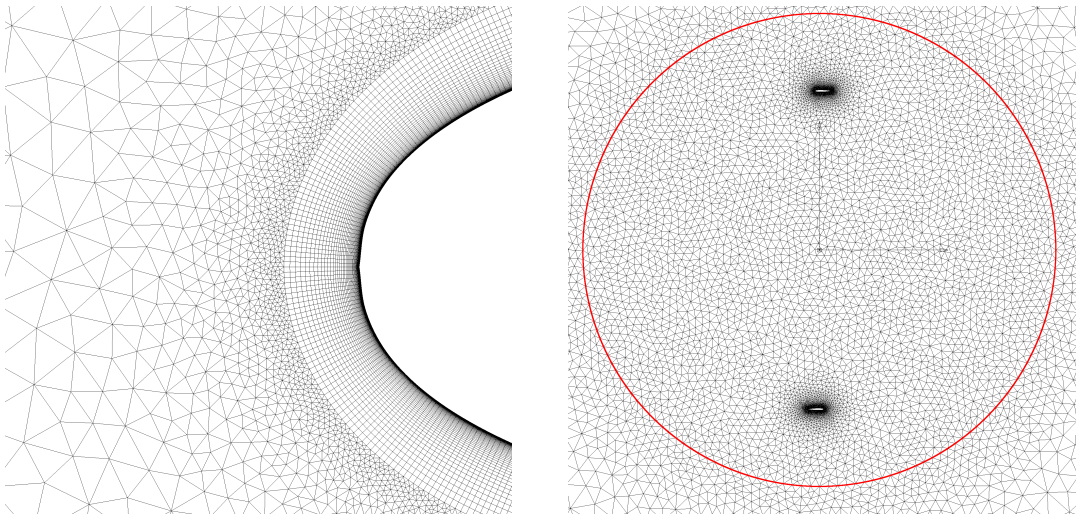

(a) Hybrid mesh near the airfoil leading edge.

(b) Unstructured mesh for the rotating domain, with the interface highlighted in red.

Figure 2.29: Representation of the mesh near the blade walls and for the rotating domain.

The comparison between the experimental results and the simulation estimations for the power production at different wind speeds is reported in Figure 2.30. A power production overestimation is registered in the whole operative range comparing to the experimental

results. A sensitivity analysis is conducted on the main geometrical characteristics of the mesh, i.e. the element count and boundary layer steps, to establish the relevance of these parameters with respect to this overestimation. Two operative point are chosen: the optimization target wind speed, 7 m/s, and the experimental stall wind speed, 12 m/s. The variation of the power with respect to different mesh densities and boundary layer steps is reported in Table 2.9 (the small variations are not noticeable in the power curve). The computational time required on a desktop computer equipped with a quad-core Intel i7-860 processor for each mesh to converge in a single tip speed ratio and the number of elements is reported in Table 2.10.

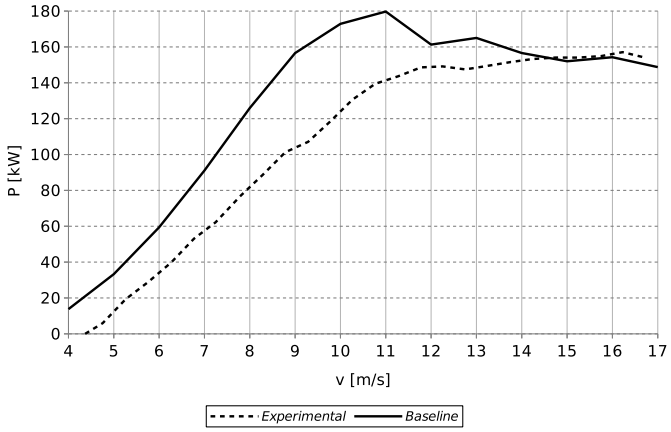

Figure 2.30: Experimental data and simulation results for the 500 kW wind turbine operating at 13.62 rpm.

v [m/s]	Mesh 0.50x	Mesh 0.75x	Mesh 1.25x	Mesh 1.50x	BL 40 Layers	BL 50 Layers	BL 70 Layers
4	0.86%	0.08%	-0.37%	-0.13%	3.50%	-0.37%	0.27%
5	0.27%	0.06%	-0.12%	-0.02%	1.37%	-0.35%	0.21%
6	0.05%	-0.08%	-0.11%	-0.12%	0.62%	-0.58%	0.12%
7	-0.09%	0.04%	-0.03%	-0.19%	0.25%	-0.75%	0.13%
8	-0.39%	0.06%	-0.05%	-0.24%	-0.63%	-1.52%	0.26%
9	-0.51%	-0.05%	-0.13%	-0.37%	-2.63%	-2.76%	0.62%
10	-0.53%	0.10%	-0.19%	-0.46%	-3.79%	-3.40%	0.80%
11	0.59%	1.22%	-0.28%	-0.69%	-5.05%	-4.42%	1.69%
12	0.33%	0.32%	-0.41%	-0.69%	-4.16%	-4.11%	2.10%

Table 2.9: Percentage power variation with respect to the baseline mesh considering different mesh densities and boundary layers steps.

Mesh	Number of Elements [-]	Computational Time [h]
baseline	248000	24
Mesh 0.50x	118200	12
Mesh 0.75x	181000	16
Mesh 1.25x	320100	30
Mesh 1.50x	397000	34
BL 40 Layers	200200	16
BL 50 Layers	224000	20
BL 70 Layers	272200	28

Table 2.10: Number of elements and computational time required on a desktop computer equipped with a quad-core Intel i7-860 processor to converge in a single tip speed ratio for each mesh.

2.3.3 Conclusions

Finer meshes lead to numerical results with a percentage difference less than 5% for the considered operative points. Therefore, the overestimation in the numerical results can not be linked to mesh quality issues. The reason can be found by considering that tower presence, tip and three-dimensional effects are neglected in the two-dimensional simulations, therefore increasing the estimated efficiency of the rotor. Moreover, no spikes are introduced in the simulation, which usually strongly affect the rotor aerodynamics by reducing the performance. Three dimensional URANS $k-\omega$ SST simulations conducted with lower density mesh on Darrieus rotors provided in fact accurate results in the whole rotor operative range [115]. However, both the required computational power, up to 64 GB of RAM, and computational time, up to 18x, is dramatically increased, leading to exclude this simulation approach for the present optimization purposes. On the other hand, the overestimation linked to the present simulation is uniform up to the rotor stall, which is found at a lower wind speed than experimental data. Three dimensional effects, in fact, typically delay the stall angle with respect to the case of an infinite-span blade having equivalent section [118]. Considering its accuracy, the two dimensional simulation is therefore accepted for the optimization procedure. Among the different meshes, the baseline mesh is selected since a deeper insight on the airfoil aerodynamics is achieved at the price of a slightly increased computational time.

2.4 3D URANS CFD

The 3D URANS CFD simulations are conducted employing the commercial software Ansys Fluent 14.5 [112]. The adopted turbulence model is the $k-\omega$ SST. This model was chosen due to its accuracy and reliability to predict complex aerodynamics under a wide of fluid flow conditions, including cases with adverse pressure gradients acting on two-dimensional

airfoils [113, 119]. The introduction of a blending function, which combines the Wilcox $k-\omega$ model and the standard $k-\epsilon$, ensures that the model equations behave appropriately in both the near-wall and far-field zones. In the near-wall boundary, the k equation of the $k-\omega$ SST model is treated in the same way as the k equation of the $k-\epsilon$, which relies on the enhanced wall treatment approach. This means that for spatial discretizations concentrated towards the wall, which are defined by values of the dimensionless wall distance y^+ [112] close or lower than the unity (hereinafter referred as "fine meshes"), the appropriate low-Reynolds-number boundary condition is applied, while the wall function approach is used for meshes characterized by y^+ values larger than unity, hence properly taking into consideration the inner layers of the boundary layer. [112]. The simulation is set to unsteady with a timestep equal to the time needed for the rotor to perform an azimuthal rotation of 1 degree. The spatial and temporal discretizations are performed considering second order schemes. The time-step converges when the scaled residual values [69] fell below 10^{-5}, since lower values would not lead to sensible difference in the estimations [29]. The rotor torque varies in every time step due to the simulation unsteadiness. The final average torque value T is estimated when the simulation is considered as periodic, i.e. when the difference between average torque values in sequential rotational periods is lower than 1%. This value is adopted to compute the power production P and the power coefficient C_P, in formulas:

$$C_P = \frac{P}{0.5 \cdot \rho \cdot A \cdot v^3} = \frac{T \cdot \omega}{0.5 \cdot \rho \cdot A \cdot v^3} \tag{2.36}$$

The Sandia turbine is modelled as a three-blade rotor with the physical characteristics reported in Table 2.11. The three blades are connected with each other on the top and the bottom of the rotor through the introduction of two truncated cones. The central shaft is disregarded in the simulation due to the lack of information about its geometry [37], and due to the limited effect of its wake, which affects only the downwind production [29, 113, 116]. This approximation moreover helps to reduce the computational complexity.

The simulation domain is rectangular with an allowance axial and vertical distances respectively of 10 D and 1.5 D. This shape is selected to reproduce a virtual wind tunnel with neglectable blockage effects: the adopted distances, largely greater than 10 times the chord length, were chosen to minimize the influence of the boundary walls. The domain is divided into two sub-domains, *gallery* and *cylinder*, to define different spatial discretizations and the rotor motion in the *cylinder* domain. The two domains are shown in Figure 2.31, where the size and the boundary conditions are also indicated. The validation case with the 2-meter rotor presents a perfect symmetry between the top and the bottom rotor halves, since a uniform wind speed is imposed at the velocity-inlet. Thus only half of the rotor is simulated, placing a symmetry boundary condition at the rotor equatorial plane. A *velocity inlet* boundary is imposed at the inlet, considering a uniform wind speed. The outlet is

considered as a *pressure outlet*, with a gauge pressure of 0 Pa. Since the simulation aims to reproduce the wind tunnel tests, a low level of turbulence is set both at the inlet and the outlet: the turbulence intensity was 0.1% and the turbulent viscosity ratio was 10, as suggested by the software User Guide [69]. The blades are considered as *no-slip walls*. Since additional details are not provided by the reference paper from Sheldahl [37], walls are considered smooth with a roughness height of 0 m.

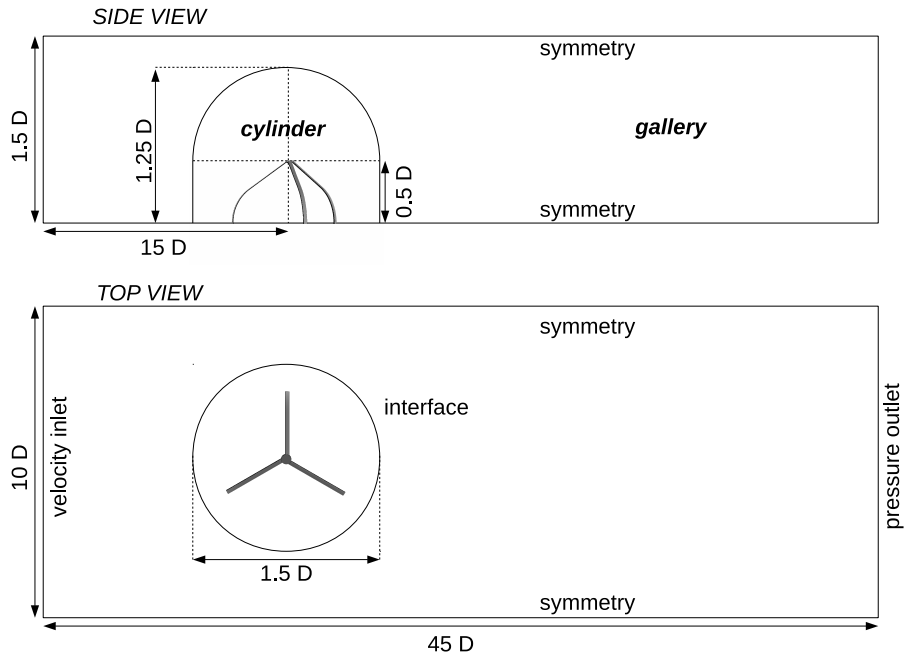

Figure 2.31: Scheme of the computational domains with boundary conditions and sizes.

2.4.1 Experimental Data

The experimental data provided by Sheldahl [37] of a 2-meter wind turbine are considered in the validation of the URANS-based simulations. The rotor is 2-meter high with a maximum radius of 0.98 m. The blade shape is straight-circular-straight (SCS): this is considered a good approximation of the Troposkien architecture [20] but it is cheaper to manufacture. The physical characteristics of the wind turbine are reported in Table 2.11, while a picture of the wind turbine installation at the Sandia test site is shown in Figure 2.32.

Open-field and wind tunnel tests were conducted considering two rotational speeds, 400 rpm and 460 rpm. The two tests provide results in good agreement with respect to the tip speed ratio. The comparison with the URANS-based simulations is therefore performed considering only the experimental data from the wind tunnel test at a rotational speed of 400 rpm. The

H [m]	2
R [m]	0.98
N_B [-]	3
Blade profile	NACA 0012
Blade shape	Straight-circular-straight (SCS)
c [mm]	58.77
σ [-]	0.18

Table 2.11: Main geometrical features of the baseline rotor configuration.

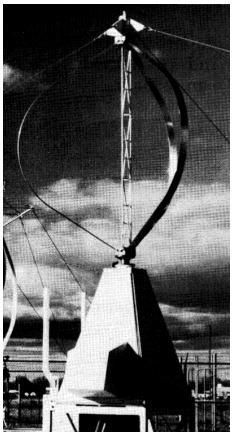

Figure 2.32: Sandia 2-meter Darrieus wind turbine installation (from: [37]).

technical report [120] indicates that the chord Reynolds number, defined as:

$$Re_c = \frac{\omega R c}{\nu} \tag{2.37}$$

was kept constant for this specific test at a value of $1.54 \cdot 10^5$.

The kinematic viscosity for the test can be evaluated and results to be $\nu = 1.566 \cdot 10^{-5}\ m^2/s$. This value is different from the common reference value at the standard sea level, which will be also adopted in the CFD simulation. In fact, considering an air density of $\rho = 1.225\ kg/m^3$ and a dynamic viscosity of $\mu = 1.789 \cdot 10^{-5}\ kg\ m/s$ [121], the kinematic viscosity at the standard sea level is $\nu = 1.460 \cdot 10^{-5}\ m^2/s$.

Retaining the original chord Reynolds number, a corrected rotational speed can be calculated from the standard kinematic viscosity, which results to be 371.09 rpm. The tip speed ratios are also corrected and a shifted performance curve is obtained, which is reported in Figure 2.33. This curve, which represents the rotor efficiency at the standard sea level, is considered in the following CFD validation.

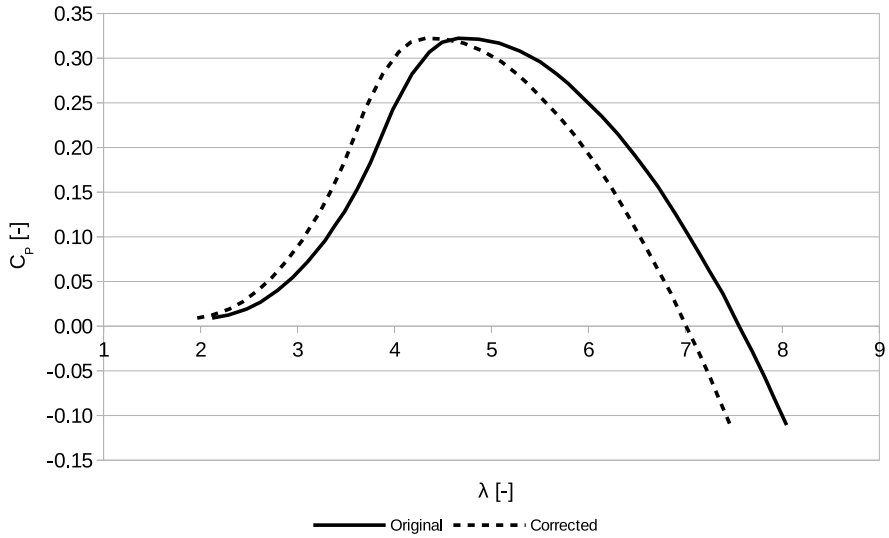

Figure 2.33: Original and kinematic viscosity corrected performance of the Sandia 2-meter rotor from the wind tunnel test.

2.4.2 Simulation Results

A sensitivity analysis is conducted to study the most important mesh parameters. A hexahedral mesh extrusion is created over the rotor blades, in order to simulate the blade's boundary layer. The first element height is estimated by imposing the maximum y^+ value in all the rotor near-wall cells to be lower than 1, an approximated value which is reported to maximize the reliability of the turbulence model [112]. The number of mesh extrusion steps and the growth rate were object of investigation, since these parameters strongly influence the total number of discretized elements, while other parameters are kept constant as reported in Table 2.12.

Number of elements on the blade airfoil	244
Number of elements on the blade lenght	300
Leading edge spacing [mm]	0.15
Trailing edge spacing [mm]	0.20
First layer height [mm]	0.011
Cylinder wall mean element size [mm]	85
Gallery wall mean element size [mm]	350
Volume mesh growth rate	1.15

Table 2.12: Geometrical parameters of the baseline mesh.

Two different configurations for the boundary layer extrusions were considered:

(i) 27 steps with a growth rate of 1.15;

(ii) 15 steps, 10 layers with a growth rate of 1.15 and 5 layers with a growth rate of 1.5.

Simulations are conducted considering tip speed ratios between 2 and 6 and the results are reported in Figure 2.34. The peak power coefficients and their tip speed ratios obtained with both mesh configurations are close to the experimental data. A good agreement is also registered with both mesh configurations at high tip speed ratios, whereas for low tip speed ratios the mesh with 15 steps is overpredicting the performance. The difference is, however, very limited.

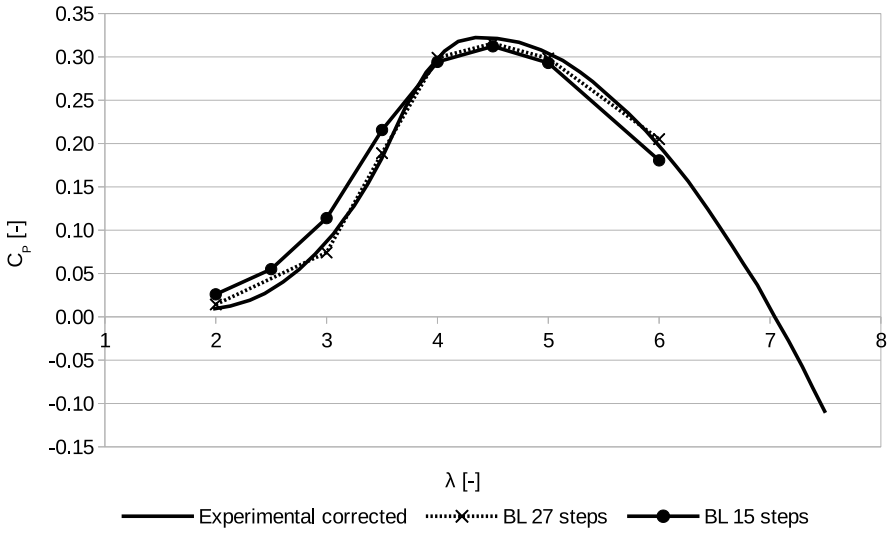

Figure 2.34: Simulation results with two different configurations for the boundary layer extrusion.

Moreover, the mesh with 15 steps is capable to capture completely the boundary layer when the airfoil is not stalling. The turbulent viscosity ratio experiences, in fact, a large rise and dissipation confined in the prism layer, as can be seen in Figures 2.35(a) and 2.35(b) for two azimuthal positions. This is not observed in Figure 2.35(c) for a different azimuthal position, since the airfoil stalls and the boundary layer is detached.

On the other hand, the simulation of a tilted Darrieus turbine requires two times the number of discretized elements, since the the blade airfoils from the upper and lower rotor halves would interact with the fluid at different angles of attack and therefore the symmetry hypothesis would not be anymore valid. The number of elements required for the configuration with 27 step extrusion is not compatible with the available computational power, since it exceeds the 64 GB RAM requirements. Therefore the configuration with 15 step extrusion is selected, as shown in Figure 2.36.

A sensitivity analysis is also conducted with respect to the number of elements on the base airfoils of the blade on a single operative condition, $\lambda = 4$. The simulation results are reported in Table 2.13. The CFD simulation with the higher number of elements is closer to the experimental result. On the other hand, a small difference is registered in the power

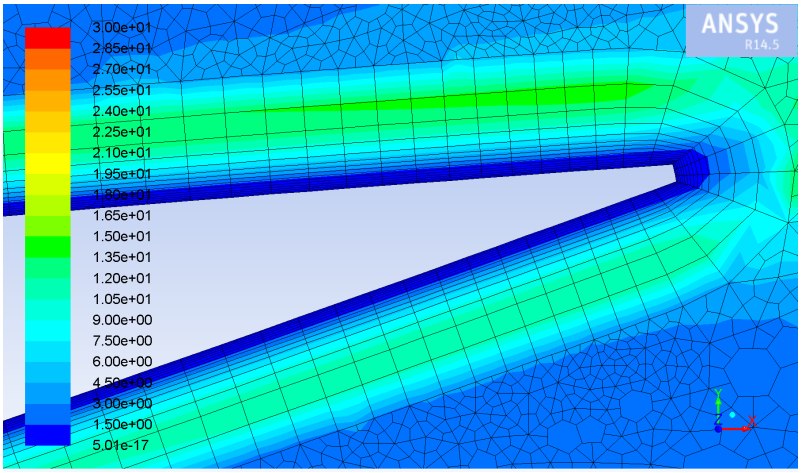

(a) $\theta = 12^\circ$

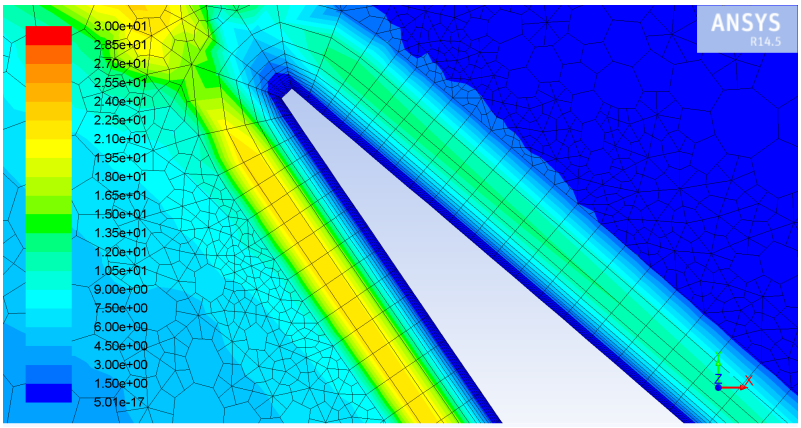

(b) $\theta = 132^\circ$

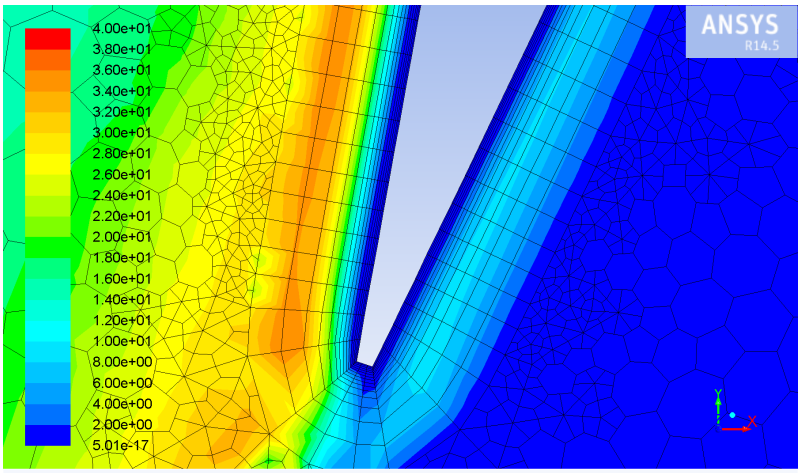

(c) $\theta = 252^\circ$

Figure 2.35: Turbulent viscosity ratio near the airfoil at different azimuthal positions, $\lambda = 4.5$.

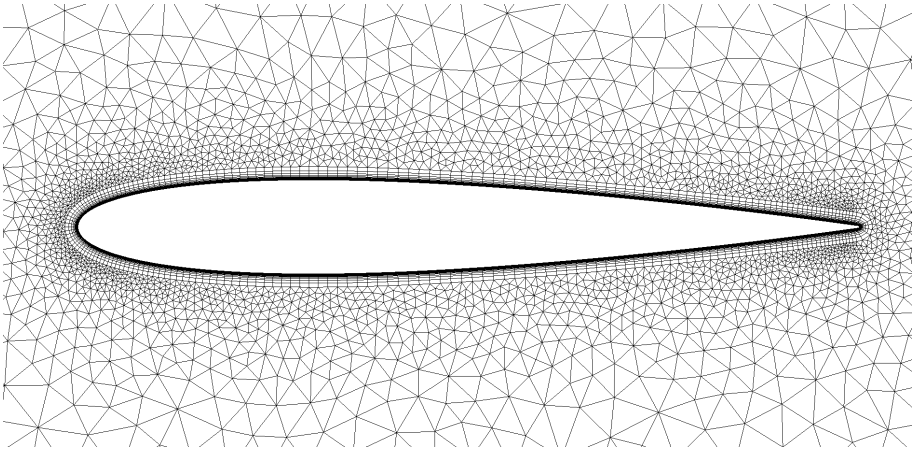

Figure 2.36: Airfoil mesh with 15 step boundary layer extrusion.

coefficient values estimated by CFD simulations and, due to the limitation in the RAM usage, the configuration with 244 elements on the profile is adopted.

Configuration	**Power Coefficient [-]**
Experimental corrected	0.300
CFD, 244 elements on profile	0.294
CFD, 364 elements on profile	0.304

Table 2.13: Simulation results for $\lambda = 4$ with two number of elements on the profile of the blade airfoil.

The mesh is characterized by 13.8 millions of cells and the unsteady simulation requires about 60 GB of RAM memory. A computer equipped with an 8-core Intel Xeon E5-2650 2.00 GHz takes about 10 min to complete a single time-step, whereas the final torque value is obtained after the simulation of 2500 time-steps on average.

2.4.3 Conclusions

An URANS approach based on the $k - \omega$ SST turbulence model was developed to predict the unsteady aerodynamics of the Darrieus rotor. A sensitivity analysis was conducted to determine the proper value of the most important parameters of the finite-volume domain discretization. Acceptable agreement between the experimental and the numerical results in non-tilted conditions was found, enabling the use of the model for the analysis of different configurations.

Chapter 3

Structural Simulation

The structural analysis of VAWTs is generally conducted by adopting a Finite Element Analysis (FEA) based on beam models, as presented in the Introduction. In this chapter, a steady model based on the Euler-Bernoulli beam theory is presented and validated (Section 3.1). The particular properties of the blade sections need to be estimated for any airfoil section and this methodology is provided in Section 3.2.

3.1 Beam Model

Berg [80] and Ashwill [81] reported the results from the experimental tests conducted on the Sandia 34m Darrieus wind turbine. The structural results are limited to the blade flatwise stress under gravitational and inertial loads for two rotational speeds. These results are compared with a FEA model developed by Sandia ("Sandia Model"). This FEA model involves beam elements [81] to perform the blade modelization. Each blade section is modeled with a different number of elements, which is shown in Figure 3.1. Each element matrix is calculated with the particular properties of the blade section or joint, considering the real weight measured from the rotor prototype. The blades' attachments to the central shaft are instead modeled considering two series of two beam elements per blade (the so called "mini-struts"). These structures increase the complexity of the structural model and lead to a lack in code reliability during the optimization process.

As a first step to validate the mass and properties calculated for the generic airfoil section as described in Section 3.2, a beam model is created using the commercial software Ansys APDL

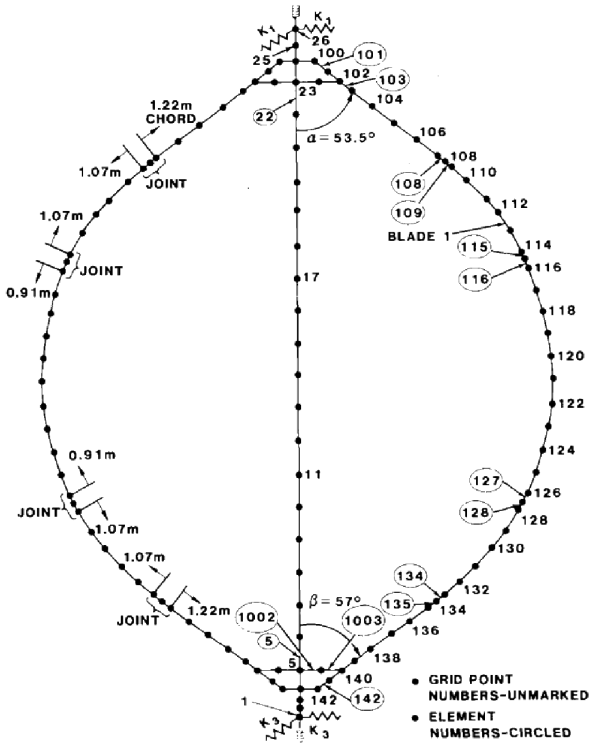

Figure 3.1: Finite element mesh adopted by Sandia to estimate the stress in the 42-meter rotor ([81]).

14.5. Each blade is modeled with a total of 160 elements whereas each "mini-strut" with 1 element, BEAM189 3-D Quadratic Finite Strain Beam [122]. The comparison between the experimental data, the numerical predictions provided by Sandia and Ansys 14.5 considering the gravitational load and the inertial load for two rotational speeds (without wind) are reported in Figure 3.2.

A good agreement between the numerical predictions provided by Sandia Model and Ansys 14.5 is registered over the whole blade range, showing a similar accuracy with respect to the experimental data. A slight difference in the stress peak is nevertheless registered when the rotational speed is 28 rpm. On the other hand, the Sandia Model adopts the real mass and property for every blade section, which are referred to be measured from the full scale rotor but are not provided in the reference paper: differences from the theoretical values, which can lead to discrepancies in numerical stresses, are therefore expected.

A model based on the Euler-Bernoulli beam theory [86] is created ("Structural Model") and its results compared against the validated Ansys model. The "mini-struts" are not implemented in the Structural Model and these are therefore removed from the validated Ansys model. The simulation conducted with the gravitational and inertial loads for two rotational speeds is again performed and the results are reported in Figure 3.3. The same experimental data are again reported as a general reference, even if the "mini-struts" are still present in the

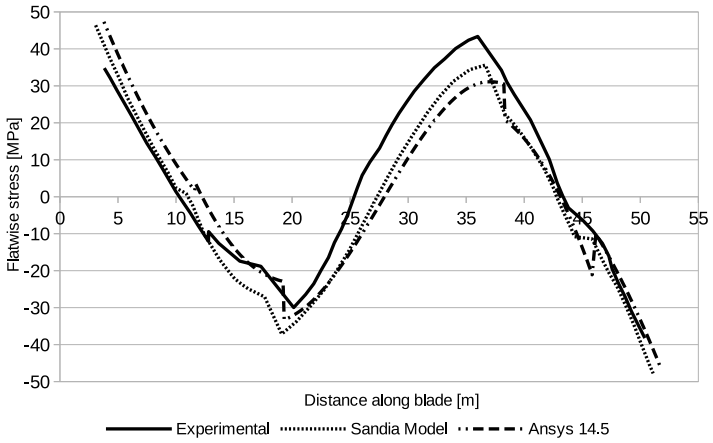

(a) Gravity

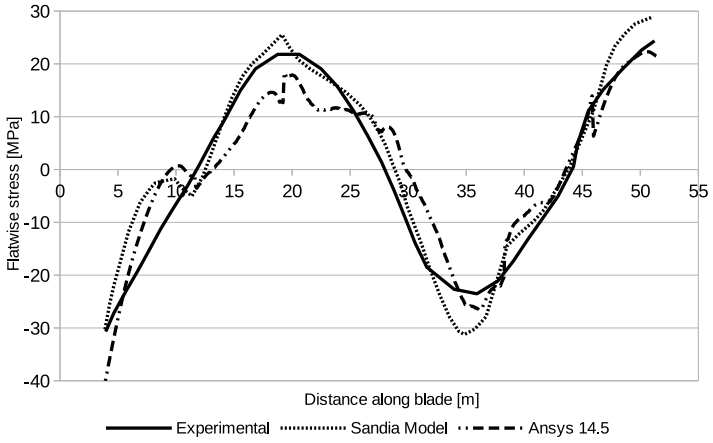

(b) 28 rpm

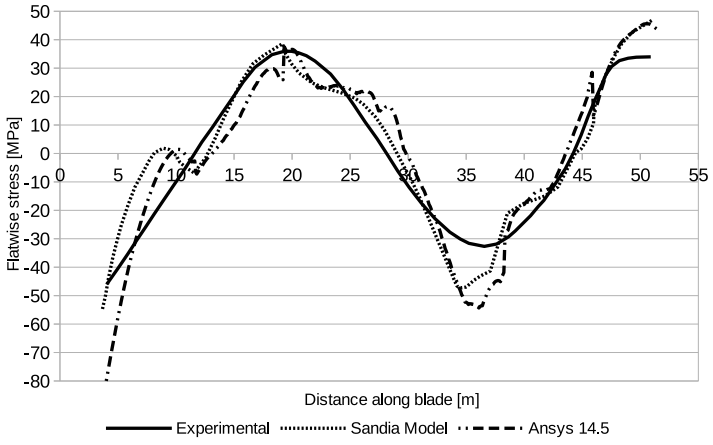

(c) 40 rpm

Figure 3.2: Comparison between the experimental data, the numerical predictions provided by Sandia and Ansys 14.5 considering the gravitational load and the inertial load for two rotational speeds.

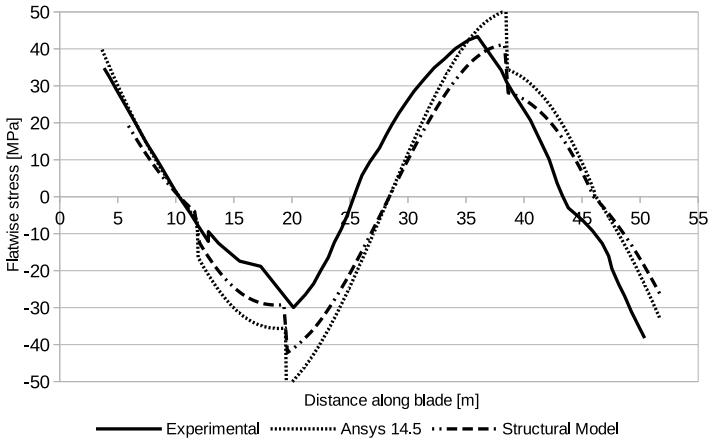

(a) Gravity

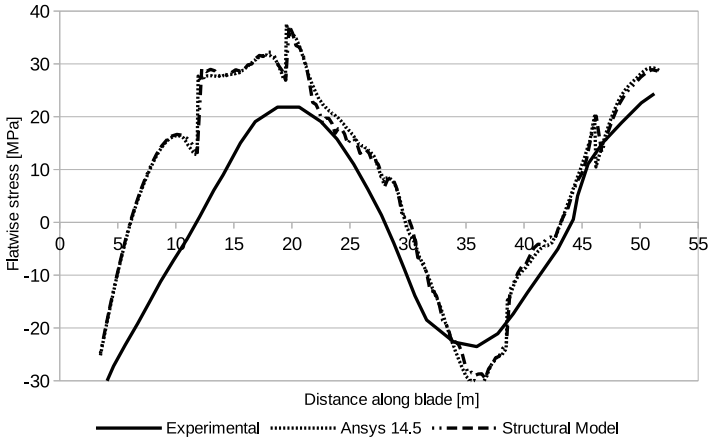

(b) 28 rpm

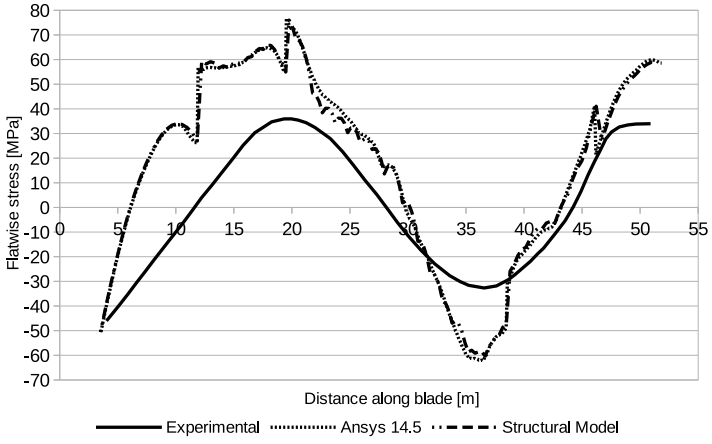

(c) 40 rpm

Figure 3.3: Comparison between the experimental data and the numerical predictions without "mini-struts" provided by Ansys 14.5 and the Structural Model considering the gravitational load and the inertial load for two rotational speeds.

experimental rotor.

A very good agreement between the Structural Model and Ansys 14.5 predictions is registered for the two rotational speeds, whereas a difference is evidenced in the proximity of the blade segment joints in the gravitational simulation. This particular difference can be again related to peculiar devices introduced in the blade: the joints, which are used to couple different blade segments, are not widely documented in the reference and are modeled as concentrated mass in both numerical models. Moreover, Ansys 14.5 adopts a different beam model compared to the one adopted in the Structural Model, leading to differences in the final flatwise stress. However, since the simulation will be conducted with a spinning rotor and given the very good agreement between the two numerical codes, the Structural Model is considered as validated.

3.2 Section Properties

The airfoil shape is not generally included in the section database of commercial software and therefore section properties need to be supplied.

The NACA profile shape is obtained considering the following function:

$$y = \frac{t/c}{0.2}\left(0.2969x^{0.5} - 0.1260x - 0.3516x^2 + 0.2843x^3 - 0.1036x^4\right) \tag{3.1}$$

In order to have a higher point concentration on the leading and trailing edge, a cosine distribution for the x values is adopted. The wall thickness is introduced as normal distance from the airfoil profile. The normal direction is estimated by calculating the orthogonal direction to the profile shape derivative:

$$\frac{dy}{dx} = \frac{t/c}{0.2}\left(0.2969 \cdot 0.5x^{-0.5} - 0.1260 - 0.3516 \cdot 2x + 0.2843 \cdot 3x^2 - 0.1036 \cdot 4x^3\right) \tag{3.2}$$

The possibility to introduce spars is also considered. The chord position as well as the thickness needs to be provided for each spar. An example of the considered geometry is reported in Figure 3.4.

The methodologies adopted to estimate the airfoil properties are reported below.

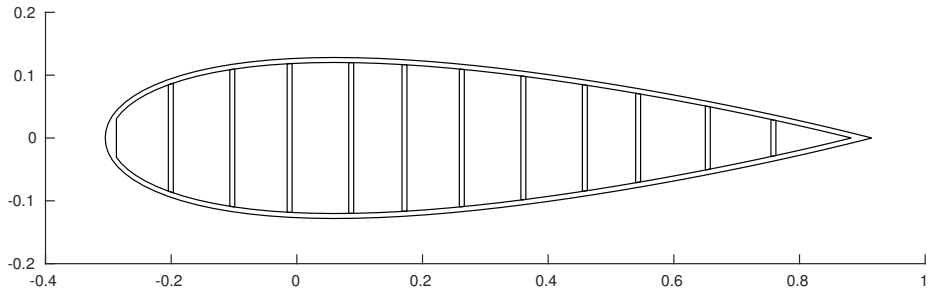

Figure 3.4: Example geometry for the estimation of section properties: NACA 0021 with 11 spars.

3.2.1 Moments of Inertia

The moments of inertia of a polygon described by n_P counter-clockwise points can be estimated by the following formulas:

$$I_x = \sum_{i=1}^{n_P} (x_i \cdot y_{i+1} - x_{i+1} \cdot y_i) \frac{y_i^2 + y_i \cdot y_{i+1} + y_{i+1}^2}{12} \tag{3.3}$$

$$I_y = \sum_{i=1}^{n_P} (x_i \cdot y_{i+1} - x_{i+1} \cdot y_i) \frac{x_i^2 + x_i \cdot x_{i+1} + x_{i+1}^2}{12} \tag{3.4}$$

$$I_{xy} = \sum_{i=1}^{n_P} (x_i \cdot y_{i+1} - x_{i+1} \cdot y_i) \frac{x_i \cdot y_{i+1} + 2x_i \cdot y_i + 2x_{i+1} \cdot y_{i+1} + x_{i+1} \cdot y_i}{24} \tag{3.5}$$

considering $x_{n_P+1} = x_1$ and $y_{n_P+1} = y_1$. The section moments of inertia are calculated by summing up the outer shell and spar moments and subtracting the inner shell moment.

3.2.2 Centroid

The centroid coordinates of a polygon described by n_P points can be estimated by means of:

$$x_c = \frac{1}{6A_C} \sum_{i=1}^{n_P} (x_i + x_{i+1})(x_i \, y_{i+1} - x_{i+1} \, y_i) \tag{3.6}$$

$$y_c \;=\; \frac{1}{6A_C}\sum_{i=1}^{n_P}(y_i + y_{i+1})(x_i\; y_{i+1} - x_{i+1}\; y_i) \tag{3.7}$$

where A_C is the polygon area and considering $x_{n_P+1} \;=\; x_1$ and $y_{n_P+1} \;=\; y_1$. The section centroid is obtained by area-averaging the outer, inner and spar centroids.

3.2.3 Shear Center

The shear center is calculated by considering the thin shell stress analysis, as described by Kuhn [123]. The shear center is located on the symmetry axis. A unitary shear force at a undetermined distance is applied and entirely sustained by the spars. By imposing every cell rotation to be equal to zero and applying a force balance, the distance where the force needs to be applied in order not to have rotation, i.e. the shear center, is found. An example of multicellular shell with reference to the geometrical details is shown in Figure 3.5. The internal and external forces introduced in order to find the shear center are shown in Figure 3.6.

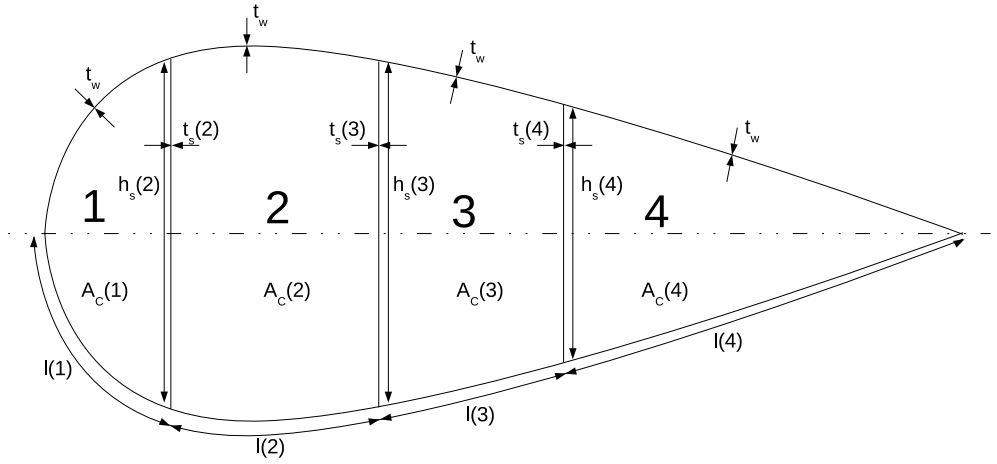

Figure 3.5: Multicellular shell, with reference to geometrical details.

The distribution of the external shear load on every spar can be found considering:

$$S(i) \;=\; P_u\frac{I(i)}{I_S} \tag{3.8}$$

$$s(i) \;=\; \frac{S_i}{h_s(i)} \tag{3.9}$$

where $I(i)$ is the i^{th} spar inertia and I_S is their sum. This shear stresses need to be added to the $q(i)$ stresses generated by the torque.

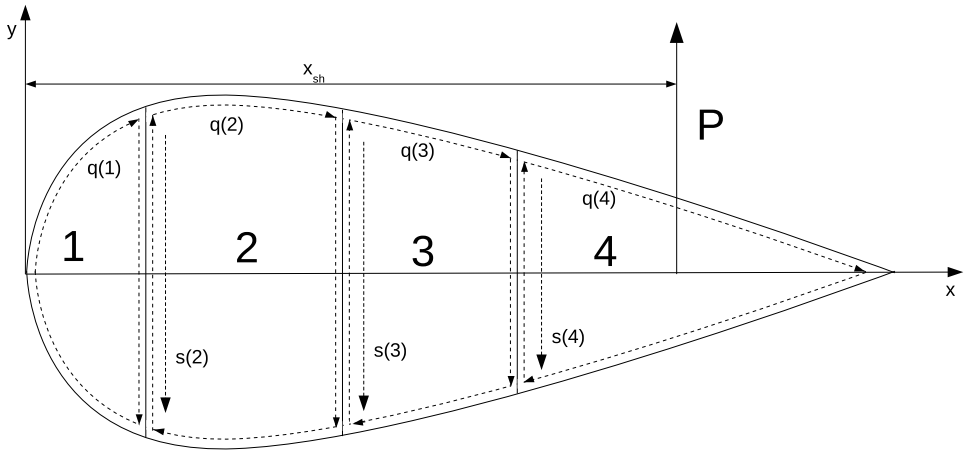

Figure 3.6: Internal and external forces introduced in order to find the shear center.

The rotation angle for the i^{th} section can be therefore expressed as:

$$\theta_i = \frac{1}{2G_S A_C(i)} \oint \frac{q_i}{t_i} ds \tag{3.10}$$

$$= \frac{1}{2G_S A_C(i)} \left(2\frac{q_i}{t_w} l(i) + \frac{q(i) - q(i-1) - s(i)}{t_s(i)} h_s(i) + \frac{q(i) - q(i+1) + s(i+1)}{t_s(i+1)} h_s(i+1) \right) \tag{3.11}$$

where $A_C(i)$ is the cell area and G_S is the shear modulus.

By imposing every rotation equal to zero, a linear system of n_P variables and n_P equations is obtained. For the example shown in Figure 3.5, the linear system becomes:

$$\begin{bmatrix} \frac{2l(1)}{t_w} + \frac{h_s(2)}{t_s(2)} & -\frac{h_s(2)}{t_s(2)} & 0 & 0 \\ -\frac{h_s(2)}{t_s(2)} & \frac{2l(2)}{t_w} + \frac{h_s(2)}{t_s(2)} + \frac{h_s(3)}{t_s(3)} & -\frac{h_s(3)}{t_s(3)} & 0 \\ 0 & -\frac{h_s(3)}{t_s(3)} & \frac{2l(3)}{t_w} + \frac{h_s(3)}{t_s(3)} + \frac{h_s(4)}{t_s(4)} & -\frac{h_s(4)}{t_s(4)} \\ 0 & 0 & -\frac{h_s(4)}{t_s(4)} & \frac{2l(4)}{t_w} + \frac{h_s(4)}{t_s(4)} \end{bmatrix} \times \begin{bmatrix} q(1) \\ q(2) \\ q(3) \\ q(4) \end{bmatrix} = \begin{bmatrix} -s(2)\frac{h_s(2)}{t_s(2)} \\ s(2)\frac{h_s(2)}{t_s(2)} - s(3)\frac{h_s(3)}{t_s(3)} \\ s(3)\frac{h_s(3)}{t_s(3)} - s(4)\frac{h_s(4)}{t_s(4)} \\ s(4)\frac{h_s(4)}{t_s(4)} \end{bmatrix} \tag{3.12}$$

The shear loads generated by the torque are therefore calculated and the shear center coordinate x_{sh} can be estimated considering the position where a unitary load can be applied

without inducing a rotation of the section:

$$P_u x_{sh} \;=\; \sum S(i)x_s(i) + 2\sum q(i)A_C(i) \tag{3.13}$$

where P_u is the unitary load and x_s the spar positions.

3.2.4 Torsional Constant

The torsional constant J represents the ability of the beam to resist torsion. As described by Kuhn [123], in a multicellular shell this can estimated considering the shear loads obtained by imposing every cell rotation to be the same. Moreover, the sum of each cell torque must be equal to the total torque. The coefficient matrix in Equation 3.12 is considered, subtracting every line to the previous one: these coefficient represent the subtraction between the angles of two adjacent cells. The resulting system of equations for the example in Figure 3.5 would therefore be:

$$\begin{bmatrix} \frac{2l(1)}{t_w} + \frac{h_s(2)}{t_s(2)} + \frac{h_s(2)}{t_s(2)} & -\frac{h_s(2)}{t_s(2)} - \frac{2l(2)}{t_w} - \frac{h_s(2)}{t_s(2)} - \frac{h_s(3)}{t_s(3)} & \frac{h_s(3)}{t_s(3)} & 0 \\ -\frac{h_s(2)}{t_s(2)} & \frac{2l(2)}{t_w} + \frac{h_s(2)}{t_s(2)} + \frac{h_s(3)}{t_s(3)} + \frac{h_s(3)}{t_s(3)} & -\frac{h_s(3)}{t_s(3)} - \frac{2l(3)}{t_w} - \frac{h_s(3)}{t_s(3)} - \frac{h_s(4)}{t_s(4)} & \frac{h_s(4)}{t_s(4)} \\ 0 & -\frac{h_s(3)}{t_s(3)} & \frac{2l(3)}{t_w} + \frac{h_s(3)}{t_s(3)} + \frac{h_s(4)}{t_s(4)} + \frac{h_s(4)}{t_s(4)} & -\frac{h_s(4)}{t_s(4)} - \frac{2l(4)}{t_w} - \frac{h_s(4)}{t_s(4)} \\ 2A_C(1) & 2A_C(2) & 2A_C(3) & 2A_C(4) \end{bmatrix} \times \begin{bmatrix} q(1) \\ q(2) \\ q(3) \\ q(4) \end{bmatrix} = \begin{bmatrix} 0 \\ 0 \\ 0 \\ T_u \end{bmatrix} \tag{3.14}$$

where T_u is the unitary torque.

The torsional constant can be therefore estimated by considering the general expression applied to any cell, in this case to the first:

$$J \;=\; \frac{T_u}{G_S \theta_S} \;=\; \frac{T_u}{\frac{1}{2A_C(1)}\left(2q(1)\frac{l(1)}{t_w} + (q(1) - q(2))\,\frac{h_s(2)}{t_s(2)}\right)} \tag{3.15}$$

Chapter 4

Applications

This chapter presents several applications of the aerodynamic and structural models presented in the previous chapters to analyse and optimize the performance of different configurations of VAWTs. Section 4.1 present an aerodynamic analysis and optimization for the DeepWind geometry. Section 4.2 provides an insight on the aerodynamic performance of a floating VAWT under tilt conditions. Section 4.3 shows the results for an aerodynamic optimization of the airfoil to be maximize the aerodynamic production of a Darrieus rotor. Finally, Section 4.4 reports the results of an aero-structural optimization with focus on the aerodynamic performance and structural stress.

4.1 DeepWind

Seventh Framework Programme (FP7) DeepWind is the first project aiming to design a big-scale offshore floating vertical axis wind turbine with a nominal power generation of 5 MW [17, 124, 125]. Given the considerable rotor size needed to achieve this power production, the Troposkien shape is chosen in order to reduce the blade stresses. The rotor shape was further analysed and optimized from the baseline to account for the gravity effect, leading to a new blade geometry designed for the target operative conditions [18]. Estimations of the rotor loads obtained with the aeroelastic code HAWC2 are provided in the final report from DTU Wind Energy [126] The purpose of this work is to conduct an aerodynamic improvement with different blade configurations, considering different numbers of blades, profiles and chord distributions.

4.1.1 Baseline Rotor

The rotor shape was designed considering a maximum allowable strain [18] and is kept constant in the aerodynamic optimization. The blade shape is shown in Figure 4.1.

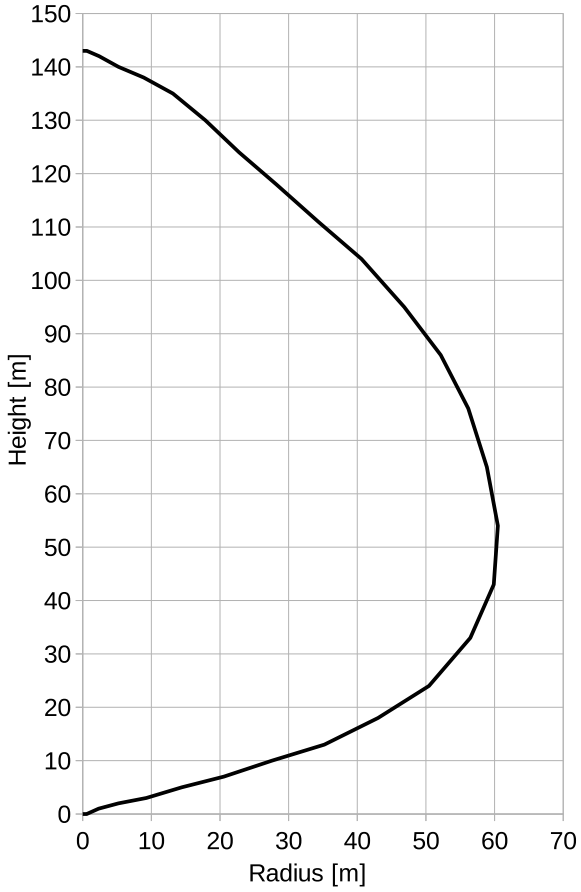

Figure 4.1: DeepWind optimized blade rotor shape.

The baseline rotor configuration, developed in the DeepWind project and characterized by the parameters reported in Table 4.1, is simulated using the BEM algorithm validated in the Section 2.1. A uniform wind speed ranging from 4 m/s to 25 m/s is considered. This assumption, which does not take into consideration the peculiar offshore environment where the turbine will operate, is introduced to perform a fair power comparison with the other aerodynamic simulations from the DeepWind project. A more careful simulation could be eventually conducted in the future considering simplified models for the wind over the water surface, e.g. increasing the ground roughness according to the Charnock's formula [127]. A rotational speed from 0 rpm to 6 rpm with steps of 0.2 rpm is considered: the power production at the different wind speeds is estimated considering the optimal tip speed ratio, until the maximum rotational speed is reached. The simulation results are shown in Figure 4.2(a).

Height	143 m
Radius	60.5 m
Airfoil	NACA 0018
Chord	5 m
Blade number	2
Solidity	0.165
Max. rotation speed	6 rpm

Table 4.1: Baseline parameters for the DeepWind project rotor.

The maximum power production of 4.5 MW is achieved for a wind speed approximately equal to 14 m/s, which will be referred as nominal wind speed. For higher rotational speeds, the rotor turns into stall and the performance is therefore reduced.

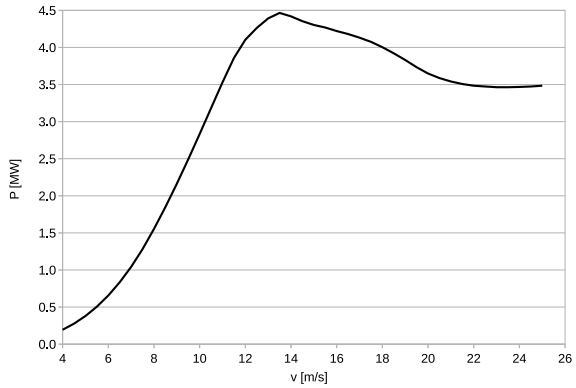

(a) Power production

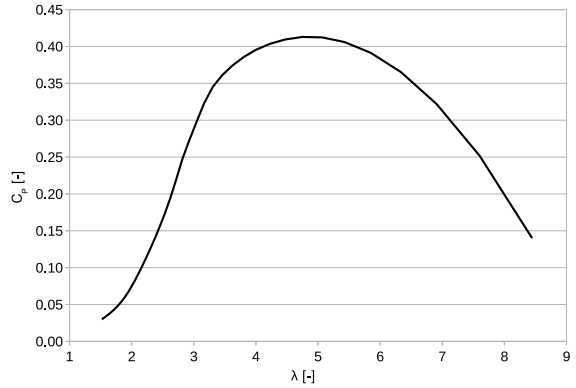

(b) Power coefficient

Figure 4.2: Performance for the DeepWind baseline configuration estimated with BEM algorithm.

The power coefficient C_P, defined as:

$$C_P = \frac{P}{0.5\rho A v^3} \tag{4.1}$$

where P is the power production, ρ is the air density and A is the swept area, is shown in Figure 4.2(b) against the tip speed ratio λ, defined as:

$$\lambda = \frac{\omega R}{v} \tag{4.2}$$

where ω is the rotational speed and R is the maximum rotor radius.

The rotor operates at the maximum efficiency for tip speed ratios higher than 4, corresponding to wind speeds lower than approximately 9 m/s. After this limit, the control system keeps the rotational speed constant at 6 rpm.

4.1.2 Aerodynamic Optimization

This section presents the results obtained from the analysis of different blade configurations in order to maximize the power production and minimize the blade loads and manufacturing cost. Two different campaigns are conducted:

1. variation of the number of blades keeping the solidity constant;
2. variation of the profile thickness.

Finally, an optimization of the chord distribution along the blade span is conducted.

4.1.2.1 Number of Blades

The number of blades is the object of the present investigation. In order to keep the comparison fair, the same solidity among the different configurations is considered by decreasing the chord size. The performance is expected not to be influenced by the blade number: in BEM computations, solidity is the key factor for the performance variation. The blade tangential and normal force coefficient [21], defined as:

$$C_t = C_L \sin\alpha - C_D \cos\alpha \tag{4.3}$$

$$C_n = C_L \cos\alpha + C_D \sin\alpha \tag{4.4}$$

being C_L and C_D respectively the airfoil lift and drag coefficient at the angle of attack α, are shown in Figure 4.3 for a wind speed of 10 m/s and do not depend on the blade number.

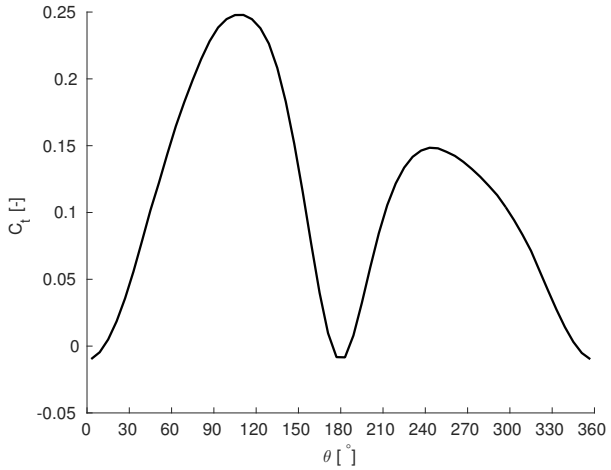

(a) Tangential force coefficient

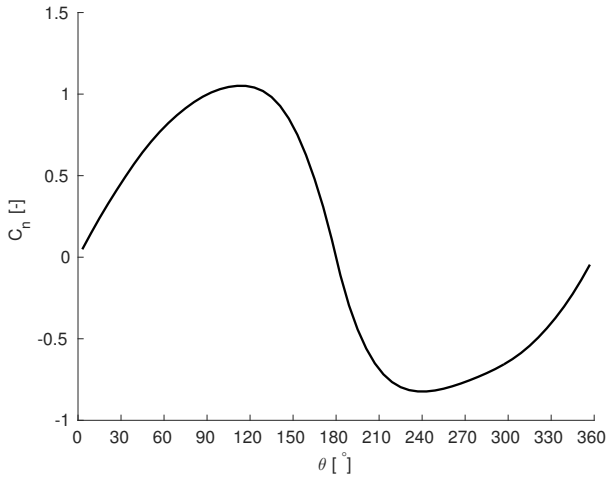

(b) Normal force coefficient

Figure 4.3: Single blade tangential and normal force coefficients computed by BEM algorithm.

The rotor loads are obtained by scaling, projecting and combining these coefficients in the parallel and orthogonal directions to the wind. The loads are separated in thrust C_T and side C_N force coefficients and represent a measure of the stress [36]. The coefficient values, shown in Figure 4.4, are sensibly different due to the different combination of forces acting simultaneously on the blades.

The rotor configuration characterized by the largest varying loads is the single-bladed: both the thrust and side force coefficients experience a large variation along the azimuthal positions. The two-bladed configuration is characterized by a higher thrust coefficient and a lower side force coefficient variations with respect to the three-bladed configuration. This is justified considering the axial-symmetry of the two-bladed configuration, whose side loads are more balanced than in the three-bladed configuration. Finally, the four-bladed configuration present

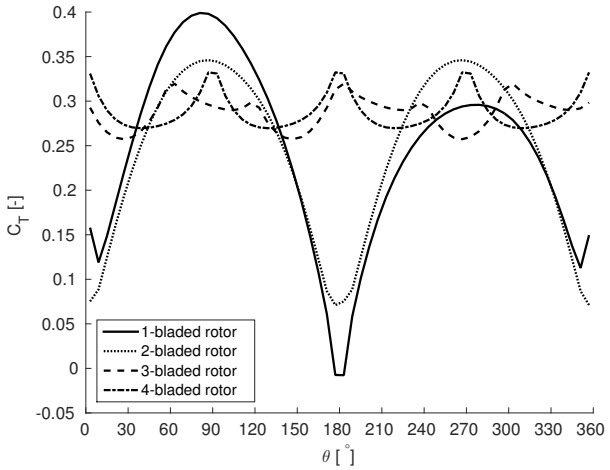

(a) Thrust force coefficient

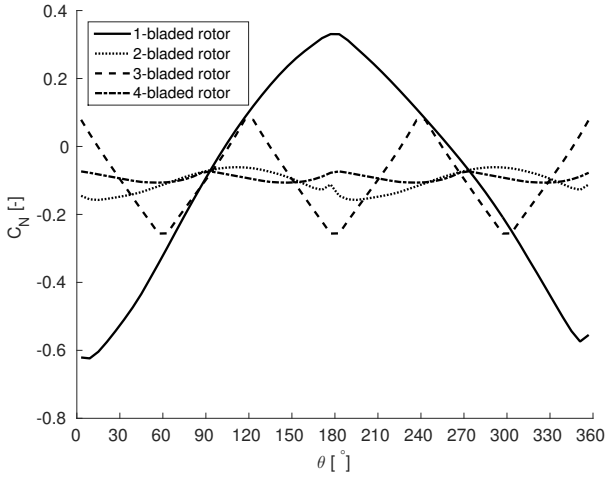

(b) Side force coefficient

Figure 4.4: Rotor thrust and side force coefficients with respect to the different number of blades.

the smallest variations. On the other hand, the higher the number of blades, the higher number of stress cycles the blade experiences. Even though the stress variation is lower, the increased number of cycles has a significant negative impact on the fatigue life [128]. This aspect should be carefully considered for the choice of the final design.

The power coefficients for the different blade-number configurations are shown in Figure 4.5, both for the single blade and for the whole rotor. This coefficient give a measure on the power production for the different azimuthal positions. As expected, the higher the number of blades, the more averaged the power generation and therefore the torque variation.

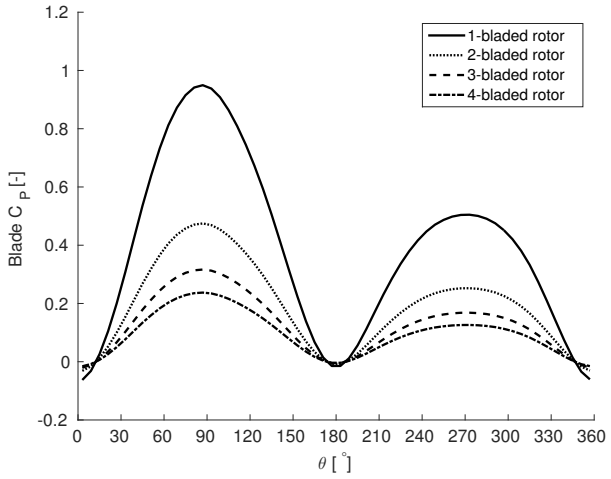

(a) Single blade

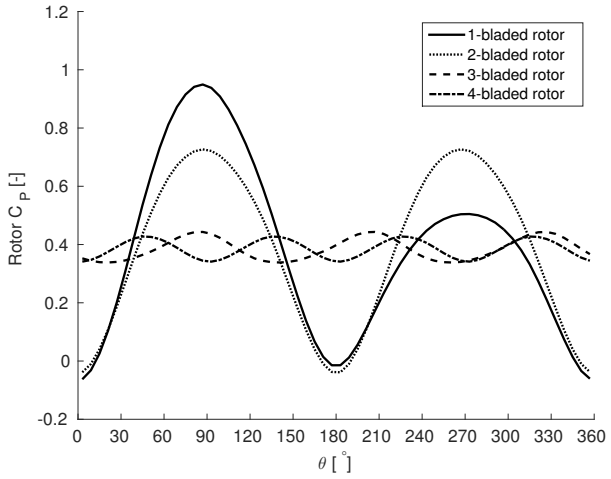

(b) Whole rotor

Figure 4.5: Single blade and whole rotor power coefficients with respect to the different number of blades.

4.1.2.2 Blade Airfoil

Different blade airfoils are tested with respect to the baseline configuration in order to find the most suitable combination. Only the aerodynamic perspective is considered as a first step, i.e. no minimum thickness is required to support the rotor load. The airfoils belong to the symmetric NACA family and their choice is limited by the availability of aerodynamic coefficients extended to $\pm 180°$. As previously stated, the database from Jacobs [43, 44] and Bullivant [45] are considered, being the first validated against experimental data and the second the only available for high Reynolds number. The databases are extended considering Sheldahl database [41] for angles of attack higher than 30°: these data are not experimentally measured but numerically estimated using the PROFILE code by Eppler [98].

The rotor simulations are conducted considering wind speeds ranging from 4 m/s to 25 m/s and rotational speeds from 0 rpm to 6 rpm. The power curves for the different blade configurations are shown in Figure 4.6. The highest power productions are achieved with NACA 0015 and NACA 0018 profiles, whereas for higher thickness profiles the performance is strongly reduced. These profiles provide, in fact, lower lift values, penalizing the production in the non-stalled region.

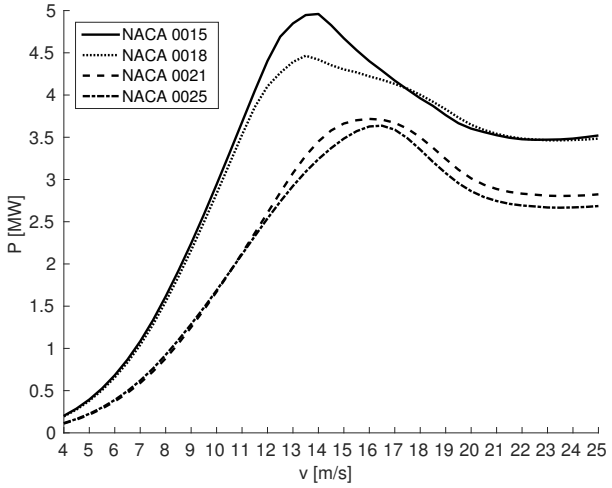

Figure 4.6: Power curves for the rotor equipped with different blade airfoils.

The loads are of strong interest for the rotor design. The tangential and normal thrust coefficients for the single blade are shown in Figure 4.7. The loads as well as the power production are reduced for blades with high thickness profiles: despite the increased profile drag, since the profile mostly operates at low angles of attack, the loads are however reduced. Finally, since the normal force coefficient does not present appreciable changes in the two-bladed configuration (see Figure 4.4(b)), the only thrust coefficient is shown in Figure 4.8 with respect to the azimuthal position. The thrust load is also decreased by increasing the profile thickness.

4.1.2.3 Chord Optimization

The rotor shape is designed to minimize the shear stress, leading to blades subjected only to normal loads. On one hand this shape reduces the swept area and therefore the efficiency with respect to a H-rotor with the same radius, but on the other hand the constraints on the material choice and blade airfoil are less severe since loads are smaller. The blade is therefore characterized by a variable radius and it is reasonable to assume that, since every blade section operates at different tip speed ratios, the optimal chord would vary along the blade span. In order to find the optimal distribution, the simulation algorithm is coupled with an optimization algorithm, a genetic code, as described by Bedon et al. [30–32]. The code

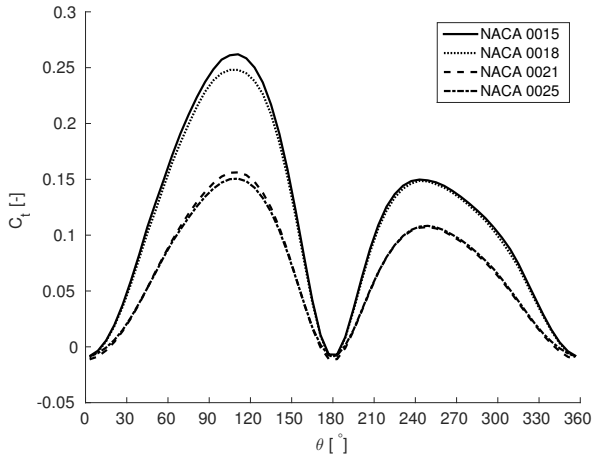

(a) Tangential force coefficient

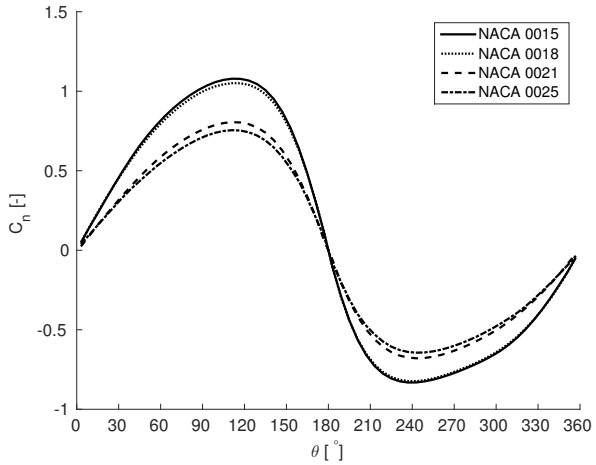

(b) Normal force coefficient

Figure 4.7: Single blade tangential and normal force coefficients for different airfoil configurations.

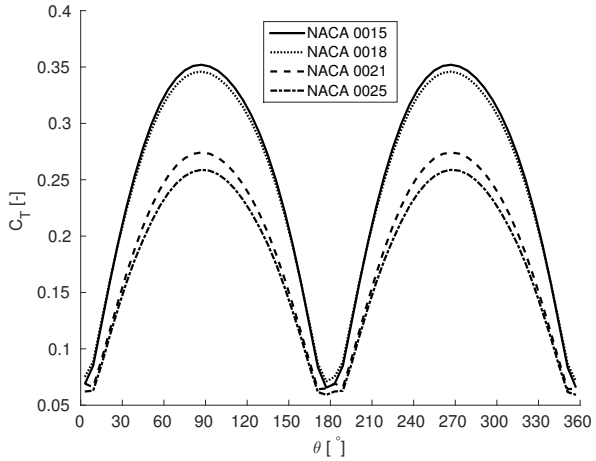

Figure 4.8: Rotor thrust force coefficients for different airfoil configurations.

coupling provides the optimization loop shown in Figure 4.9.

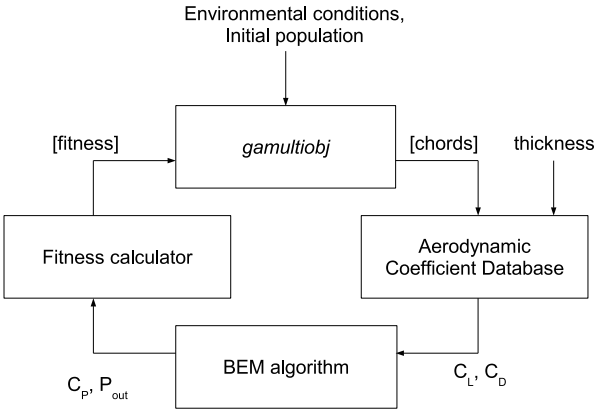

Figure 4.9: Optimization loop obtained by coupling the simulation and the optimization algorithm, from [31].

The optimization is conducted providing the genetic algorithm with 250 individuals evolved for 20 generations. The thickness is kept constant as well as the other rotor parameters, whereas the chord is varied between 1 m and 12 m, being a solidity of $\sigma = 0.4$ an upper limit for the BEM code validity [36]. The chord variation have been parametrized by 30 decisional parameters freely varied by the optimization algorithm. The optimization purpose is to maximize the energy production for a wind speed around the nominal value of 14 m/s.

The optimization algorithm may provide a result which does not present smooth parameter trends. This behavior is usually related to the intrinsic mechanism of the genetic algorithm, which considers a fitness value to perform a wise parameter variation and converge to the optimal result. A not complete convergence to the optimal solution and/or a limited fitness function sensitiveness to small variations of the optimization parameters can therefore prevent the free optimization to provide a smooth trend [129]. In this case, a combination of both the factors led to an unstable trend of the chord distribution. A smooth trade-off solution is therefore obtained by curve-fitting the results. This solution is named "Trade-off configuration" and compared to the baseline solution. The baseline configuration, the free optimization result and the Optimization Trade-Off chord distributions are shown in Figure 4.10.

The optimization provides a result with a chord distribution sensibly increased with respect to the baseline solution. The power production and power coefficient curves for the optimized trade-off are obtained by BEM code simulation and reported against the baseline curves in Figure 4.11.

The power production is sensibly increased up to a nominal power production of 7.5 MW whereas the maximum power coefficient is increased up to 0.45. The optimal aerodynamic configuration needs however to be analysed also from the structural perspective, analysing

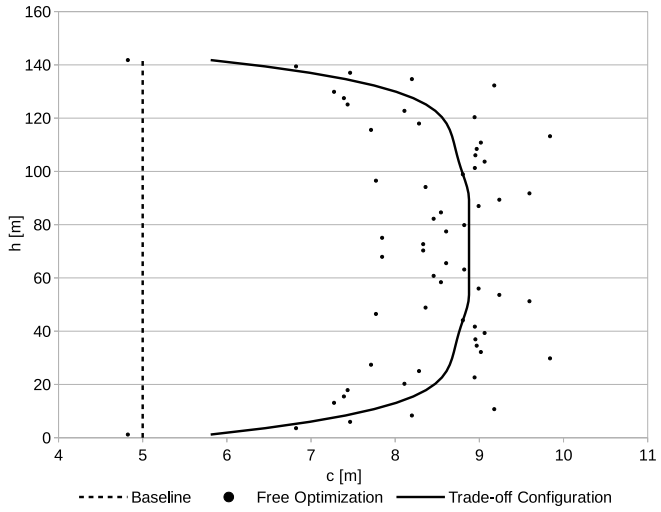

Figure 4.10: Chord distributions of the baseline, free optimization and the trade-off configurations.

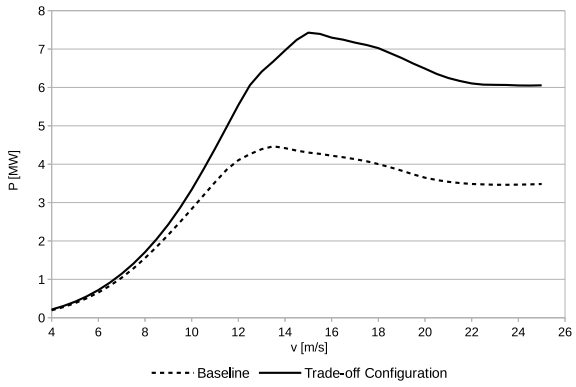

(a) Power curve

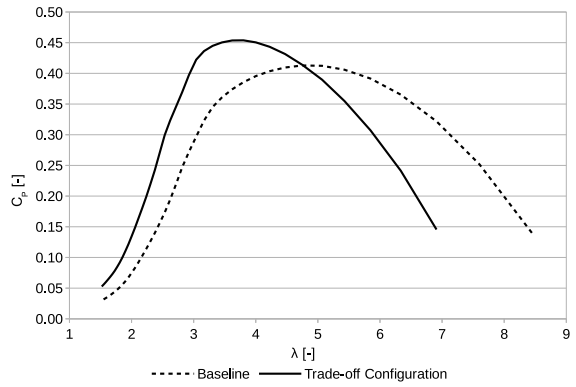

(b) Power coefficient curve

Figure 4.11: Performance for the baseline and optimized trade-off configurations.

the increased loads. In fact, even if the normal force coefficient does not sensibly vary, the thrust coefficient experiences an increase from the baseline to the trade-off configurations, as shown in Figure 4.12. An increase of 38% is experienced and this may seriously change the design for the auxiliary components or even violate the constraints.

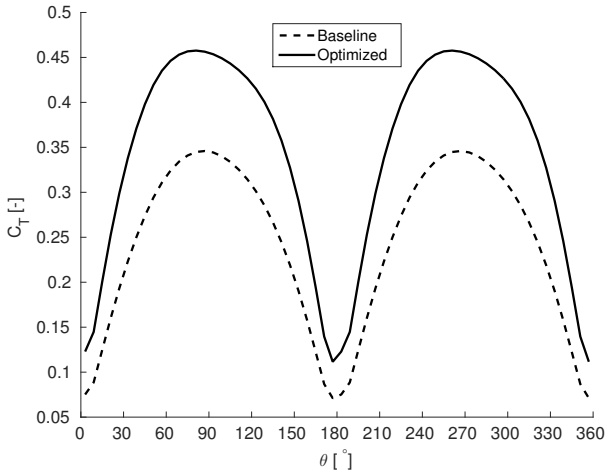

Figure 4.12: Rotor thrust and side force coefficients for baseline and optimized trade-off configurations.

4.1.2.4 Summary of Results

The results obtained from the different cases are reported in this section along with the percentage variation from the baseline. The mean thrust and side load coefficients and their cycle amplitude, useful to establish the fatigue life, are reported in Table 4.2. An opposite trend between thrust and normal mean coefficients is highlighted by increasing the blade number: the choice should be therefore conducted by considering the overall system dynamics. Differently, a reduction of both mean coefficients and cycle amplitude is obtained by increasing the airfoil thickness. The Optimization Trade-Off, due to the increased power performance, finally presents sensibly increased load coefficients.

The performance comparison is reported in Table 4.3. The performance variation due to the different number of blades is not appreciable with BEM algorithm. A strong power reduction is instead observed by increasing the airfoil thickness, since airfoil efficiency (defined as ratio between lift and drag coefficients) is decreased. Finally, the Optimization Trade-Off, as expected from the optimization routine, provides a power production and power coefficient sensibly increased from the baseline configuration.

	$C_{T,mean}$ [-]		ΔC_T [-]		$C_{N,mean}$ [-]		ΔC_N [-]	
Baseline	0.2429		0.2749		-0.1051		0.0963	
1-bladed rotor	0.2429	0.0%	0.4066	47.9%	-0.1051	0.0%	0.9544	891.1%
2-bladed rotor	0.2429	0.0%	0.2749	0.0%	-0.1051	0.0%	0.0963	0.0%
3-bladed rotor	0.2876	18.4%	0.0623	-77.3%	-0.0939	-10.7%	0.3348	247.7%
4-bladed rotor	0.2891	19.0%	0.0627	-77.2%	-0.0931	-11.4%	0.0330	-65.7%
NACA 0015	0.2457	1.2%	0.2864	4.2%	-0.1061	1.0%	0.0922	-4.3%
NACA 0018	0.2429	0.0%	0.2748	0.0%	-0.1051	0.0%	0.0963	0.0%
NACA 0021	0.1876	-22.8%	0.2100	-23.6%	-0.0657	-37.5%	0.0547	-43.2%
NACA 0025	0.1773	-27.0%	0.1996	-27.4%	-0.0704	-33.0%	0.0706	-26.7%
Optimized Trade-Off	0.3441	41.7%	0.3460	25.9%	-0.1419	35.0%	0.2265	135.2%

Table 4.2: Thrust and side force mean coefficients, cycle amplitude and percentage variation from the baseline configuration for the different analysed configurations.

	P_{max} [MW]		$C_{P,max}$ [-]	
Baseline	4.4652		0.4133	
NACA 0015	4.9597	11.1%	0.43	4.0%
NACA 0018	4.4652	0.0%	0.4133	0.0%
NACA 0021	3.7173	-16.7%	0.2355	-43.0%
NACA 0025	3.6371	-18.5%	0.2457	-40.6%
Optimized Trade-Off	7.4267	66.3%	0.4542	9.9%

Table 4.3: Maximum power production, power coefficient and percentage variation from the baseline configuration for the different analysed configurations.

4.1.3 Conclusions

The present work considered the FP7 DeepWind rotor for an aerodynamic analysis of different blade parameters. In the baseline design, a two bladed rotor with NACA 0018 profiles was considered. The comparison shows the aerodynamic effect of a change in the number of blades. A blade number equal to two or three is equally a good choice with respect to the rotor loads. Further reduction in the loads can be obtained by adding one additional blade, however this would increase substantially the rotor cost and therefore the cost of energy. The choice between two and three blades should be conducted considering the rotor basement, evaluating which load (thrust or side) is more suitable for the whole turbine.

Considering different airfoils, NACA 0015 and NACA 0018 are the two best alternatives from a power production point of view. Increasing the airfoil thickness would lead to a sensible decrease in the performance, however linked to a decrease in the blade loads. The choice between the two selected profiles should be conducted based on structural considerations, given that the performance does not change considerably between the two configurations.

Finally, an optimization campaign is conducted on the chord distribution along the blade span, aiming to maximize the power production. The optimization result was manually corrected in order to create a smooth parameter trend. The new blade configuration provided a

sensibly increased power production but at the same time a substantial increase in the thrust coefficient. This very interesting result represents only the first step for the optimization procedure, which will involve additional iterations between the structural and aerodynamic analysis.

4.2 Tilted Troposkien

The purpose of the present work is to provide a modelling approach to forecast the aerodynamic performance of a tilted Darrieus rotor with a Troposkien shape. The limitations of conventional semi-empirical methods are overcome by considering an unsteady three-dimensional URANS $k-\omega$ SST CFD model, whose validation against experimental data for a 2-meter rotor [37] is presented in Section 2.4. This size is adopted, beside for the availability of experimental data, to compare the numerical predictions with the 2-meter DeepWind demonstrator [130], which is operating in these particular conditions. Results, however, have general validity, since the Troposkien shape is simply scaled for turbines characterized by larger dimensions.

4.2.1 Results and Discussion

The domain for the tilted Darrieus simulation is created by rotating the *cylinder* domain around the rotor virtual central point with a defined angle. The *gallery* domain is reconstructed afterwards, as showed in Figure 4.13. The rotor rotation and the torque calculation are specified considering the new tilted axis.

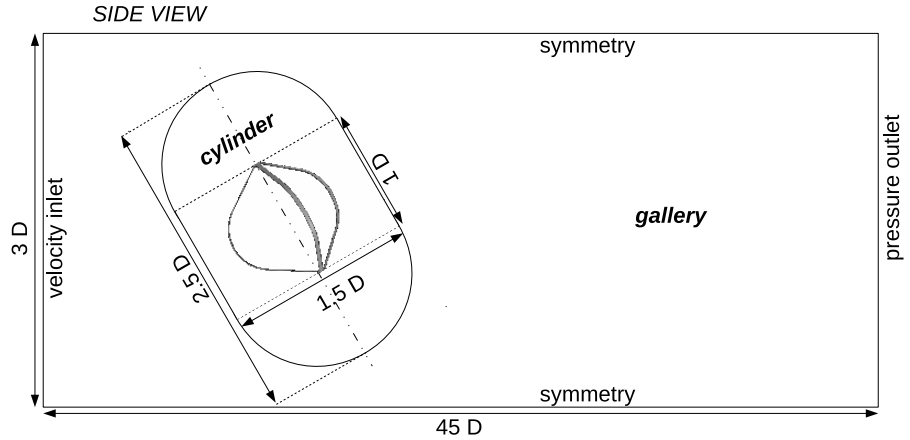

Figure 4.13: Scheme of the computational domains for the tilted configuration with boundary conditions and sizes, no to scale.

During offshore operations, the rotor blades should not impact the water during rotation. The tilt angle is therefore expected, and should be forced, not to exceed the angle at the Troposkien root, which is about 30°. Simulations are therefore conducted considering two tilted configurations, with a tilt angle equals to 10° and 20°. The power production P with respect to the free-stream wind speed V and the power coefficient C_P with respect to the tip speed ratio λ for the two tilted configurations are reported in Figure 4.14, whereas the peak power coefficient values, the relative tip speed ratios and their variations with respect to the vertical configuration are reported in Table 4.4.

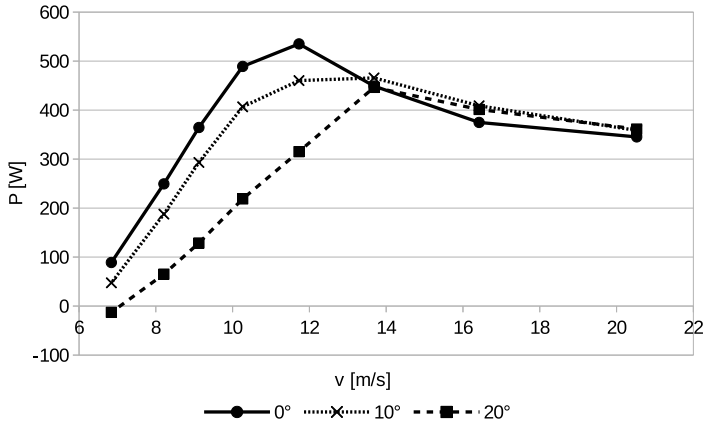

(a) Power production with respect to the wind speed.

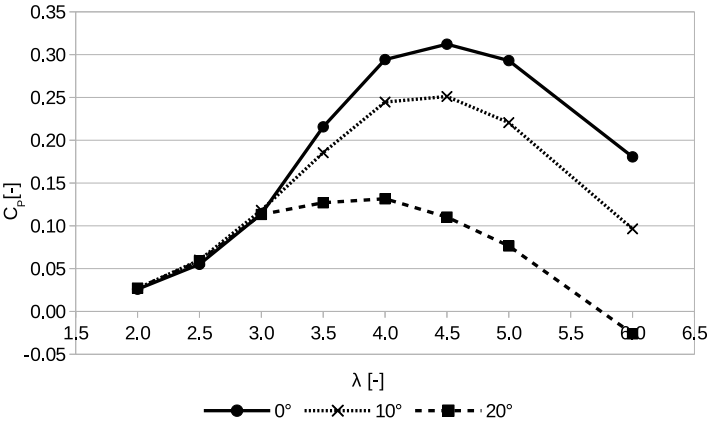

(b) Power coefficient with respect to the tip speed ratio.

Figure 4.14: Aerodynamic performance for the two tilted configurations obtained with the URANS CFD simulations.

Configuration	$\lambda\|_{C_{\mathrm{P,max}}}$ [-]	$C_{\mathrm{P,max}}$ [-]	$\Delta\lambda\|_{C_{\mathrm{P,max}}}$ [-]	ΔC_P [-]
0°	4.5	0.3122		
10°	4.5	0.2511	0.00%	-19.57%
20°	4.0	0.1316	-11.11%	-57.83%

Table 4.4: Peak power coefficient values, relative tip speed ratios and variations with respect to the vertical configuration.

The comparison between the performance of the non-tilted and tilted rotors can be analysed by considering the rotor behaviour before and after a particular operative point characterized by the operative condition of $\lambda = 3$, approximately equal to $v = 14m/s$. The tilted rotor operating at high tip speed ratios, corresponding to lower wind speeds, i.e. lower angles of attack, is experiencing an expected decrease in the power production due to the unfavourable effective wind direction. As reported by Johnson [131], the aerodynamic forces in a yawed wing can be estimated, for small angles of attack, by considering the two-dimensional aerodynamic coefficients but with different wind speeds: the lift and the drag force should be computed, respectively, using the projected and the free-stream wind speeds, the former lower than the latter. Consequently, the reduction in the lift force with respect to the drag force will lead to a reduction in the rotor torque.

As stated before, this trend is generally considered in the semi-empirical analysis by reducing the inflow wind speed, approximately by the cosine of the tilt angle [25, 26]. Figure 4.15 shows a comparison between the performance estimated by the URANS CFD approach and those obtained by interpolating the simulation results with a reduced inflow wind speed calculated as:

$$v = v_\infty \cdot \cos\beta \tag{4.5}$$

The accuracy of the prediction obtained by projecting the wind speed is very limited since performance is over-predicted with respect to the URANS CFD simulations for the lower wind speeds. Whereas a shifting trend of the production curve can be still observed, as the peak production is reduced and moved to higher wind speeds, a more accurate model to be adopted in semi-empirical methods is needed to predict this aerodynamic effect for tilted rotors.

The tilted rotor performance at tip speed ratios lower than $\lambda = 3$ are comparable to the vertical rotor configuration. The power coefficient values are super-imposed whereas a small increase in the power performance is observed. The reason behind this behaviour can be found in the profile aerodynamics. In the operative conditions above the peak power production, in fact, the rotor is operating at stalled conditions with large angles of attack. In these conditions, small variations in the angle of attack, due to the rotor tilt, lead to limited variations around the zero value of the tangential force coefficient C_t [21], defined as:

$$C_t = C_L \sin\alpha - C_D \cos\alpha \tag{4.6}$$

The coefficient values with respect to different angles of attack derived from the experimental NACA 0012 coefficient database developed by Jacobs [44] and extended by Bedon et al. [132]

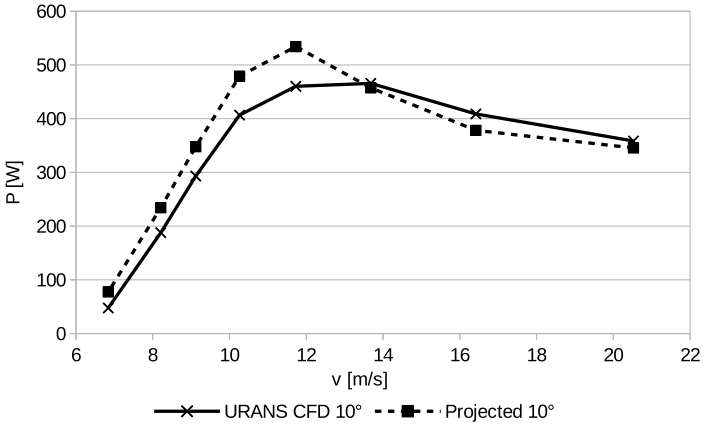

(a) Tilt angle of 10°.

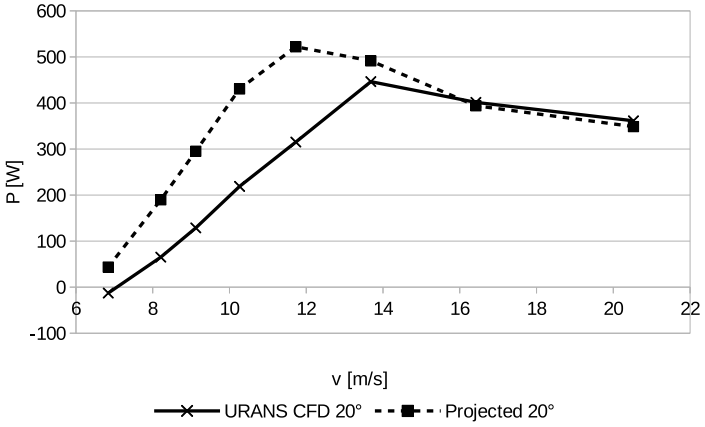

(b) Tilt angle of 20°.

Figure 4.15: Performance of the two tilted configurations, estimated by URANS CFD simulations and interpolation of the curve with a reduced wind speed.

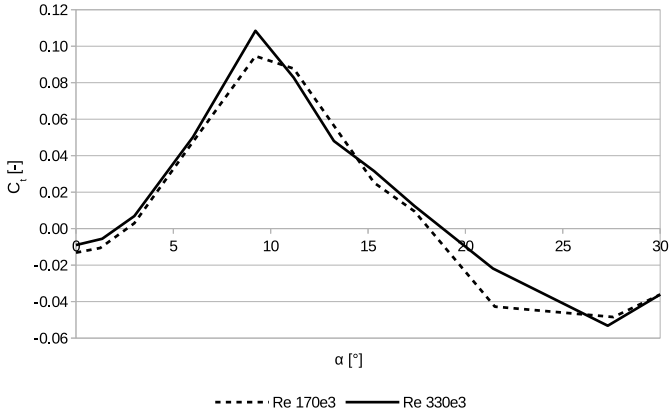

Figure 4.16: Tangential force coefficient C_t with respect to the angle of attack for two operational Reynolds numbers.

are plotted in Figure 4.16 for two Reynolds numbers typical of these operative conditions. Variations in the rotor torque, calculated from the average C_t value, are therefore limited too. This explanation can be also confirmed by observing that the performance obtained by projecting the wind speed on the rotor plane, which involves a small change in the angle of attack, are in good agreement with those from URANS CFD simulations. Moreover, since the three-dimensional nature of the separated flow due to the boundary layer detachment influences the whole blade aerodynamics [56], no relevant differences between the tilted and vertical configurations should be expected.

4.2.2 Conclusions

This work presented a CFD-based study of the aerodynamic performance of a Darrieus wind turbine operating under tilted conditions.

Two tilt angles were considered due to the operative restrictions linked to the Troposkien shape: 10° and 20°. The performance of the VAWT was reported in terms of the power production and the power coefficient. As expected, a reduced performance was observed with increasing tilt angle. However, two different trends were observed as a function of the tip speed ratio. For high tip speed ratios, a strong decrease in the power coefficient was observed. This performance attenuation is linked to the yawed airfoil theory. A comparison between the URANS estimations and the results obtained by simply projecting the wind speed along the rotor plane highlighted the limitation of the second approach, which is unable to account for the three-dimensional effects due to the tilted inflow. At low tip speed ratios, the tilted rotor performance was comparable with the perfectly vertical configuration. This behaviour is linked to the stalled operative conditions of the rotor, since the tangential coefficient C_t is little varying with a variation of the angle of attack. Estimations based on the wind speed projection, which relies on the same hypothesis, are in fact accurate.

These computational predictions represent the first attempt to provide an estimation of the aerodynamic performance in tilted configurations, which are often experienced in offshore conditions. A validation with experimental results would provide a final confirmation on the accuracy of the CFD approach and would allow to perform a deeper analysis of the Darrieus aerodynamics in these unconventional operative conditions. Moreover, corrections for semi-empirical models could be developed in order to overcome the actual limitations, leading to more complete theories which could be adopted in much comprehensive analyses.

4.3 Airfoil Optimization

The question regarding which type of airfoil is to be addressed as "optimal" in Darrieus Vertical Axis Wind Turbines (VAWTs) is a largely debated theme. As underlined by Sandia [7], the use of an optimal design for the airfoil blades would, in fact, significantly reduces the cost of energy. In literature, a considerable number of researchers provided different improved solutions with respect to aerodynamic, structural and control aspects. The problem is approached considering different simulation and optimization methodologies, trying to find an optimal balance between the computational complexity and the extension of the investigation field.

Different authors presented several approaches based on different physical considerations. The present work aims to develop an optimization routine whose target is to increase the global aerodynamic performance of the Darrieus rotor, as it will be more extensively presented in the next section. Beside the simulation algorithm, the physics of the problem is not further simplified, avoiding the introduction of additional constraints and preventing the solution to converge to a different result.

Genetic and evolutionary algorithms represent the most natural choice to perform the airfoil optimization given the uncertainty in determining a direct link between geometric parameters and rotor performance [31]. In the present work, the elitist genetic algorithm NSGA-II modified by Deb [133] is adopted.

The airfoil is generally varied considering a profile family. On one hand, this choice enables a fast convergence of the optimization algorithm, since only a limited number of parameters is varied and deformed shapes are avoided. On the other hand, the research span is considerably limited, since variations outside the family domain are not considered. In this work, a wide exploration of the optimization area is privileged at the expense of convergence time. As a consequence, airfoil is represented by two Bézier curves, respectively for the description of the mean line and the thickness distribution, similarly to the approach described by Derksen and Rogalsky [134].

A variety of simulation tools are adopted based on the researcher choice to privilege the computational complexity or the solution accuracy. In the present work the 2D URANS CFD model validated in Section 2.3 is adopted due to the need for a simulation algorithm both flexible in terms of airfoil geometry and fast to be implemented in an optimization loop.

The considered baseline rotor geometry for the optimization is the same adopted for the validation of the simulation model, the two-blade 500 kW Darrieus vertical axis wind turbine tested by Mays [117]. The rotor, whose main geometrical characteristics are reported in Table 2.7, is equipped with two blades having NACA 0018 airfoil section.

4.3.1 Optimization Rationale

The aerodynamics of the Darrieus vertical axis wind turbines is a largely debated theme in literature. Given the complexity linked to the unsteadiness of the operative conditions, different models were developed with the aim of providing a reliable estimation of the aerodynamic performance. As shortly introduced before, a higher model accuracy is generally linked to a higher computational effort. The global computational load is generally exponentially increased using an optimization routine, since several fitness evaluations are required for the algorithm to converge.

On the other hand, the constraints imposed in the previous literature works are extremely limiting: the results can not be interpreted as the best airfoils to be used in a Darrieus turbine. The limitations on the airfoil geometry in fact prevent a complete exploration of the solution space: a symmetric or NACA airfoil can not be established in advance as the optimal shape for these machines. Moreover, performance estimations based on static coefficients do not consider all the dynamic effects which deeply influence the rotor behavior.

The present work aims to provide an optimization method which overcomes the previous limitations. An efficient exploration of the solution space is guaranteed by two Bézier curves which can describe a wide range of airfoil shapes, similarly to the approach described by Derksen and Rogalsky [134], whereas the 2D URANS simulation tool validated in Section 2.3 can provide a reliable estimation of the rotor unsteady behavior. The simulation using a semi-empirical method, such as BEM, coupled with an aerodynamic coefficient estimator, such as XFOIL [135, 136], would in fact neglect time-dependent effects, e.g. dynamic stall: empirical corrections are tuned, in fact, only for well-known airfoils and not available on a general basis. However, two-dimensional simulations can be argued not be accurate enough for simulating the VAWT aerodynamics since three-dimensional effects are neglected. Two-dimensional simulations are widely considered in literature to perform these type of calculations [75, 109] due to the reduced number of elements and good agreement with experimental data for straight bladed VAWT [137]. The reduced number of elements makes it possible to estimate the performance for a single tip speed ratio in 24 h, whereas a three-dimensional simulation would require 416 h on the same machine [115]. The only chance to perform an airfoil optimization involves therefore two-dimensional simulations: the optimization in this work, which implied 90 fitness function evaluations, required 3 months, whereas the same task using three-dimensional simulations would have required approximately 4.3 years on the same computer. Moreover, the use of three-dimensional simulations would constitute a different optimization rationale which is strongly dependent to the baseline rotor architecture (e.g. blade length, spoke placement, etc.). The present optimization is therefore aimed to obtain the best airfoil to achieve the maximum performance in a generic Darrieus rotor, since the two-dimensional result can be scaled to different diameters.

4.3.2 Optimization Methodology

The optimization is aimed to provide an airfoil shape to improve the aerodynamic performance, whereas all the remaining geometrical parameters (i.e. rotor diameter and chord length) are kept constant. The optimization process is conducted considering an iterative loop which includes the URANS CFD simulation tool described in Section 2.3, a fitness calculator, an optimization algorithm and a rotor geometry generator. A scheme of the optimization loop is reported in Figure 4.17.

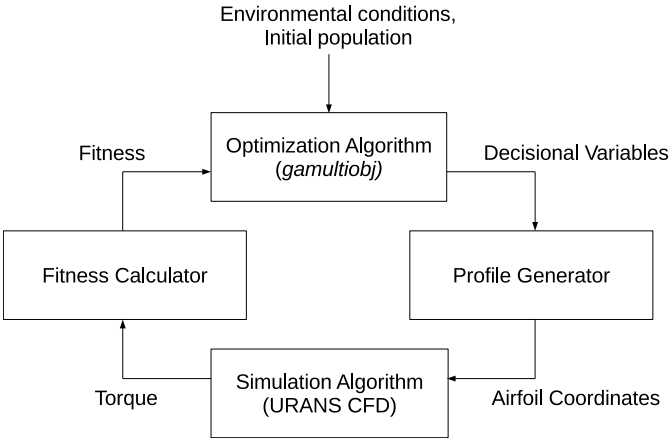

Figure 4.17: Scheme of the optimization loop showing the main iterative steps.

As *Optimization Algorithm*, the elitist genetic algorithm NSGA-II modified by Deb [133] is adopted as implemented in the Matlab *gamultiobj* function [138]. The algorithm involves an elitarism selection based on the phenotype distance, a roulette wheel parent selection, an uniform crossover and a mutation function based on the Gaussian. The algorithm is set to evolve 15 individuals for 5 generations. An initial population to start the optimization procedure is needed. To increase the convergence possibility and to evaluate the performance improvement, the airfoils which are mostly adopted in VAWT applications, i.e. NACA 0012, NACA 0015, NACA 0018, NACA 0021 [132] and DU 06-W-200 [139] are provided. The remaining individuals are randomly generated.

The selection of the best individuals is performed based on the fitness value derived from the simulation results. The original rotor configuration performs at the maximum power coefficient for a wind speed of 7 m/s: this wind speed is therefore targeted for optimization. By increasing the torque value, the power production would be increased too. However, in order to provide the genetic algorithm with a clearer path to optimize the airfoil and given the most of the power is generated in the upwind section, two optimization objectives are considered:

- the rotor total torque T_{tot}, calculated as an average during one revolution;

- the rotor upwind torque T_{up}, calculated as an average in the upwind azimuthal positions.

The genetic algorithm aims to minimize the fitness values: the *Fitness Calculator* therefore provides the additive inverses of the rotor total and upwind torque.

The decision variables varied during the optimization algorithms are interpreted by the *Profile Generator* as coordinates for two Bézier control curves which describe the non-dimensional chord line and thickness distribution. In particular, every individual is generated as follows:

- The chord line is generated by 7 control points. The first and last points are respectively placed at $(0; 0)$ and $(1, 0)$ whereas 10 decision variables are interpreted as abscissas and ordinates for the remaining 5 control points.
- The thickness distribution is generated by 7 control points. The first and last points are respectively placed at $(0; 0)$ and $(1, 0)$ and the abscissa for the second point is fixed at 0 in order to ensure the leading edge tangency. The ordinate for the second point and the coordinates for the remaining 4 control points are provided by 9 decision variables.

As an example, the two Bézier curves describing the DU 06-W-200 profile are shown in Figure 4.18.

4.3.3 Results and Discussion

Starting from the initial population including the baseline rotor airfoil (NACA 0018), the optimization loop evolved the individuals for five generations. The evolution is appreciable by representing the fitness values as Pareto fronts [140, 141], where only the non-dominated solutions are inserted, as shown in Figure 4.19. Moreover, the fitness values obtained simulating the rotor with the traditional airfoils are also highlighted. The optimization successfully provided solutions with a higher upwind and total torque, which continuously increases as long as the optimization is performed.

Different configurations are found in the Pareto front of the last generation. Since the second fitness, the upwind torque, was inserted only to drive the genetic algorithm, the configuration with the highest total torque should be chosen as final optimization result. The airfoil with the highest torque is named "WUP 1615" (Wind Team of University of Padua, numbered as NACA convention). The profile is represented in Figure 4.20 with the relative mean line and thickness distribution.

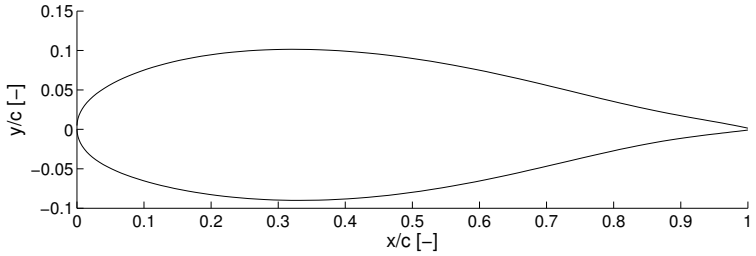

(a) DU 06-W-200 profile.

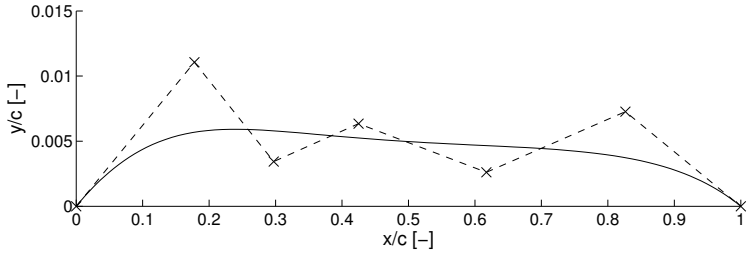

(b) Bézier curve for the mean line (solid line) and control points (dashed line).

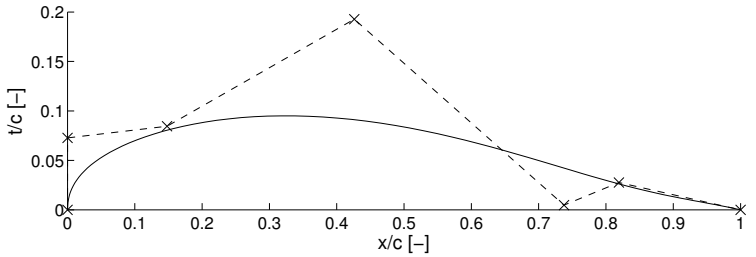

(c) Bézier curve for the thickness distribution (solid line) and control points (dashed line).

Figure 4.18: Profile parametrization for the DU 06-W-200 profile.

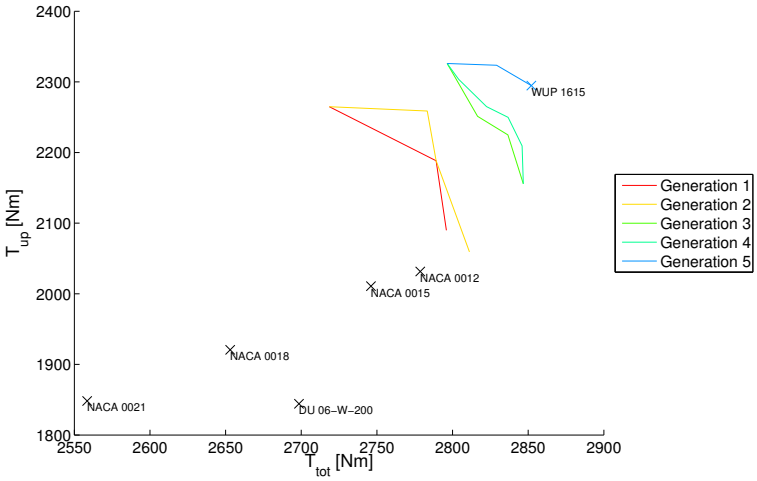

Figure 4.19: Pareto front evolution starting from the initial population, including the baseline rotor airfoil (NACA 0018).

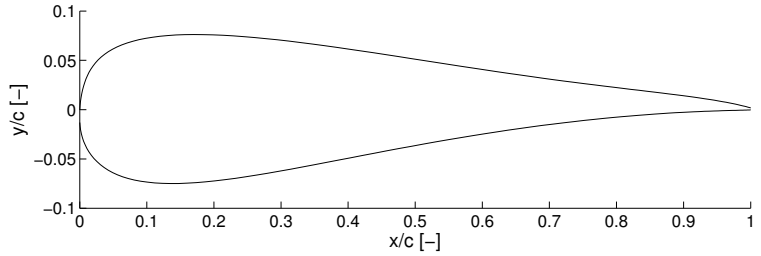

(a) WUP 1615 profile.

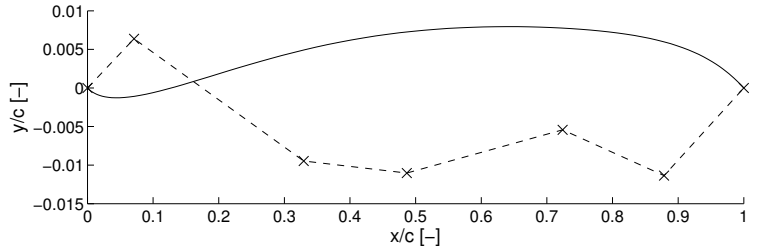

(b) Bézier curve for the mean line (solid line) and control points (dashed line).

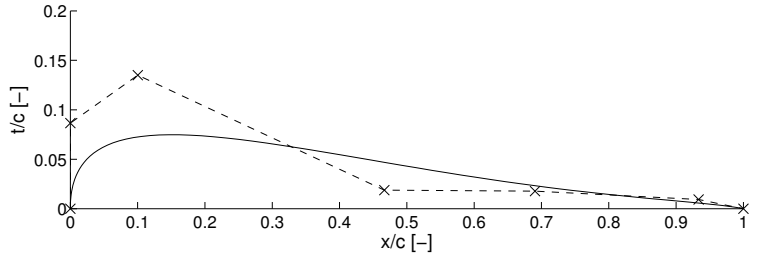

(c) Bézier curve for the thickness distribution (solid line) and control points (dashed line).

Figure 4.20: Profile parametrization for the WUP 1615 profile.

The profile shape sensibly differs from the traditional airfoil ones. The airfoil presents an almost symmetric shape near the trailing edge, with the mean line aligned with the chord. At about $0.15c$ the mean line deviates to reach the maximum offset of $0.005c$ at $0.6c$. This offset is maintained up to $0.8c$, where the mean line approaches the trailing edge with a strong curvature. The thickness profile presents instead a smoother trend than the mean line. The maximum thickness of $0.08c$ is reached at about $0.15c$, with an almost linear decrease up to the trailing edge.

Additional considerations on the profile aerodynamics will be presented in the next section. Given the global approach adopted for the optimization process, a comparison in terms of ratio between the numerical simulation power coefficients of the rotors equipped with NACA 0018 and WUP 1615 is shown in Figure 4.21. The rotor equipped with the WUP 1615 profile is characterized by a peak power coefficient value 8% higher than the baseline configuration. A Maximum Power Point Tracking (MPPT) tracking control, widely adopted in the modern

wind engineering, would therefore allow to obtain a higher power production. Moreover, the peak power coefficient is achieved at the same tip speed ratio λ of about 4, thus avoiding to operate at higher rotational speeds which will affect the structural performance, especially in a straight blade rotor.

A smooth decrease in the power coefficient is observed for higher tip speed ratios, similar to the NACA 0018 configuration. The trend is instead steeper than in the baseline at tip speed ratios lower than 3, linked to the conditions for the rotor operating at fixed maximum rotational speed and wind speeds higher than nominal. This peculiarity could represent an advantage on the control side, since the rotor would eventually stall for operating conditions above nominal and reduce the power production. On the other hand, the structure would experience a higher load during deep stall conditions. Therefore, a sensible variation in the rotor structural design could be necessary due to the increased load, but further considerations are not possible since the reference paper does not provide any structural information.

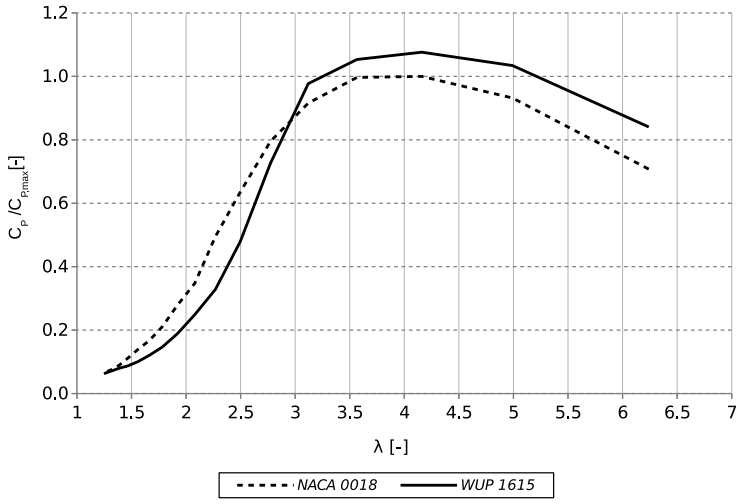

Figure 4.21: Ratio between the numerical power coefficients and the numerical baseline maximum value for different tip speed ratios, rotors equipped with NACA 0018 and WUP 1615.

The performance of the two rotors can be further analysed by considering the variation of the torque and normal force with respect to the azimuthal coordinate for different tip speed ratios. Figures 4.22 and and 4.23 show respectively the polar charts for torque and and normal forces of a single blade for the tip speed ratios of $\lambda = 4.2$, $\lambda = 3$, $\lambda = 2.5$ and $\lambda = 2$, equivalent to wind speeds of $v = 6\ m/s$, $v = 8.32\ m/s$, $v = 10\ m/s$ and $v = 12\ m/s$.

Both rotors work in non-stall conditions along all the azimuthal position for the wind speed of 6 m/s. In particular, the rotor equipped with the WUP 1615 airfoil outperforms the one with NACA 0018 in the whole upwind region, whereas on the downwind side the torque is lower since the wind speed is strongly decreased. At a wind speed of 8.32 m/s, corresponding to

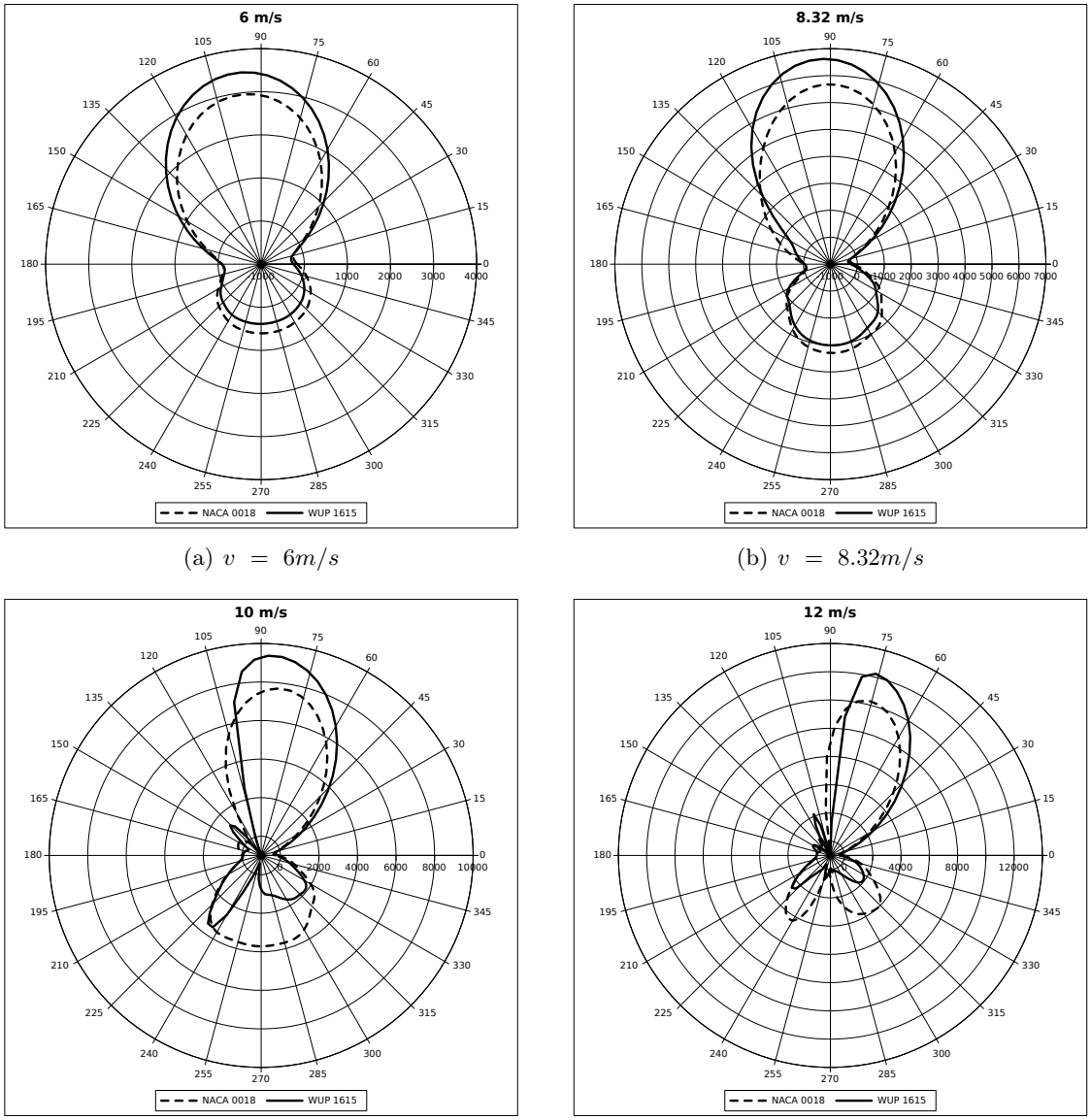

(a) $v = 6m/s$ (b) $v = 8.32m/s$

(c) $v = 10m/s$ (d) $v = 12m/s$

Figure 4.22: Torque values [Nm] for the single blade with respect to the azimuthal position [°] for different wind speeds.

$\lambda = 3$, the two rotors provide the same power production, as can be observed in Figure 4.21. The torque values for the WUP 1615 rotor are still higher than the NACA 0018 rotor for most of the upwind region, but a steep fall in performance is observed at an azimuthal position of about 130° due to the profile incurring in stall conditions. This effect, combined to the lower production in the downwind region, reduces the total production to the baseline rotor level. Finally, for the highest analysed wind speeds of 10 m/s and 12 m/s, both the rotors work with stalled blades but, since the NACA 0018 airfoil experiences a smoother stall behavior and reduced fall of lift coefficient than WUP 1615, the total power production for the rotor equipped with the former profile remains higher.

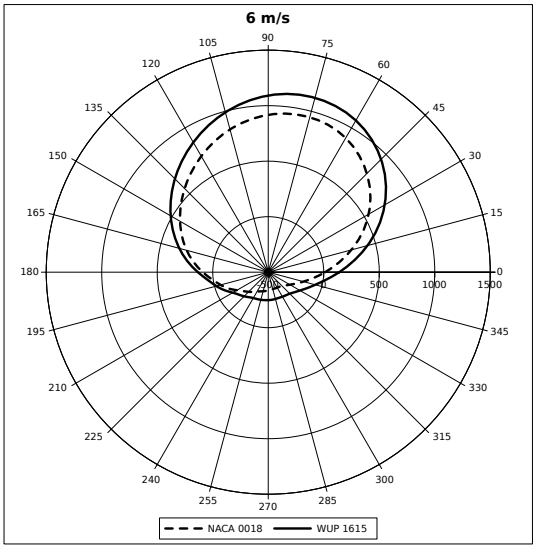

(a) $v = 6m/s$

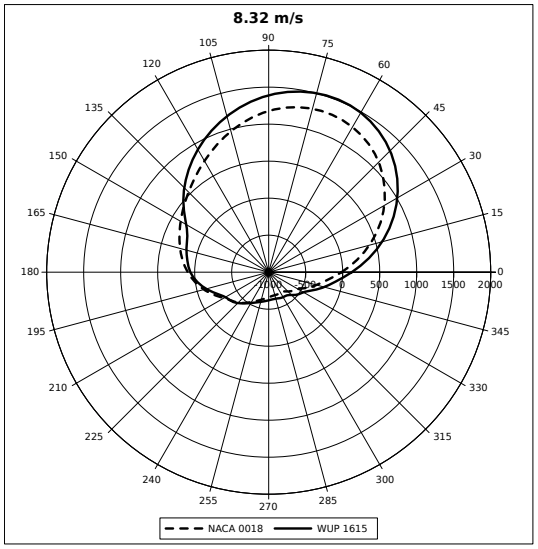

(b) $v = 8.32m/s$

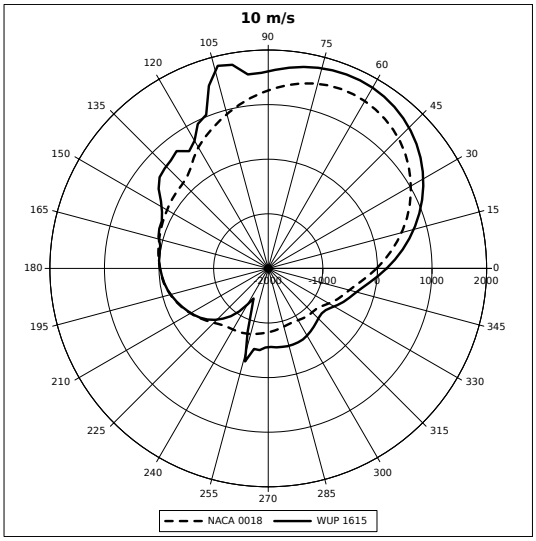

(c) $v = 10m/s$

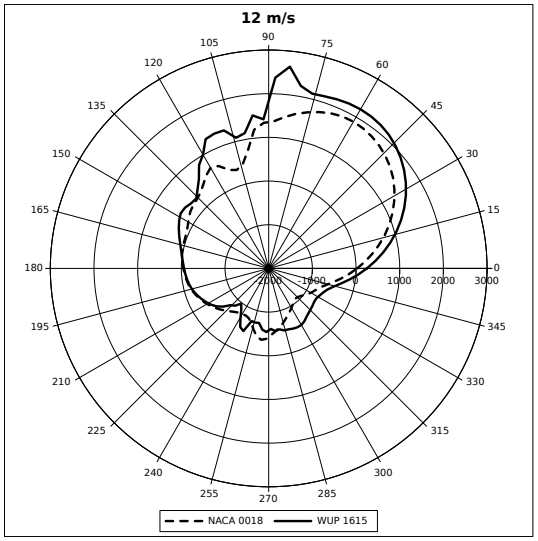

(d) $v = 12m/s$

Figure 4.23: Normal force values [N] for the single blade with respect to the azimuthal position [°] for different wind speeds.

On the other hand, normal force is sensibly decreased in the rotor equipped with the WUP 1615 airfoil with respect to the NACA 0018 rotor for all the considered operative conditions. The flatwise stress deriving from the aerodynamic load is therefore reduced, even though its influence is limited with respect to the centrifugal force for this type of rotors [78, 79].

4.3.4 Airfoil Aerodynamics

A deeper insight on the WUP 1615 airfoil aerodynamics is provided to explain the higher rotor performance obtained by the optimization process. The airfoil lift and drag coefficients are estimated considering two simulation approaches:

- URANS $k-\omega$ SST model, considering the same simulation mesh adopted in the rotor simulation;
- simulation code RFOIL, which exploits the viscous panel code method implemented in XFOIL [135, 136] matched with a new set of closure equations to improve the estimations of the post-stall region [142, 143].

The considered Reynolds number is $3 \cdot 10^6$, which is similar for the rotor operative conditions. The numerical values of the aerodynamic coefficients for the NACA 0018 and WUP 1615 airfoils are shown in Figure 4.24, whereas the values of the drag coefficient at an angle of attack of 0° and the minimum drag coefficients are respectively reported in Tables 4.5 and 4.6.

Airfoil	**URANS $k-\omega$ SST**	**RFOIL**
NACA 0018	0.01105	0.00633
WUP 1615	0.01013	0.00839

Table 4.5: Drag coefficients at an angle of attack of 0° for the NACA 0018 and WUP 1615 airfoils.

Airfoil	$C_{D,min}$ [-]	$\alpha\|_{C_{D,min}}$ [°]
NACA 0018	0.00633	0
WUP 1615	0.00773	-1

Table 4.6: Minimum drag coefficients and their angles of attack for the NACA 0018 and WUP 1615 airfoils estimated with RFOIL.

A good agreement for the numerical aerodynamic coefficients, estimated with the different simulation codes, is registered for angles of attack between $-15°$ and $+15°$. The airfoil operates with positive angles of attack in the upwind side, where the rotor production is higher. In this region, the WUP 1615 airfoil presents higher values of the lift coefficients compared to NACA 0018 due to the camber. However, the NACA 0018 behavior after stall is smoother than for WUP 1615, which is also characterized by a sensible increase in the drag coefficient. The abrupt decrease in power coefficient at low tip speed ratios for the rotor equipped with WUP 1615 airfoil, as shown in Figure 4.21, can be therefore related to the abrupt decrease in the airfoil efficiency, highlighting a working condition that should be avoided in the rotor operative life.

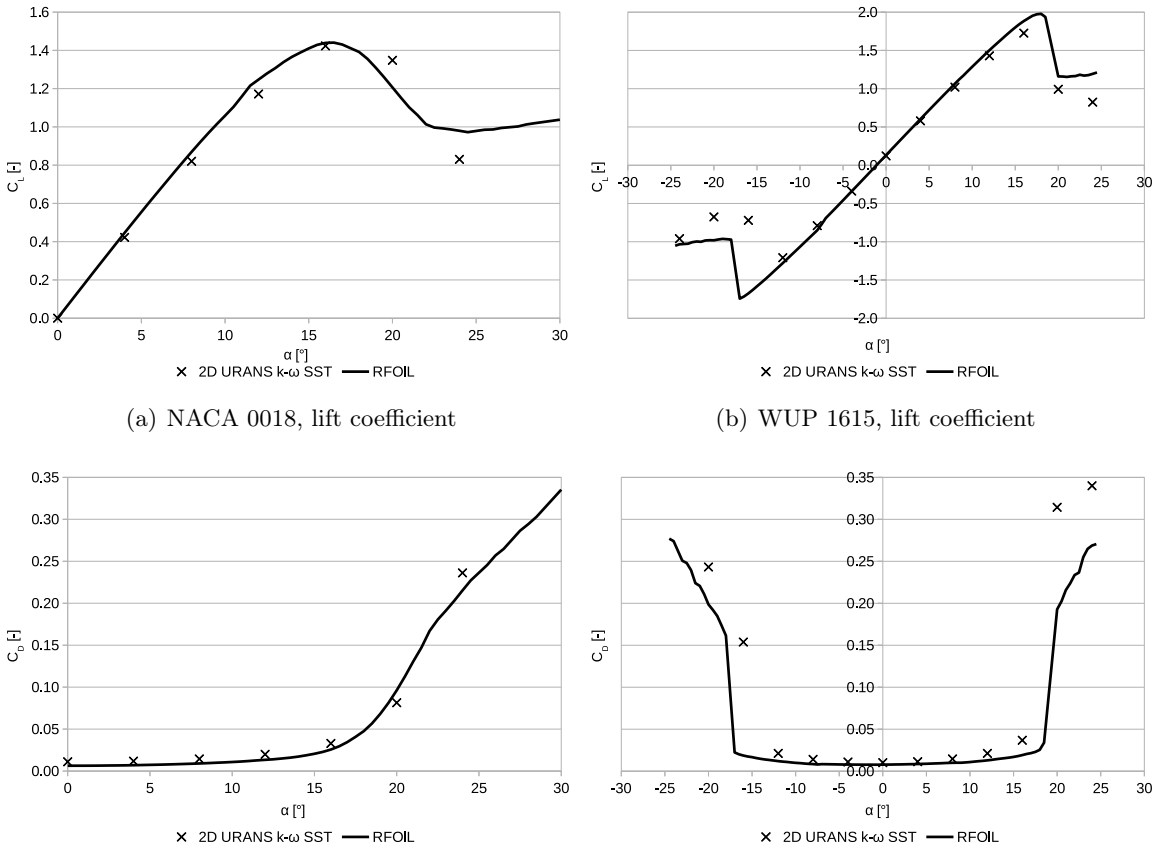

(a) NACA 0018, lift coefficient

(b) WUP 1615, lift coefficient

(c) NACA 0018, drag coefficient

(d) WUP 1615, drag coefficient

Figure 4.24: Aerodynamic coefficients estimated by URANS $k - \omega$ SST and RFOIL simulations for the NACA 0018 and WUP 1615 airfoils.

The aerodynamic coefficients at negative angles are instead comparable between the two airfoils, with the only difference for the WUP 1615 immediately before stall, which exhibits a higher lift coefficient. Even in this region, the stall is abrupt with a consequent increase in the aerodynamic drag values.

The increased lift of the WUP 1615 airfoil for positive angles of attack with respect to NACA 0018 can be further investigated by considering the pressure coefficient values along the chord line, which are evaluated with RFOIL and reported in Figure 4.25 for three different angles of attack before stall, where the panel code reliability is higher.

The stagnation point for the two airfoils is located in the same position at the considered angles of attack, due to the similarity in the profile shape near the leading edge. However, a considerable difference is registered for the pressure coefficient trends.

The suction side experiences a lower pressure in the WUP 1615 airfoil compared to NACA 0018 even at lower angles of attack, with a peak located at the same position of about $0.03c$. On the

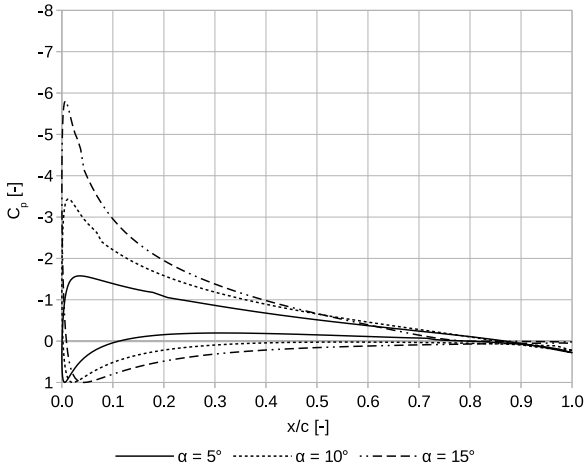

(a) NACA 0018

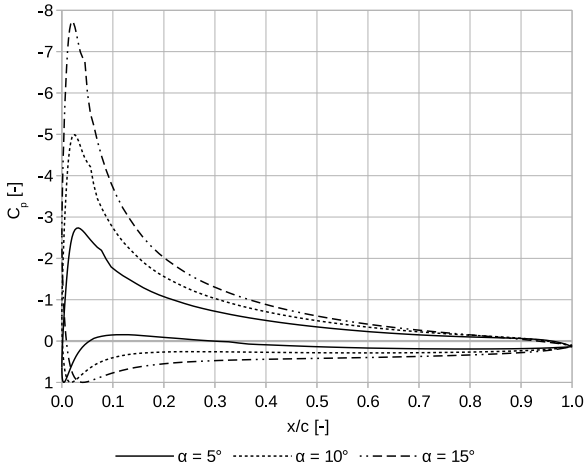

(b) WUP 1615

Figure 4.25: Pressure coefficients for the NACA 0018 and WUP 1615 airfoils at different angles of attack, Re $3 \cdot 10^6$.

other hand, the pressure recovery towards the trailing edge for WUP 1615 is less smooth than for NACA 0018. The adverse pressure gradient is however not critical since earlier boundary layer separations are avoided, as can be observed in the aerodynamic coefficient curves in Figure 4.24.

The pressure coefficient trends on the pressure side are instead similar. Nevertheless the pressure difference between suction and pressure sides, which is almost extinguished for NACA 0018 at about $0.8c$ for high angles of attack, is still persistent up to about $0.95c$ in the WUP 1615 case, as can be seen in Figure 4.26, providing an important contribution for the total lift force. On the other hand, a larger adverse pressure gradient on the suction side of the WUP 1615 airfoil than on the NACA 0018 airfoil is registered at identical angles of

attack: this condition is favorable with boundary layer separation and stall. When the profile incurs in stall conditions, the stall would be abrupt with a separation point moved towards the leading edge.

Finally, the trailing edge pressures are similar in both airfoils and slightly positive.

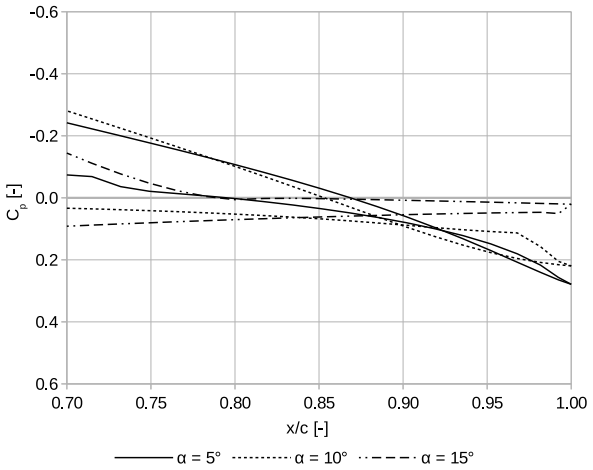

(a) NACA 0018

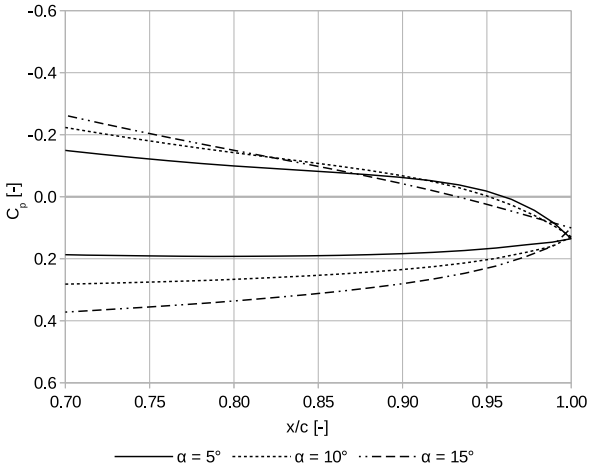

(b) WUP 1615

Figure 4.26: Pressure coefficients near the trailing edge for the NACA 0018 and WUP 1615 airfoils at different angles of attack, Re $3 \cdot 10^6$.

The coefficients here reported, being derived in steady conditions, provide a good representation of the airfoil aerodynamics and can be adopted in semi-empirical algorithms like those based on Blade Element Momentum (BEM) theory. However, the airfoil experiences during the wind turbine cycle different operative conditions than those assumed with steady-state calculations. It is therefore interesting to compare the steady state performance with dynamic coefficients which can be obtained by CFD calculations. The dynamic and

static coefficients for the WUP 1615 airfoil operating at a tip speed ratio of $\lambda = 2.5$ are reported in Figure 4.27. The dynamic coefficients are referred to the geometrical angles of attack, neglecting therefore rotor-induced perturbations of velocity intensity and direction.

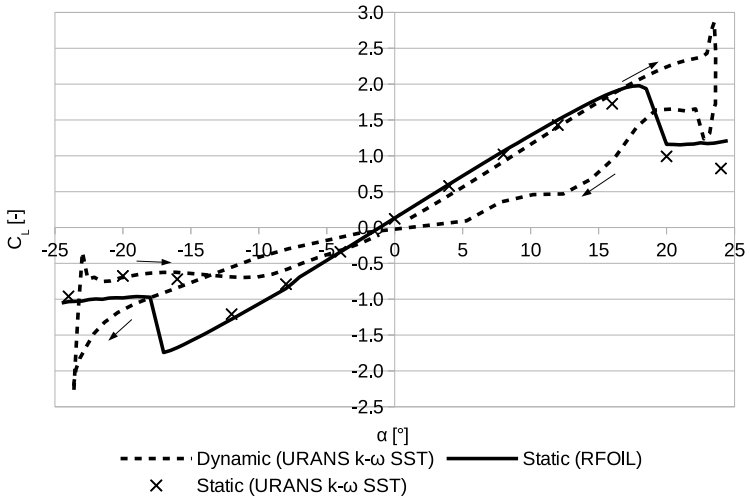

(a) Lift Coefficient

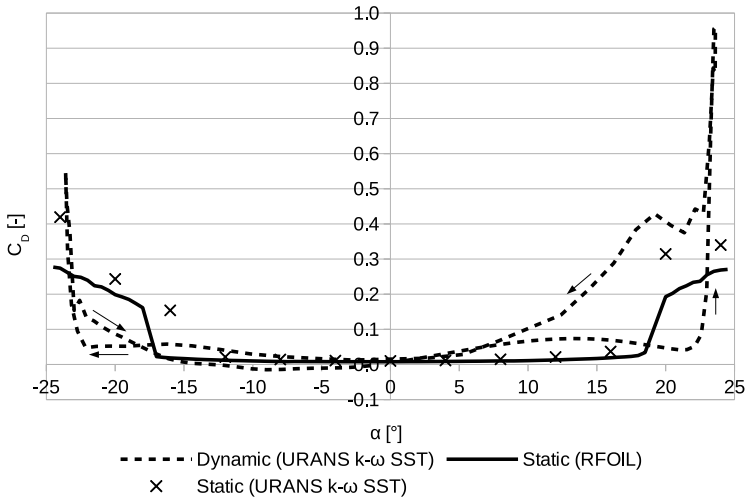

(b) Drag Coefficient

Figure 4.27: Static and dynamic lift coefficients, WUP 1615 airfoil at Reynolds number of about 3*e*6 and tip speed ratio of $\lambda = 2.5$.

The dynamic lift coefficients considerably exceeds the static values for the positive angles of attack whereas, at negative angles, both trends and values are similar. The most important difference is shown for the drag coefficient: the increased lift above the static stall condition is coupled with a drag outbreak at the dynamic stall conditions, which presents values higher up to 500%. This brutal stall behavior, as expected, could be the main responsible for the decrease in the power performance at low tip speed ratios. A similar behavior, but limited to lower drag values, is observed at negative angles of attack. This behavior is typically hindering the

power output capabilities of a vertical axis turbine. The variation ranges of the blade angle of attack with respect to different rotor operative conditions in terms of tip speed ratio is shown in Figure 4.28. The control system needs therefore to keep the operative tip speed ratio between $\lambda = 3.5$ and $\lambda = 4.5$ to maximize the rotor aerodynamic performance, as seen in Figure 4.21, and to limit the operative angles of attack below $\pm 17°$, avoiding the airfoil stall.

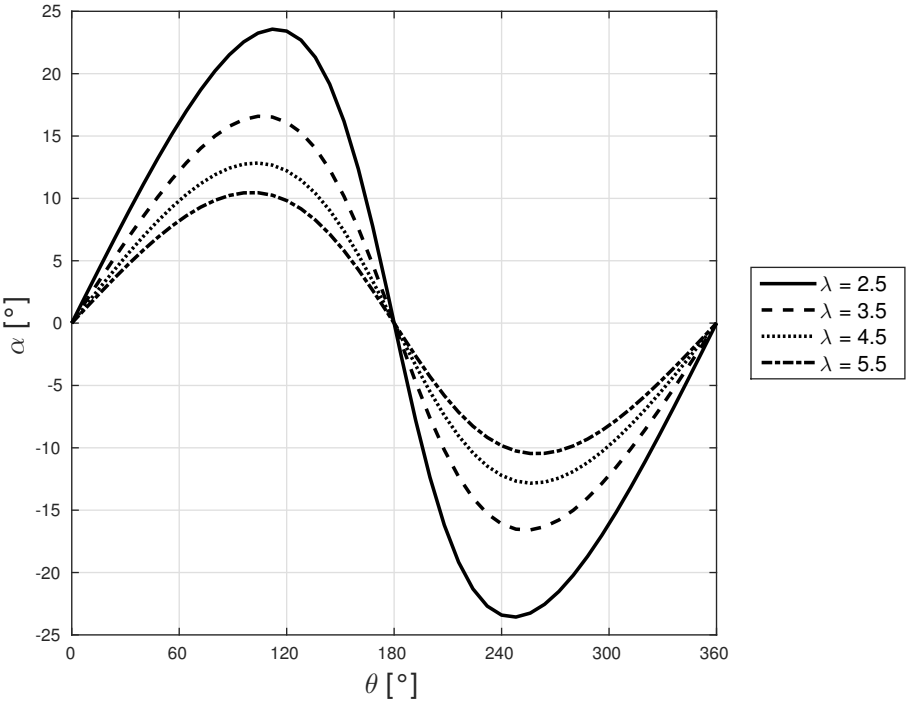

Figure 4.28: Variation ranges of the blade angle of attack with respect to different rotor operative conditions in terms of tip speed ratio.

4.3.5 Conclusions

A new airfoil profile, named WUP 1615, is provided by the optimization routine, which is characterized by a particular mean line and thickness distribution. The aerodynamic performance of the Darrieus rotor at the optimal working condition is in fact sensibly increased with respect to the baseline configuration with NACA 0018 airfoil. However the power coefficient curve presents a different trend: the rotor experiences a sudden fall in performance when the operative tip speed ratio is below a certain limit. The turbine should be therefore equipped with a control system enabled to perform a Maximum Power Production Tracking (MPPT) to exploit the maximum efficiency. This behavior is explained by considering the torque values with respect to the azimuthal position, which show an earlier stall for the blade equipped with the optimized airfoil.

A deeper analysis for the WUP 1615 airfoil is conducted to understand the global rotor results provided by the URANS CFD algorithm. The analysis included both static and a dynamic considerations, respectively derived from a panel code and CFD simulation. The profile is characterized by increased lift coefficients at positive angles of attack with respect to NACA 0018, which lead to an increase in the rotor performance. However, the profile experiences an abrupt stall with a consequent increase in the drag force, which affects the rotor performance and increase loads and vibrations at low tip speed ratios. At negative angles of attack, the lift coefficient presents almost the same values as NACA 0018. In the stall region, WUP 1615 presents an increased lift, with a similar abrupt stall as noted for positive angles of attack. The pressure coefficients along the chord line showed that an increased pressure difference between airfoil sides is registered especially near the leading and trailing edges.

The new profile represents the optimal airfoil to increase the power performance during the whole cycle of the Darrieus rotor, obtained through the use of URANS CFD simulations to catch the dynamic aspects of the rotor aerodynamics. Despite the considerable increase in aerodynamic performance, an estimation for the cost of energy reduction is hard to establish, since the investment costs and energy price are unavailable in literature. However, the optimization successfully provided an airfoil shape which outperforms the available airfoils and should be carefully considered in a new rotor design. On the other hand, the optimization activity was limited to one operative conditions, whereas a multiple objective optimization targeting two or more wind speeds would ensure increased performance in a broader range. A parallel analysis on the rotor structural response could also be implemented as concurrent optimization routine, with the aim to reduce the average and off-design loads.

4.4 Aero-structural Optimization

BEM and FEA can be efficiently coupled to perform a complete aero-structural analysis of the rotor. Given the considerable rotor size for offshore applications, a particular attention is given to structural aspects, which led to adopt in several prototypes a shape similar to the Troposkien [144]. The Troposkien is the particular shape assumed by a rotating rope, which therefore minimizes the bending stresses, without considering the gravity force [20]. While this simplification does not lead to important collateral stresses for small size rotors, this is not the case when big offshore rotors are dealt with. Variations from the Troposkien were proposed by several authors [18, 100], but a complete optimization considering both aerodynamic performance and loads is not documented in the open literature.

In this work, a new methodology to provide the optimal blade shape and chord distribution for a VAWT rotor is presented. This methodology involves the combined use of a validated aero-structural code to provide reliable structural and aerodynamic analyses coupled with an

advanced optimization code based on a genetic algorithm [133].

A baseline configuration is selected to perform the optimization and provide the optimal blade shape and chord distribution to maximize the power coefficient and minimize the flatwise stress. The selected baseline is the widely documented Sandia 34m wind turbine [80, 81, 100], whose main characteristics are presented in Section 4.2. The aerodynamic and structural algorithms adopted in the present work and their validation are presented in Section 2.1.2.4 and 3.1. The optimization algorithm, presented in Section 4.4.1, is coupled with the simulation code, providing an equilibrium solution in every blade azimuthal position, as presented in Section 4.4.2.

4.4.1 Optimization Algorithm

The adopted multi-objective genetic algorithm is based on the formulation from Deb [133] and is implemented as a tool in the commercial software Matlab [138]. The algorithm is programmed to perform an elitarism selection based on the phenotype distance, a roulette wheel parent selection, an intermediate crossover and a mutation function based on the Gaussian distribution. A total of 100 individuals are evaluated and evolved for 200 generations, providing a suitable range for the optimization process. Among the individuals of the first generations, the Sandia baseline is included.

The genetic algorithm provides a total of 20 decision variables ("genes") which are interpreted by the geometry generator as:

- Genes $1 \rightarrow 10$: coordinates of 5 control points of a Bézier curve which describes the blade shape;
- Genes $11 \rightarrow 15$: chord length for the five blade sections;
- Genes $16 \rightarrow 20$: percentage of the rotor height for the five blade segments.

The fitness function is minimized by the optimization algorithm. In this work, both the aerodynamic performance and the structural stress are object of interest. The baseline design provides the peak power coefficient for tip speed ratios λ between 4 and 8 and this range is considered in the optimization routine. A multi-objective approach is adopted which provides a Pareto front with the optimal results (each solution in the front is not dominated). The optimization procedure aims at:

- Maximization of the maximum product between power coefficient and swept area, $C_P \cdot A$. This value provides a reference value for the power production which is not

however influenced by the free stream wind speed, being the latter varied in the adopted range.

- Minimization of the maximum flatwise stress σ_z along the blade, considering both the standstill and rotating operative conditions.

The total number of sectors for which the Aerodynamic Model is not converged is considered. This value is included as an additional objective to address the optimization algorithm towards solutions which are reliably simulated by the Aerodynamic Model and it will be considered as a filter during the post-processing phase to exclude failed individuals.

The choice of these three objectives allows to obtain turbine optimized configurations characterized by both high efficiency and low flatwise stress. The fitness values are the following:

$$\text{fitness} \;=\; \left[-\left(C_P A\right)_{\max}\,;\sigma_{\text{z,max}};n_{\text{bad}}\right] \tag{4.7}$$

4.4.2 Code Coupling

The Structural Model, Aerodynamic Model and Optimization Algorithm are coupled to create a loop algorithm as shown in Figure 4.29.

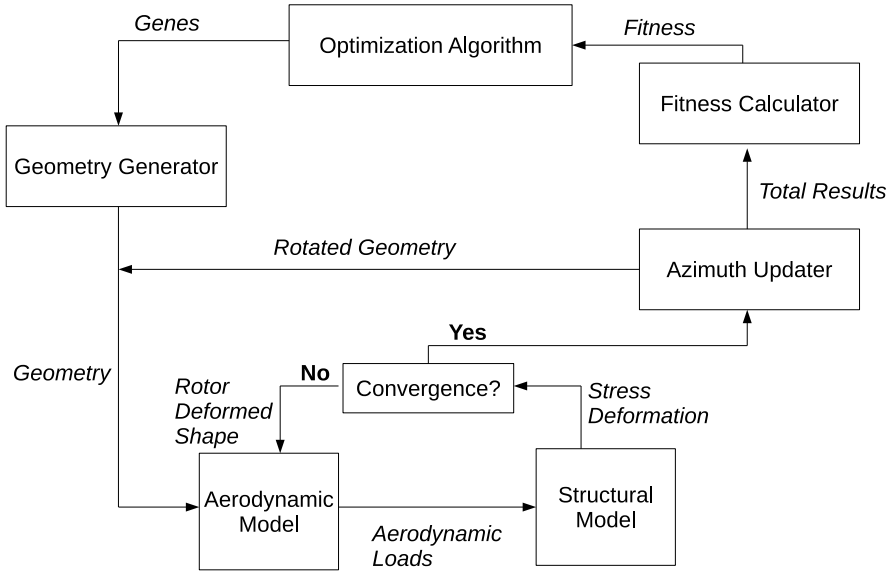

Figure 4.29: Optimization loop.

The geometry generated by the Geometry Generator is first simulated using the Aerodynamic Model, whose results are passed to the Structural Model to estimate the flatwise stress and deformation. The deformed shape is simulated again with the Aerodynamic Model and the iterative procedure is repeated until convergence in deformation is reached. This sub-loop is

evaluated for all the azimuthal positions in the mesh. Finally, the fitness calculator provides the Optimization Algorithm with the fitness vector calculated as previously described.

4.4.3 Results and Discussion

The optimization routine provided a Pareto front of non-dominated solutions. Among the three values in the fitness function, the third objective is considered as a filter to establish the reliability of the simulation: a maximum percentage of 1% for the total failed simulated sectors is accepted. The Pareto front considering the first two fitness values is shown in Figure 4.30(a). The baseline solution is highlighted with a red cross: a magnification of the Pareto front near the baseline solution is shown in Figure 4.30(b).

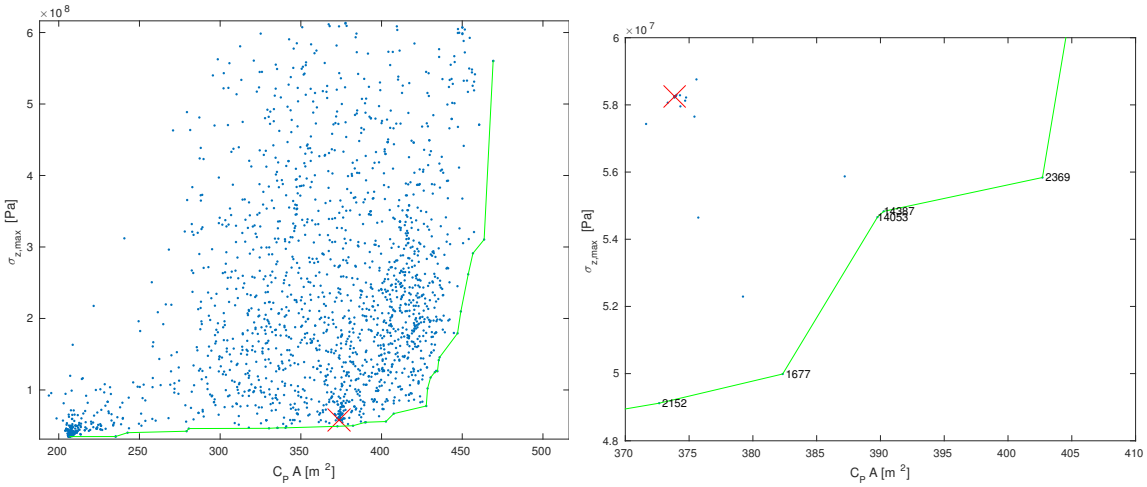

(a) Pareto (b) Localized Pareto

Figure 4.30: Pareto front and its magnification near the baseline configuration (red cross) for two fitness values and considering a maximum percentage of 1% for the failed simulated sectors.

The individuals which dominate the baseline solution are named in the magnification of the Pareto front in Figure 4.30(b). Three individuals are of particular interest thanks to their position with respect to the baseline:

- Individual 2152: characterized by a similar value of aerodynamic performance (C_PA) but a maximum flatwise stress reduced by 16%;
- Individual 2369: characterized by a similar value of maximum flatwise stress but aerodynamic performance increased by 8%;
- Individual 14387: selected among the individuals which dominate the baseline solution, it shows an increase of aerodynamic performance of 4% and a reduction of the maximum

flatwise stress of 6%.

These three individuals are characterized by different blade shapes, segments and chord lengths and are shown in Figure 4.31 compared against the baseline configuration, represented in dashed line with italic chord values. The chord lengths and the percentage of the rotor height for the five blade segments of the selected individuals are also reported in Table 4.7.

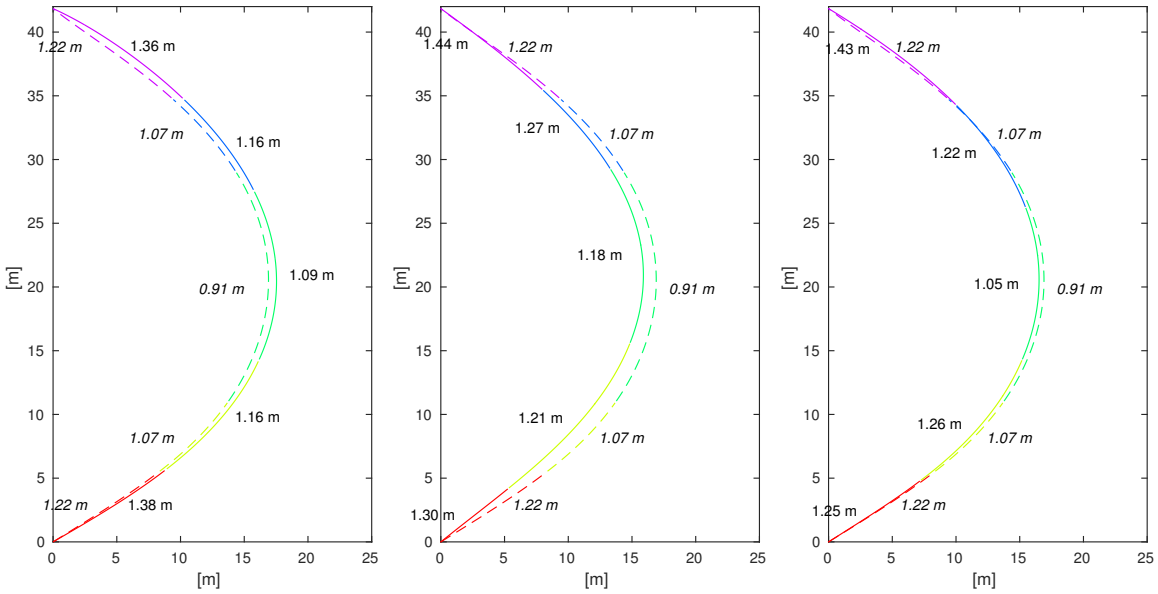

(a) Maximum $C_P A$ (b) Minimum σ_z (c) Trade-off

Figure 4.31: A selection of three individuals from the Pareto front which dominate the baseline solution: blade shape, segment position and chord lengths for the individual and baseline solution (dashed line and italic font).

Baseline		Maximum $C_P A$		Minimum σ_z		Trade-off	
c [m]	h [%]	c [m]	h [%]	c [m]	h [%]	c [m]	h [%]
1.22	16.9%	1.36	16.9%	1.44	15.0%	1.43	18.1%
1.07	13.8%	1.16	17.5%	1.27	15.0%	1.22	19.4%
0.91	43.1%	1.09	31.3%	1.18	32.5%	1.05	28.1%
1.07	13.1%	1.16	20.6%	1.21	27.5%	1.26	23.1%
1.22	13.1%	1.38	13.7%	1.30	10.0%	1.25	11.3%

Table 4.7: Chord lengths and percentage of the rotor height for the five blade segments of the selected individuals.

The three solutions need to be discussed specifically from the aerodynamic and structural point of view to highlight the different aspects of the optimization process.

4.4.4 Aerodynamic Analysis

The maximization of the aerodynamic performance value C_PA is obtained, as expected, by a configuration which also provides an increased swept area, see Figure 4.31(a). Nevertheless, the aerodynamic power coefficients C_P for the three configurations show increased peak values, which are also shifted towards lower values of the tip speed ratios λ, as shown in Figure 4.32. The peak values and their tip speed ratios for the different configurations are reported in Table 4.8.

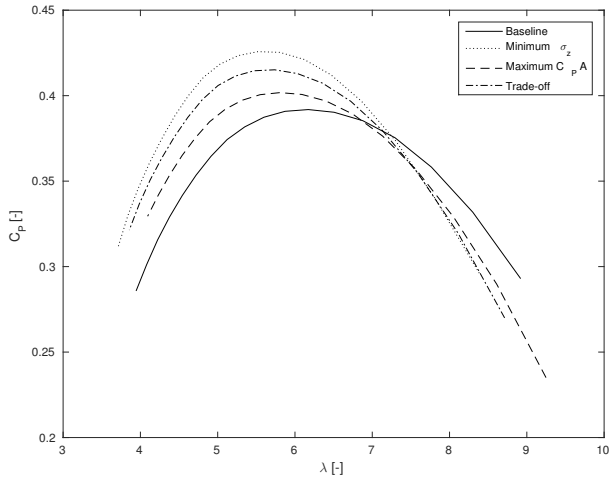

Figure 4.32: Power coefficient vs. tip speed ratio for the baseline and optimized configurations.

Configuration	$C_{\mathrm{P,max}}$	$\lambda\vert_{\mathrm{C_{P,max}}}$
Baseline	0.3919	6.1728
Maximum C_PA	0.4018	5.8071
Minimum σ_z	0.4258	5.5211
Trade-off	0.4151	5.7376

Table 4.8: Peak power coefficient and relative tip speed ratio for the baseline and optimized configurations.

The increase of the fitness target C_PA is therefore linked to an increase both of the swept area and the maximum power coefficient. To understand the variation of this second factor, which is the most important for the efficiency of a wind turbine, considerations based on the amount of energy extracted from the airflow can be conducted. The parameter which describes the energy extraction is the "induction factor" a, defined as:

$$a \;=\; 1 - \frac{v_i}{v} \tag{4.8}$$

being v_i the wind velocity the blade section and v the free-stream wind speed. The induction

factor varies between 0 (no absorption) and 1 (complete extraction). The adopted BEM algorithm, without the Glauert correction [33] for high induction factors, is considered reliable only for values lower than 0.5. The contour plots of the upwind induction factors for the baseline and optimized configurations operating at the maximum power coefficient conditions are reported in Figure 4.33.

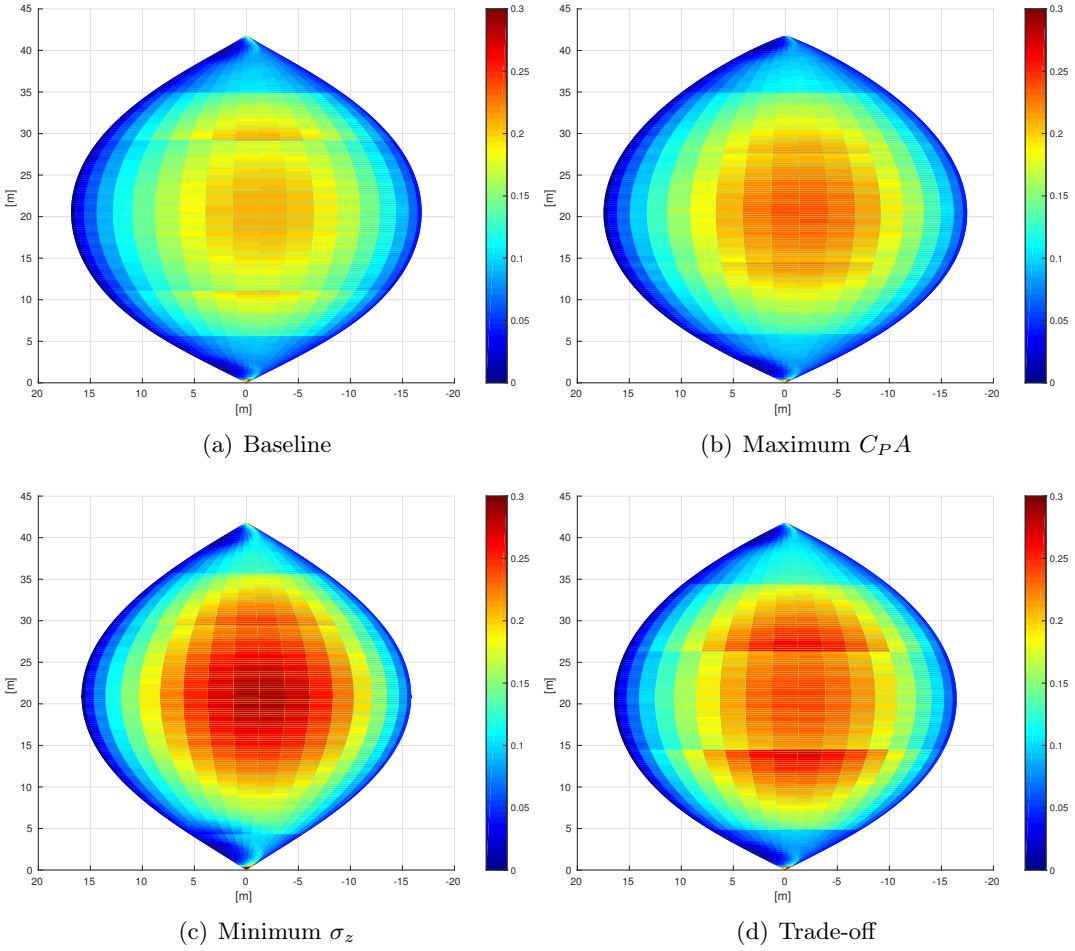

(a) Baseline

(b) Maximum C_PA

(c) Minimum σ_z

(d) Trade-off

Figure 4.33: Contour plots of the upwind induction factor for the baseline and optimized configurations operating at the maximum power coefficient conditions.

The induction factors of the baseline configuration (Figure 4.33(a)) are lower than those of the maximum C_PA configuration (Figure 4.33(b)). The values are increased in the central segments of the rotor, where the radius and the aerodynamic torque are higher. In these sections, the chord values are increased by 8% and 19%: the optimization algorithm leads the result towards a higher solidity, which increases the interaction with the air to an optimal value without penalizing the flatwise stress.

The configuration with the minimum flatwise stress σ_z is characterized by a reduced swept area (see Figure 4.31(b)) and therefore, to maintain the same value of C_PA, an increased energy

extraction is expected: Figure 4.33(c) shows, in fact, sensibly increased induction factors.

Finally, the Trade-off configuration in Figure 4.33(d), which is also characterized by a reduced swept area (see Figure 4.31(c)), shows a sensibly increased induction factors too. However, the chord lengths are larger than the maximum C_PA configuration to reduce the centrifugal stress, leading to a higher solidity than optimal.

4.4.5 Structural Analysis

The maximum total values of the flatwise stress σ_z, useful to conduct the design process, for the Baseline and optimized configurations operating at the maximum power coefficient conditions are reported in Figure 4.34.

The Minimum σ_z configuration is characterized by a smaller swept area but chord values sensibly increased, especially in the top section, see Figure 4.31(b). All the three selected configurations show an increase in chord length in this segment: this provides a sensibly decrease in the flatwise stress in correspondence of the shaft link, where a peak is registered in the baseline configuration, as can be seen in Figure 4.34(a).

High stress values are also registered in the second, fourth and fifth segment from the top, where the baseline configuration provides a flatwise stress up to 60 MPa. The stress is mainly linked to the inertial contribution of the centrifugal force, whereas the aerodynamic forces provide only a limited contribution [78, 79]. The Minimum σ_z configuration presents reduced peaks, see Figure 4.34(c), obtained both by decreasing the rotor maximum radius and increasing the airfoil section, leading to an increased mass but also an increased inertia. A partial reduction is registered for the Maximum C_PA configuration, see Figure 4.34(b), which is however presenting a maximum peak up to 50 MPa.

The central segment in the Maximum C_PA configuration presents a lower stress value than the Minimum σ_z configuration. The latter configuration is characterized, in fact, by an incremented chord length, with both aerodynamic performance and the centrifugal effects increased.

The Trade-off configuration presents a stress distribution similar to the Maximum C_PA configuration, see Figure 4.34(d). Higher values are registered in the central and fourth segments from the top, due to the larger radius with respect to the Minimum σ_z configuration and larger chord length with respect to the Maximum C_PA configuration. Average stress is lower than in Baseline configuration but stress peaks are comparable.

The structural design needs however to be conducted also considering the mean stress and its

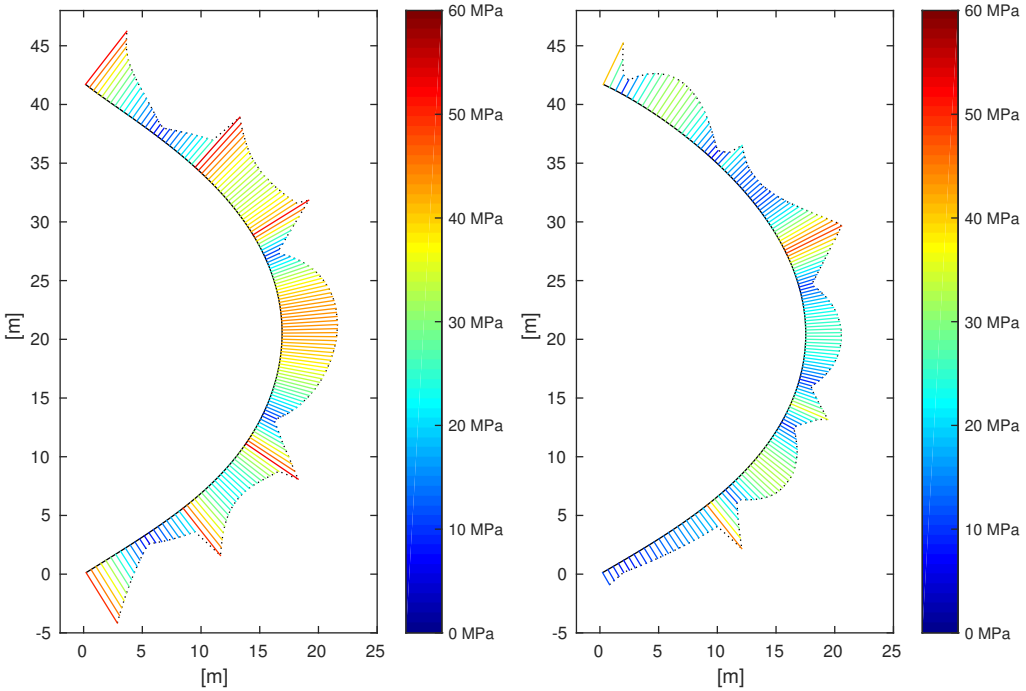

(a) Baseline

(b) Maximum $C_P A$

(c) Minimum σ_z

(d) Trade-off

Figure 4.34: Contour plots of the flatwise stress along the blade length for the baseline and the different optimized configurations operating at the maximum power coefficient conditions.

cycle amplitude to perform fatigue analysis. Despite these values are not considered as targets in the optimization process, their value can be estimated post-processing the results and are reported in Table 4.9.

Configuration	$\sigma_{z,mean}$ [MPa]	$\sigma_{z,max}$ [MPa]	$\sigma_{z,min}$ [MPa]	$\Delta\sigma_z$ [MPa]
Baseline	32.2940	57.2574	8.0732	49.1841
Maximum C_PA	23.7568	52.5699	8.4595	44.1104
Minimum σ_z	25.1233	49.1193	7.9687	41.1506
Trade-off	23.9713	54.3391	7.7365	46.6026

Table 4.9: Mean, maximum and minimum stress and cycle amplitude for the baseline and the different optimized configurations operating at the maximum power coefficient conditions.

Both the mean stress and the cycle amplitude are reduced in the Minimum σ_z configuration compared to the Baseline configuration, even though the mean stress is higher than in the Maximum C_PA and Trade-off configurations. Values are however sensibly reduced proving, therefore, that this optimization target scheme can also contribute to reduce the fatigue loads. Whether the fatigue design needs to be particularly considered in structural design, an additional optimization target can be considered.

4.4.6 Conclusions

The aerodynamic model based on BEM theory and the structural model adopting beam elements were correctly validated for the Sandia 34-meter Darrieus rotor, considered as Baseline configuration, against experimental data and surrogate models provided by commercial software. These models were coupled with an optimization algorithm based on the genetic theory, allowing to perform and evaluate variations of the blade shape and chord distribution.

The optimization routine, targeted to increase the aerodynamic performance and reduce the maximum blade stress of the Baseline rotor, provided a Pareto front populated with different configurations. A particular sector of this front, whose individuals dominate the Baseline configuration, is investigated from the aerodynamic and structural point of view.

From the aerodynamic analysis, an improvement in the rotor power production up to 8% is registered. The efficiency increase is obtained both with an increase of the swept area and a decrease in the tip speed ratio. On the other hand, the structural analysis showed a decrease in maximum stress up to 16%, obtained with a configuration which preserves the same aerodynamic production.

A Trade-off solution is also selected, which outperforms the Baseline configuration in both

the targets. The analysis showed that, despite this configuration can be obtained by small modifications from the Baseline design, it should be preferred since a significant increase in performance and reduction in stress is provided. These factors could lead to a lower cost of energy both reducing the rotor investment cost and increasing the energy production.

Chapter 5

Conclusions

This thesis provided an insight on physics, validation and application of different aerodynamic and structural methods to simulate the behavior of Darrieus Vertical Axis Wind Turbines (VAWTs). The considered aerodynamic tools include algorithm based on Blade Element Momentum, Vortex, two- and three-dimensional Unsteady Reynolds-Averaged Navier-Stokes (URANS) Computational Fluid Dynamics (CFD) models. On the structural side, a Finite Element Analysis (FEA) tool based on the beam model was shown to be reliable with a low computational effort. The advantages and disadvantages of the different models, validated against experimental results, were highlighted with respect to the particular application.

On a design stage, the algorithm based on Blade Element Momentum theory is the most favorable choice due to accuracy and reduced computational time. On the other hand, since the model reliability is strongly dependent on the adopted aerodynamic database, the analysis conducted on the different aerodynamic coefficients provides the wind turbine designer a complete overview on the choice for the most reliable. This analysis was the basis for the optimization of the DeepWind aerodynamic design, where different aerodynamic configurations were tested both manually and using an automatic optimization algorithm, obtaining an increase in aerodynamic performance up to 10%. The same tool, coupled with the FEA model, allowed to perform the blade shape and chord distribution optimization, identifying a shape closer to Troposkien which shows both aerodynamic production increased up to 8% and flatwise stress reduction up to 16%.

Simulation algorithms based on URANS CFD models are required to perform a deeper optimization of the rotor aerodynamics. The three-dimensional model was successfully adopted to simulate the particular case of a Troposkien rotor under tilted conditions, linked to

the floating turbine of the DeepWind project. A strong decrease in performance was registered, up to 60% for a tilt angle of 20°, which should be carefully kept into consideration during the design phase. A new airfoil shape was also obtained coupling the two-dimensional model with the optimization algorithm. The optimization was performed considering the rotor mean performance on a revolution, enabling a sensible increase in aerodynamic performance up to 8%.

The results presented in this thesis are to be carefully kept in consideration for the aero-structural design of Darrieus rotors since a significant performance increase is obtained. Moreover, the simulation tools can be used in the verification and testing phases by adopting the provided models which, being validated against experimental data, are shown to provide reliable results. Finally, the use of validated tools coupled with advanced optimization algorithms are shown to be effective for the design stage, enabling the designer to create innovative configurations which are increasing the energy conversion effectiveness and decrease structural loads.

Bibliography

[1] American Wind Energy Association. *U.S. Wind Industry Annual Market Report 2014*. Tech. rep. Washington, D.C., U.S.A.: American Wind Energy Association, 2014.

[2] "Turning Wind Power on its Side." *The Economist* (Mar. 2006).

[3] Hannes Riegler. "HAWT versus VAWT: Small VAWTs find a clear niche". *Refocus* 4.4 (2003), pp. 44–46. ISSN: 1471-0846. DOI: 10.1016/S1471-0846(03)00433-5.

[4] Jonathan Knight. "Urban wind power: Breezing into town". *Nature* 430.6995 (2004), pp. 12–13. ISSN: 0028-0836. DOI: 10.1038/430012a.

[5] Steven Peace. "Another approach to wind: vertical-axis turbines may avoid the limitations of today's standard propeller-like machines". *Mechanical Engineering-CIME* 126.6 (2004), pp. 28–32.

[6] Sandra Eriksson, Hans Bernhoff, and Mats Leijon. "Evaluation of different turbine concepts for wind power". *Renewable and Sustainable Energy Reviews* 12.5 (June 2008), pp. 1419–1434. ISSN: 13640321. DOI: 10.1016/j.rser.2006.05.017.

[7] Herbert J. Sutherland, Dale E. Berg, and Thomas D. Ashwill. *A Retrospective of VAWT Technology*. Tech. rep. Sandia National Laboratories Report SAND2012-0304, 2012.

[8] EEA. *Europe's onshore and offshore wind energy potential*. Tech. rep. 6. 2009, No 6/2009. DOI: 10.2800/11373.

[9] W. P. Musial and Bonnie Ram. *Large-Scale Offshore Wind Power in the United States*. Tech. rep. September. National Renewable Energy Laboratory, 2010, p. 240. DOI: 10.2172/990101.

[10] Jeremy Firestone, Willett Kempton, and Andrew Krueger. "Public acceptance of offshore wind power projects in the USA". *Wind Energy* 12.2 (2009), pp. 183–202. ISSN: 10954244. DOI: 10.1002/we.316.

[11] Christopher Neil Elkinton. "Offshore Wind Farm Layout Optimization". PhD thesis. University of Massachusetts, 2007, p. 325. ISBN: 0549330577.

[12] P. Gardner, A. Garrad, P. Jamieson, H. Snodin, G. Nicholls, and A. Tindal. "Volume 1: Technology." In: *Wind Energy - The Facts*. Brussels, Belgium: European Wind Energy Association, 2004.

[13] Henrik Svensson. "Design of foundations for wind turbines". *M.Sc. Thesis - Lund University* (2010).

[14] Marco Raciti Castelli, Stefano De Betta, and Ernesto Benini. "Preliminary Evaluation of Feasibility for Wind Energy Production on Offshore Extraction Platforms". *Wold Academy of Science, Engineering and Technology* 6.11 (2012), pp. 1873–1878.

[15] "http://www.inflow-fp7.eu/". *accessed on February 2015* ().

[16] Luca Vita. "Offshore Floating Vertical Axis Wind Turbines with Rotating Platform". Risø-PhD-80(EN). Danmarks Tekniske Universitet, 2011. ISBN: 9788755039247.

[17] Uwe Schmidt Paulsen, Luca Vita, Helge Aagård Madsen, Jesper Henri Hattel, Ewen Ritchie, Krisztina M Leban, Petter A. Berthelsen, and Stefan Carstensen. "1st DeepWind 5 MW baseline design". *Energy Procedia* 24 (2012), pp. 27–35.

[18] Uwe Schmidt Paulsen, Helge Aagård Madsen, Jesper Henri Hattel, Ismet Baran, and Per Hørlyck Nielsen. "Design Optimization of a 5 MW Floating Offshore Vertical-axis Wind Turbine". *Energy Procedia* 35 (2013), pp. 22–32.

[19] "http://www.deepwind.eu/The-DeepWind-Project". *accessed on February 2015* ().

[20] G. E. Reis and B. F. Blackwell. *Practical approximations to a troposkien by straight-line and circular-arc segments*. Tech. rep. Sandia National Laboratories Report SAND74-0100, 1975.

[21] James H. Strickland. *The Darrieus Turbine: A performance prediction model using multiple streamtubes*. Tech. rep. Sandia National Laboratories Report SAND75-0431, 1975.

[22] Ion Paraschivoiu. "Double-multiple streamtube model for Darrieus in turbines". In: *Wind Turbine Dynamics*. Cleveland, Ohio, USA: Nasa Conference Publication 2185, 1981, pp. 19–25.

[23] Ion Paraschivoiu and François Delclaux. "Double multiple streamtube model with recent improvements". *Journal of Energy* 7.3 (1983), pp. 250–255.

[24] James H. Strickland, B. T. Webster, and T. Nguyen. "A Vortex Model of the Darrieus Turbine: An Analytical and Experimental Study". *Journal of Fluids Engineering* 101.4 (1979).

[25] Alessandro Bianchini, Giovanni Ferrara, Lorenzo Ferrari, and Sandro Magnani. "An Improved Model for the Performance Estimation of an H-Darrieus Wind Turbine in Skewed Flow ACRONYMS". *Wind Energy* 36.6 (2012), pp. 667–686. ISSN: 0309524X. DOI: 10.1260/0309-524X.36.6.667.

[26] K. Wang, Martin Otto Laver Hansen, and T. Moan. "Model improvements for evaluating the effect of tower tilting on the aerodynamics of a vertical axis wind turbine". *Wind Energy* 18.January 2015 (2015), pp. 91–110. DOI: 10.1002/we.

[27] Christian Bak, Peter Fuglsang, and Helge Aagård Madsen. *Airfoil characteristics for wind turbines*. Tech. rep. Roskilde, Denmark: Risø National Laboratory Risø-R-1065(EN), 1999.

[28] Martin Otto Laver Hansen, Jens Nørkær Sørensen, Spyros G. Voutsinas, Niels N. Sørensen, and Helge Aagård Madsen. "State of the art in wind turbine aerodynamics and aeroelasticity". *Progress in Aerospace Sciences* 42.4 (June 2006), pp. 285–330. ISSN: 03760421. DOI: 10.1016/j.paerosci.2006.10.002.

[29] Marco Raciti Castelli, Alessandro Englaro, and Ernesto Benini. "The Darrieus wind turbine: Proposal for a new performance prediction model based on CFD". *Energy* 36.8 (June 2011), pp. 4919–4934. ISSN: 03605442. DOI: 10.1016/j.energy.2011.05.036.

[30] Gabriele Bedon, Marco Raciti Castelli, Ernesto Benini, and Marco Raciti. "Optimal Spanwise Chord and Thickness Distribution for a Troposkien Darrieus Wind Turbine". *Journal of Wind Engineering and Industrial Aerodynamics* 125.February (2014), pp. 13–21. ISSN: 0167-6105. DOI: 10.1016/j.jweia.2013.12.006.

[31] Gabriele Bedon, Marco Raciti Castelli, and Ernesto Benini. "Optimization of a Darrieus Vertical-Axis Wind Turbine using Blade Element Momentum Theory and Evolutionary Algorithm". *Renewable Energy* 59 (Nov. 2013), pp. 184–192. ISSN: 09601481. DOI: 10.1016/j.renene.2013.03.023.

[32] Gabriele Bedon, Marco Raciti Castelli, Uwe Schmidt Paulsen, Luca Vita, Ernesto Benini, and Marco Raciti Castelli. "Aerodynamic Optimization and Open Field Testing of a 1 kW Vertical Axis Wind Turbine". In: *EWEA 2013 Conference*. Wien, Austria, 2013.

[33] H. Glauert. "Airplane propellers". In: *Aerodynamic theory*. Springer Berlin Heidelberg, 1935, pp. 169–360. ISBN: 978-3-642-89630-9.

[34] R. J. Templin. *Aerodynamic performance theory for the NRC vertical-axis wind turbine*. Tech. rep. NASA STI/Recon N 76: 16618, 1974.

[35] S. Read and David J. Sharpe. "An extended multiple streamtube theory for vertical axis wind turbines". In: *2nd BWEA Workshop*. Cranfield, U.K., 1980, pp. 65–72.

[36] Ion Paraschivoiu. *Wind turbine design: with emphasis on Darrieus concept*. Montréal, Canada: Polytechnic International Press, 2002. ISBN: 2-553-00931-3.

[37] Robert E. Sheldahl. *Comparison of field and wind tunnel Darrieus wind turbine data*. Tech. rep. Sandia National Laboratories Report SAND80-2469, 1981.

[38] S. Watkins, S. Ravi, and B. Loxton. "The effect of turbulence on the aerodynamics of low Reynolds number wings". *Engineering Letters* 18.3 (2010). ISSN: 1816093X.

[39] K Freudenreich, K Kaiser, A P Schaffarczyk, H.Winkler, and B.Stahl. *Reynolds number and roughness effects on thick airfoils for wind turbines*. 2004. DOI: 10.1260/0309524043028109.

[40] Marinos Manolesos, Giorgos Papadakis, and Spyros G Voutsinas. "An experimental and numerical investigation on the formation of stall-cells on airfoils". *Journal of Physics: Conference Series* 555.1 (2014), p. 012068. ISSN: 1742-6588. DOI: 10.1088/1742-6596/555/1/012068.

[41] Robert E. Sheldahl and Paul C. Klimas. *Aerodynamic Characteristics of Seven Symmetrical Airfoil Sections Through 180-Degree Angle of Attack for Use in Aerodynamic Analysis of Vertical Axis Wind Turbines*. Tech. rep. Sandia National Laboratories SAND80-2114, 1981.

[42] B. K. Kirke, L. Lazauskas, and K. Davis. *Cyberiad Aerofoil Data*. 2008.

[43] Eastman N. Jacobs. *The aerodynamic characteristics of eight very thick airfoils from tests in the variable density wind tunnel*. Tech. rep. National Advisory Committee for Aeronautics 391, 1932.

[44] Eastman N. Jacobs and Albert Sherman. *Airfoil section characteristics as affected by variations of the Reynolds number*. Tech. rep. National Advisory Committee for Aeronautics 586, 1937.

[45] W. Kenneth Bullivant. *Tests of the NACA 0025 and 0035 airfoils in the ful-scale wind tunnel*. Tech. rep. National Advisory Committee for Aeronautics 708, 1941.

[46] G. M. Gregorek, M. J. Hoffman, and M. J. Berchak. *Steady State and Oscillatory Aerodynamic Characteristics of a Sandia 0018/50 Airfoil*. Tech. rep. Aeronautical and Astronautical Research Laboratory, The Ohio State University, 1989.

[47] Gabriele Bedon, Marco Raciti Castelli, and Ernesto Benini. *Extended aerodynamic coefficient databases for simulations of vertical axis wind turbines*. Tech. rep. University of Padua UniPD2013-02, 2013.

[48] L. E. Ericsson and J. P. Reding. "Fluid dynamics of unsteady separated flow. Part II. Lifting surfaces". *Progress in Aerospace Sciences* 24 (1987), pp. 249–356.

[49] J. G. Holierhoek, J. B. de Vaal, A. H. van Zuijlen, and H. Bijl. "Comparing different dynamic stall models". *Wind Energy* 16 (2013), pp. 139–158. DOI: 10.1002/we.

[50] Joseph Katz and Allen Plotkin. *Low-speed aerodynamics*. Cambridge University Press, 2001. ISBN: 0521665523.

[51] Marvin A. Jones. "The separated flow of an inviscid fluid around a moving flat plate". *Journal of Fluid Mechanics* 496 (Dec. 2003), pp. 405–441. ISSN: 00221120. DOI: 10.1017/S0022112003006645.

[52] Chengjie Wang and Jeff D. Eldredge. "Low-order phenomenological modeling of leading-edge vortex formation". *Theoretical and Computational Fluid Dynamics* 27 (2013), pp. 577–598. ISSN: 09354964. DOI: 10.1007/s00162-012-0279-5.

[53] Kiran Ramesh, Ashok Gopalarathnam, Jack R. Edwards, Michael V. Ol, and Kenneth Granlund. "An unsteady airfoil theory applied to pitching motions validated against experiment and computation". *Theoretical and Computational Fluid Dynamics* 27 (Jan. 2013), pp. 843–864. ISSN: 0935-4964. DOI: 10.1007/s00162-012-0292-8.

[54] J. W. Oler, James H. Strickland, B. J. Im, and G. H. Graham. *Dynamic stall regulation of the Darrieus turbine*. Tech. rep. August. Sandia National Laboratories Report SAND83-7029, 1983.

[55] Joseph Katz. "A discrete vortex method for the non-steady separated flow over an airfoil". *Journal of Fluid Mechanics* 102 (1981), pp. 315–328.

[56] Joseph Katz. "Large-Scale Vortex-Lattice Model for the Locally Separated Flow over Wings". *American Institute of Aeronautics and Astronautics Journal* 20.12 (1982), pp. 1640–1646.

[57] Kiran Ramesh, Ashok Gopalarathnam, Kenneth Granlund, Michael V. Ol, and Jack R. Edwards. "Discrete-vortex method with novel shedding criterion for unsteady aerofoil flows with intermittent leading-edge vortex shedding". *Journal of Fluid Mechanics* 751 (June 2014), pp. 500–538. ISSN: 0022-1120. DOI: 10.1017/jfm.2014.297.

[58] G. A. Osswald, K. N. Ghia, and U. Ghia. "Simulation of dynamic stall phenomenon using unsteady Navier-Stokes equations". *Computer Physics Communications* 65 (1991), pp. 209–218.

[59] Rajesh Bhaskaran and Alric P. Rothmayer. "Separation and Instabilities in the Viscious Flow over Airfoil Leading edges". *Computers & Fluids* 27.8 (Nov. 1998), pp. 903–921. ISSN: 00457930. DOI: 10.1016/S0045-7930(98)00014-0.

[60] Wallace J. Morris and Zvi Rusak. "Stall onset on aerofoils at low to moderately high Reynolds number flows". *Journal of Fluid Mechanics* 733 (Sept. 2013), pp. 439–472. ISSN: 0022-1120. DOI: 10.1017/jfm.2013.440.

[61] K. Stewartson, F. T. Smith, and K. Kaups. "Marginal separation". *Studies in Applied Mathematics* 67.1 (1982), pp. 45–61.

[62] AI Ruban. "Asymptotic theory of short separation regions on the leading edge of a slender airfoil". *Fluid Dynamics* 17.1 (1982), pp. 33–41.

[63] P. G. Saffman. "Vortex dynamics". In: *Cambridge Monographs on Mechanics*. Cambridge University Press, 1995.

[64] G. H. Vatistas, V. Kozel, and W. C. Mih. "A simpler model for concentrated vortices". *Experiments in Fluids* 11.1 (1991), pp. 73–76.

[65] Mahendra J. Bhagwat and J. Gordon Leishman. "Generalized viscous vortex model for application to free-vortex wake and aeroacoustic calculations". In: *58th Annual Forum and Technology Display of the American Helicopter Society International*. Montréal, Canada, 2002.

[66] Tuncer Cebeci, G. J. Mosinskis, and A. M. O. Smith. "Calculation of separation points in incompressible turbulent flows". *Journal of Aircraft* 9.9 (1972), pp. 618–624.

[67] Bryan Thwaites. *Incompressible aerodynamics: an account of the theory and observation of the steady flow of incompressible fluid past aerofoils, wings, and other bodies*. Dover Publications, 1960.

[68] Morten Hartvig Hansen, Mac Gaunaa, and Helge Aagård Madsen. *A Beddoes-Leishman type dynamic stall model in state-space and indicial formulations*. Tech. rep. Roskilde, Denmark: Risø National Laboratory R-1354(EN), 2004.

[69] Ansys Inc. *ANSYS FLUENT 14.5 User's Guide*. Ed. by Ansys Inc. Canonsburg, PA, U.S.A., 2012.

[70] William J. McCroskey, Laurence W. Carr, and Kenneth W. McAlister. "Dynamic stall experiments on oscillating airfoils". *American Institute of Aeronautics and Astronautics Journal* 14.1 (1976), pp. 57–63.

[71] William J. McCroskey, Kenneth W. McAlister, Laurence W. Carr, and S. L. Pucci. *An Experimental Study of Dynamic Stall on Advanced Airfoil Sections. Volume 1. Summary of the Experiment*. Tech. rep. NASA Technical Memorandum 84245, 1982.

[72] Kenneth W. McAlister, Laurence W. Carr, and William J. McCroskey. *Dynamic Stall Experiments on the NACA 00i2 Airfoil*. Tech. rep. Moffett Field, California: NASA Technical Paper 1100, 1978.

[73] Panayiote Gerontakos. "An Experimental Investigation of Flow Over an Oscillating Airfoil". *M.Sc. Thesis - McGill University* (2004).

[74] R. Bourguet, Guillaume Martinat, Gilles Harran, and Marianna Braza. "Aerodynamic multi-criteria shape optimization of VAWT blade profile by viscous approach". *Wind Energy* (2007), pp. 215–219.

[75] Carlos Simão Ferreira, Gerard J. W. van Bussel, and Gijs van Kuik. "2D CFD simulation of dynamic stall on a vertical axis wind turbine : verification and validation with PIV measurements". In: *45th AIAA Aerospace Sciences Meeting and Exhibit*. January. 2007, pp. 1–11.

[76] Travis J. Carrigan, Brian H. Dennis, Zhen X. Han, and Bo P. Wang. "Aerodynamic Shape Optimization of a Vertical-Axis Wind Turbine Using Differential Evolution". *ISRN Renewable Energy* (2012), pp. 1–40.

[77] A. Rossetti and G. Pavesi. "Comparison of different numerical approaches to the study of the H-Darrieus turbines start-up". *Renewable Energy* 50 (2013), pp. 7–19. ISSN: 09601481. DOI: 10.1016/j.renene.2012.06.025.

[78] Marco Raciti Castelli, Andrea Dal Monte, Marino Quaresimin, and Ernesto Benini. "Numerical evaluation of aerodynamic and inertial contributions to Darrieus wind turbine blade deformation". *Renewable Energy* 51 (2013), pp. 101–112. ISSN: 09601481. DOI: 10.1016/j.renene.2012.07.025.

[79] Marco Raciti Castelli, Stefano De Betta, and Ernesto Benini. "Numerical Evaluation of the Contribution of Inertial and Aerodynamic Forces on VAWT Blade Loading". *World Academy of Science, Engineering and Technology* 78 (2013), pp. 373–378.

[80] Dale E. Berg. *Structural design of the Sandia 34-meter vertical-axis wind turbine.* Tech. rep. Sandia National Laboratories Report SAND84-1287, 1985.

[81] Thomas D. Ashwill. *Initial Structural Response Measurements and Model Validation for the Sandia 34-Meter VAWT Test Bed.* Tech. rep. Sandia National Laboratories Report SAND88-0633, 1990.

[82] Torben J. Larsen and Helge Aagård Madsen. "On the way to reliable aeroelastic load simulation on VAWT's". In: *EWEA 2013 Conference.* Wien, Austria, 2013. ISBN: 9781632663146.

[83] Torben J. Larsen, Helge Aagård Madsen, Anders M. Hansen, and Kenneth Thomsen. "Investigation of stability effects of an offshore wind turbine using the new aeroelastic code HAWC2". In: *Proceedings of Copenhagen Offshore Wind 2005.* 2005, pp. 1–6.

[84] Amin Fereidooni, Fred Nitzsche, and Edgar A Matida. "Aeroelastic Study of a Vertical Axis Wind Turbine with Troposkien Shape". In: *32nd ASME Wind Energy Symposium.* January. American Institute of Aeronautics and Astronautics, 2014, pp. 1–13.

[85] B Roscher. "Structural Optimization Of A Vertical Axis Wind Turbine With Aeroelastic Analysis". *M.Sc. Thesis - Delft University of Technology* June (2014).

[86] Stephen Timoshenko. *History of Strength of Materials.* 1983, p. 452. ISBN: 0486611876. DOI: 10.1016/0022-5096(54)90010-1.

[87] Robert E. Sheldahl, Paul C. Klimas, and Louis V. Feltz. *Aerodynamic performance of a 5-metre-diameter Darrieus turbine with extruded aluminum NACA-0015 blades.* Tech. rep. Sandia National Laboratories Report SAND80-0179, 1980.

[88] Mark H. Worstell. *Aerodynamic performance of the 17-metre-diameter Darrieus wind turbine.* Tech. rep. Sandia National Laboratories Report SAND78-1737, 1979.

[89] Mark H. Worstell. *Aerodynamic performance of the 17-m-diameter Darrieus wind turbine in the three-bladed configuration: An addendum.* Tech. rep. Sandia National Laboratories Report SAND79-175, 1982.

[90] R. D. McConnell, J. H. Vansant, M. Fortin, and B. Piché. "An experimental 200 kW vertical axis wind turbine for the Magdalen Islands". In: *11th Intersociety Energy Conversion Engineering Conference*. New York: American Institute of Chemical Engineers, 1976, pp. 1798–1802.

[91] R. J. Templin and R. S. Rangi. "Vertical-axis wind turbine development in Canada". *IEE Proceedings A Physical Science, Measurement and Instrumentation, Management and Education, Reviews* 130.9 (1983), p. 555. ISSN: 0143702X. DOI: 10.1049/ip-a-1.1983.0085.

[92] Jacquelin Déry. "Éole, aérogénérateur à axe vertical de 4 MW à Capchat, Québec, Canada". In: *Intersol Eighty Five: Proceedings of the Ninth Biennial Congress of the International Solar Energy Society*. 1986, pp. 2030–2034.

[93] G. F. Homicz. *Numerical simulation of VAWT stochastic aerodynamic loads produced by atmospheric turbulence: VAWT-SAL code*. Tech. rep. Sandia National Laboratories Report SAND91-112, 1991.

[94] F. N. Fritsch. "Monotone piecewise cubic interpolation". *SIAM Journal on Numerical Analysis* 17.2 (1980), pp. 238–246.

[95] Maido Saarlas. *Aircraft performance*. Hoboken, New Jersey, USA: John Wiley & Sons, 2007, p. 282. ISBN: 0470044160.

[96] Matlab. *http://www.mathworks.com/help/techdoc/ref/pchip.html*.

[97] Christian Masson, Christophe Leclerc, and Ion Paraschivoiu. "Appropriate Dynamic-Stall Models for Performance Predictions of VAWTs with NLF Blades". *International Journal of Rotating Machinery* 4.2 (1998), pp. 129–139. ISSN: 1023-621X. DOI: 10.1155/S1023621X98000116.

[98] Richard Eppler. "Turbulent airfoils for general aviation". *Journal of Aircraft* 15.2 (1978), pp. 93–99.

[99] Christian Masson, Christophe Leclerc, and Ion Paraschivoiu. "Performance predictions of VAWTs with NLF airfoil blades". *Journal of Solar Energy engineering* 119.February (1997), pp. 97–99.

[100] Thomas D. Ashwill. *Measured data for the Sandia 34-meter vertical axis wind turbine*. Tech. rep. Sandia National Laboratories Report SAND91-2228, 1992.

[101] A. Fage and F. C. Johansen. "On the flow of air behind an inclined flat plate of infinite span". *Proceedings of the Royal Society of London. Series A, Containing Papers of a Mathematical and Physical Character* 116.773 (1927), pp. 170–197.

[102] A. J. Coyne, Mahendra J. Bhagwat, and J. Gordon Leishman. "Investigation into the rollup and diffusion of rotor tip vortices using laser Doppler velocimetry". In: *American Helicopter Society, 53rd Annual Forum, Virginia Beach, VA*. 1997.

[103] Mahendra J. Bhagwat and J. Gordon Leishman. "Measurements of bound and wake circulation on a helicopter rotor". *Journal of Aircraft* 37.2 (2000), pp. 227–234.

[104] H. B. Squire. "The Growth of a Vortex In Turbulent Flow". *Aeronautical Quarterly* 16 (1965), pp. 302–306.

[105] C. W. Oseen. "Über Wirbelbewegung in einer reibenden Flüssigkeit". *Arkiv för matematik, astronomi och fysik* 7 (1911), pp. 14–26.

[106] F. S. Archibald. "Unsteady Kutta condition at high values of the reduced frequency parameter". *Journal of Aircraft* 12.6 (1975), pp. 545–550.

[107] D. R. Poling and D. P. Telionis. "The response of airfoils to periodic disturbances-The unsteady Kutta condition". *American Institute of Aeronautics and Astronautics Journal* 24.2 (1986), pp. 193–199.

[108] Shengyi Wang, Derek B. Ingham, Lin Ma, Mohamed Pourkashanian, and Zhi Tao. "Numerical investigations on dynamic stall of low Reynolds number flow around oscillating airfoils". *Computers & Fluids* 39 (2010), pp. 1529–1541.

[109] Filippo Trivellato and Marco Raciti Castelli. "On the Courant-Friedrichs-Lewy criterion of rotating grids in 2D vertical-axis wind turbine analysis". *Renewable Energy* 62 (2014), pp. 53–62.

[110] Shengyi Wang, Derek B. Ingham, Lin Ma, Mohamed Pourkashanian, and Zhi Tao. "Turbulence modeling of deep dynamic stall at relatively low Reynolds number". *Journal of Fluids and Structures* 33 (2012), pp. 191–209.

[111] Guillaume Martinat, Marianna Braza, Y. Hoarau, and Gilles Harran. "Turbulence modelling of the flow past a pitching NACA0012 airfoil at 1e5 and 1e6 Reynolds numbers". *Journal of Fluids and Structures* 24.8 (2008), pp. 1294–1303.

[112] Ansys Inc. *ANSYS FLUENT 14.5 Theory Guide*. Ed. by Ansys Inc. Canonsburg, PA, U.S.A., 2012.

[113] Marco Raciti Castelli, Guido Ardizzon, Lorenzo Battisti, Ernesto Benini, and Giorgio Pavesi. "Modeling Strategy and Numerical Validation for a Darrieus Vertical Axis Micro-Wind Turbine". In: *ASME 2010 International Mechanical Engineering Congress & Exposition IMECE2010-39548*. Vancouver, British Columbia (Canada), 2010.

[114] G. H. Yu, X. C. Zhu, and Z. H. Du. "Numerical simulation of a wind turbine airfoil: dynamic stall and comparison with experiments". *Proceedings of the Institution of Mechanical Engineers, Part A: Journal of Power and Energy* 224.5 (2010), pp. 657–677. ISSN: 0957-6509. DOI: 10.1243/09576509JPE942.

[115] Gabriele Bedon, Stefano De Betta, and Ernesto Benini. "A computational assessment of the aerodynamic performance of a tilted Darrieus wind turbine". *Journal of Wind Engineering and Industrial Aerodynamics* 145 (2015), pp. 263–269. ISSN: 01676105. DOI: 10.1016/j.jweia.2015.07.005.

[116] Marco Raciti Castelli and Ernesto Benini. "Effect of blade inclination angle on a Darrieus wind turbine". *Journal of Turbomachinery* 134.031016 (2012), pp. 1–10.

[117] I. D. Mays, C. A. Morgan, M. B. Anderson, and S. J. R. Powles. "Experience with the VAWT 850 demonstration project". In: *European Wind Energy Conference*. Madrid, Spain, 1990, pp. 482–487.

[118] C. Ostowari and D. Naik. *Post Stall Studies of Untwisted Varying Aspect Ratio Baldes with NACA 44XX Series Airfoil Sections - Part II*. 1985.

[119] Francesco Balduzzi, Alessandro Bianchini, Riccardo Maleci, Giovanni Ferrara, and Lorenzo Ferrari. "Blade Design Criteria to Compensate the Flow Curvature Effects in H-Darrieus Wind Turbines". *Journal of Turbomachinery* 137.January (2015), pp. 1–10. ISSN: 0889-504X. DOI: 10.1115/1.4028245.

[120] B. F. Blackwell, Robert E. Sheldahl, and Louis V. Feltz. *Wind tunnel performance data for the Darrieus wind turbine with NACA 0012 blades*. Tech. rep. Sandia National Laboratories Report SAND76-013, 1976.

[121] B. W. McCormick. *Aerodynamics, aeronautics and flight mechanics*. 1994, p. 672. ISBN: 978-0-471-57506-1.

[122] Ansys Inc. *ANSYS Parametric Design Language 14.5 Guide*. Ed. by Ansys Inc. Canonsburg, PA, U.S.A., 2012.

[123] Paul Kuhn. *Some elementary principles of shell stress analysis with notes on the use of the shear center*. Tech. rep. Washington, USA: NACA Technical Notes No. 691, 1939.

[124] Uwe Schmidt Paulsen, Helge Aagård Madsen, Knud A. Kragh, Per H. Nielsen, Ismet Baran, Jesper Henri Hattel, Ewen Ritchie, Krisztina Leban, Harald Svenden, and Petter A. Berthelsen. "DeepWind - from idea to 5 MW concept". *Energy Procedia* 53.7465 (2014), pp. 23–33. ISSN: 1876-6102. DOI: 10.1016/j.egypro.2014.07.212.

[125] Uwe Schmidt Paulsen, Helge Aagård Madsen, Knud A. Kragh, Per H. Nielsen, Ismet Baran, Ewen Ritchie, Krisztina M. Leban, Harald Svenden, Petter A. Berthelsen, Gerard J. W. van Bussel, Carlos Simão Ferreira, and N. Chrysochoidis-Antsos. "The 5 MW DeepWind floating offshore vertical wind turbine concept design - status and perspective". In: *EWEA 2014 Conference*. Barcelona, Spain: European Wind Energy Association, 2014.

[126] David R. S. Verelst, Helge Aagård Madsen, Knud A. Kragh, and Federico Belloni. *Detailed Load Analysis of the baseline 5MW DeepWind Concept*. Tech. rep. September. Roskilde, Denmark: DTU Wind Energy Report E-0057, 2014.

[127] H. Charnock. "Wind stress on water: An hypothesis". *Quarterly Journal of the Royal Meteorological Society* 81.350 (1955), pp. 639–640. ISSN: 00359009. DOI: 10.1002/qj.49708135026.

[128] James L. Tangler. *The Evolution of Rotor and Blade Design*. Tech. rep. May. Palm Springs, California, USA: National Renewable Energy Laboratory Report NREL/CP-500-28410, 2000, p. 11.

[129] Gabriele Bedon, Marco Raciti Castelli, and Ernesto Benini. "Proposal for an Innovative Chord Distribution in the Troposkien Vertical Axis Wind Turbine Concept". *Energy* 66 (2014), pp. 689–698. DOI: 10.1016/j.energy.2014.01.004.

[130] Uwe Schmidt Paulsen, Troels Friis Pedersen, Helge Aagård Madsen, Karen Enevoldsen, Per Hørlyck Nielsen, Jesper Henri Hattel, Luca Zannel, Lorenzo Battisti, Alessandra Brighenti, Marie Lacaze, Victor Lim, Jakob W. Heinen, Petter A. Berthelsen, Stefan Carstensen, Erik-Jan De Ridder, Gerard van Bussel, and Giuseppe Tescione. "Deepwind - An Innovative Wind Turbine Concept for Offshore". In: *EWEA 2011 Conference*. 2011.

[131] Wayne Johnson. *Helicopter theory*. New York, U.S.A.: Dover Publications, 1980. ISBN: 0486682307.

[132] Gabriele Bedon, Enrico Giuseppe Agostino Antonini, Stefano De Betta, Marco Raciti Castelli, and Ernesto Benini. "Evaluation of the Different Aerodynamic Databases for Vertical Axis Wind Turbine Simulations". *Renewable & Sustainable Energy Reviews* 40 (2014), pp. 386–399. DOI: doi:10.1016/j.rser.2014.07.126.

[133] Kalyanmoy Deb. "Multi-objective optimization using evolutionary algorithms". In: *Multi-objective optimization*. Hoboken, NJ: John Wiley & Sons, 2001, pp. 13–46.

[134] R. W. Derksen and Tim Rogalsky. "Bezier-PARSEC: An optimized aerofoil parameterization for design". *Advances in Engineering Software* 41.7-8 (2010), pp. 923–930. ISSN: 09659978. DOI: 10.1016/j.advengsoft.2010.05.002.

[135] Mark Drela and Michael B. Giles. "Viscous-inviscid analysis of transonic and low Reynolds number airfoils". *American Institute of Aeronautics and Astronautics Journal* 25.10 (1987), pp. 1347–1355.

[136] Mark Drela. "XFOIL: An Analysis and Design System for Low Reynolds Number Airfoils". In: *Low Reynolds Number Aerodynamics*. Springer Berlin Heidelberg, 1989, pp. 1–12.

[137] Rosario Lanzafame, Stefano Mauro, and Michele Messina. "2D CFD modeling of H-Darrieus Wind Turbines using a transition turbulence model". *Energy Procedia* 45 (2014), pp. 131–140. ISSN: 18766102. DOI: 10.1016/j.egypro.2014.01.015.

[138] Matlab. "http://www.mathworks.com/help/gads/gamultiobj.html". *accessed on February 2015* ().

[139] M. C. Claessens. "The design and testing of airfoils for application in small vertical axis wind turbines". *M.Sc. Thesis - Faculty of Aerospace Engineering, Delft University of Technology* (2006).

[140] John Henry Holland. *Adaptation in natural and artificial systems.* Ann Arbour: The University of Michigan Press, 1975.

[141] John Henry Holland. *Adaptation in natural and artificial systems: an introductory analysis with applications to biology, control, and artificial intelligence.* Cambridge, MA, USA: MIT Press, 1992.

[142] R.P.J.O.M. van Rooij. *Modification of the boundary layer calculation in RFOIL for improved airfoil stall prediction.* Tech. rep. Delft, The Netherlands: Delft University of Technology, Report IW-96087R, 1996, p. 59.

[143] J. Bosschers. *Modelling of Rotational Effects with a 2-D Viscous-Inviscid Interaction Code.* Tech. rep. NLR Contract Report, CR 96521 C, 1997.

[144] B. F. Blackwell and G. E. Reis. *Blade shape for a troposkien type of vertical-axis wind turbine.* Tech. rep. Albuquerque, New Mexico: Sandia National Laboratory SLA-74-0154, 1977.

”If we shadows have offended,
Think but this, and all is mended,
That you have but slumber’d here
While these visions did appear.
And this weak and idle theme,
No more yielding but a dream,
Gentles, do not reprehend:
If you pardon, we will mend:
And, as I am an honest Puck,
If we have unearned luck
Now to ‘scape the serpent’s tongue,
We will make amends ere long;
Else the Puck a liar call;
So, good night unto you all.
Give me your hands, if we be friends,
And Robin shall restore amends.”

– William Shakespeare, A Midsummer Night’s Dream